Quantum transport in molecular devices and graphene

Quantum transport in molecular devices and graphene

Proefschrift

ter verkrijging van de graad van doctor
aan de Technische Universiteit Delft,
op gezag van de Rector Magnificus prof. dr. ir. J.T. Fokkema,
voorzitter van het College voor Promoties,
in het openbaar te verdedigen op vrijdag 8 december 2006 om 10.00 uur

door

Hubertus Bernardus HEERSCHE

natuurkundig ingenieur
geboren te Almelo.

Dit proefschrift is goedgekeurd door de promotors:
  Prof. dr. ir. L. P. Kouwenhoven
  Prof. dr. ir. H. S. J. van der Zant

Samenstelling van de promotiecommissie:

Rector Magnificus	voorzitter
Prof. dr. ir. L. P. Kouwenhoven	Technische Universiteit Delft, promotor
Prof. dr. ir. H. S. J. van der Zant	Technische Universiteit Delft, promotor
Prof. dr. H. Park	Harvard University, Verenigde Staten van Amerika
Prof. dr. H. B. Weber	Universität Erlangen-Nürnberg, Duitsland
Prof. dr. C. W. J. Beenakker	Universiteit Leiden
Prof. dr. C. Dekker	Technische Universiteit Delft
Dr. A. Morpurgo	Technische Universiteit Delft
Prof. dr. ir. J. E. Mooij	Technische Universiteit Delft, reservelid

Preface

In September 2002, I started my PhD working on transport through single molecules, a project initiated by my advisor Herre van der Zant, in the Quantum Transport (QT) group of Leo Kouwenenhoven and Hans Mooij. A challenging and explorative project, and a significant part of this Thesis is devoted to developing the technique of contacting single molecules and measuring their transport properties. Somewhere half-way my PhD, Herre started his own research group, together with Alberto Morpurgo, on molecular electronics and devices (MED). I stayed in QT and worked on somewhat different subjects. I was involved in a spintronics related project, and the last year of my PhD I spent working on graphene, a recently discovered material system with very exciting properties.

Many people contributed significantly to the work in this Thesis. First of all, I would like to thank my advisor and 'promotor' Herre van der Zant, for his continuous support throughout my whole PhD. Herre, with your optimism and sense of humor it has always been a pleasure to work with you. I learned that explorative research requires a different approach then I was used to. When you started your own group you respected my choice to stay (mostly) in QT and work on another project. I also owe much to my promotor Leo Kouwenhoven, who gave me almost unlimited freedom to work on whatever I preferred. This taught me not only to solve research problems, but also to think of them. His broad scientific knowledge and overview were always of great help.

Towards the end of my PhD I worked in the 'graphene team' at that time consisting of Albero Morpurgo, Lieven Vandersypen, Pablo 'the Hero', and novice Jeroen Oostinga. This collaboration turned out to be very effective. Alberto, I am impressed with your knowledge of physics and you kept the spirit high when we were working on the manuscript. Lieven, I'm confident that graphene will indeed provide the *perfect* qubit. Pablo, thanks to your enthusiasm and drive we got there so fast. It was a pleasure to work together so intensively during the last months of my PhD. I hope that the flakes in Columbia are even bigger. Jeroen, thanks for all the hours behind the microscope. Björn Trauzettel helped us a lot on the theory side and I could enter his office even (only?) with the silliest

questions. Recently, Lan and Dominique started working on graphene and I wish them a lot of success in the near future.

Collaborations with people outside QT were very valuable. At the start of my PhD, a short stay at prof. Park's group at Harvard was extremely useful to learn the tricks of electromigration and measurements on single molecules. Andrea Cornia and Laura Zobbi from the chemistry department of Modena University in Italy synthesized the molecules that we measured and hence their support was essential for this work. A visit to Jan Martinek in Poland helped us a lot to explain the Kondo effect measurements. Josh Folk, based at different places, always seemed to be working on the same topics as I was. Collaborations were quite fruitful. Josh, you once told me that 25 revisions of a manuscript is on the low side, and by now I believe you were right. Good luck with graphene. Theorists Maarten Wegewijs and Christian Romeike provided an explanation for about every molecule measurement we did and were to do. I am sorry that I had to remove the Hamiltonians from the figure captions in the manuscript due to space limitations (maybe tomorrow). The TEM project wouldn't exist without Henny Zandbergen, Günther Lientschnig (in Japan, thanks for the Skype conversations at 2am) and Kevin O'Neill. Help with fabrication and discussion with prof. Geim, Kostian Novoselov (it really seemed you enjoyed that 'rarely fried frog'), and Da Jiang from Manchester were invaluable for the graphene project. Discussions with Jos Thijssen, Gerrit Bauer, Bart van Wees (Groningen), Yuli Nazarov, Teun Klapwijk, and Carlo Beenakker (Leiden) were very helpful.

The more names you mention the more names you forget, so I only mention a few out of the many 'Delft people' that contributed to this Thesis. I acknowledge Hans Mooij and Leo Kouwenhoven for making QT such an exciting place to do research and such a pleasant place to work. I thank all (former) QT members for their contribution to the nice group atmosphere. I had the pleasure to advise graduate students Zeger de Groot and Dirk van der Mast. Zeger, thanks for breaking thousands of devices (for outsiders: they were meant to be broken). It may please you to know that I am writing this past the official deadline. Dirk, thanks to you many people know what 'Spin Räuschen' means. Floris, I enjoyed working together on the spin project and hope you'll manage to convert the results in a nice paper (don't let hockey-girls distract your attention).

I would like to thank all (former) Room A inhabitants and in particular Jorden van Dam and Jelle Plantenberg for the nice atmosphere, interesting discussions, and juicy stories. Jelle, I am glad see-not finally became CNOT. I hope Katja, Pieter or Pol won't run away with your reputation as the 'escalator initiator' during the last stage of your PhD. Jorden, you really seem to be serious about following Wouter Bos' career path; I just hope you won't get stopped by

a guy like J.P. Some other (ex-)QT people that cross my mind are: Ronald Hanson (co-founder of the 'Comité slechte koffie nee'), Jeroen Elzerman (thanks for your hospitality in Zürich), Silvano De Franceschi (too bad you couldn't come to Hanoi), Laurens Willems van Beveren & Ivo (nice bike trips), triple-F (Frank, you can really increase your life-expectancy by no longer climbing when under the influence of alcohol), Sami (sorry I sent you down that ski-slope), and prof. L.P.K. Voorhetkeren (applications of the flip-flop). But there are many others that made QT a superb place to work.

I greatly appreciate practical help and technical support from Raymond, Bram, Mascha (especially for bonding issues), Leo L., Willem & Wim (I consumed more helium than beer over the last four years), Leo D., and Remco. Yuki, Ria, Maria and Monique deserve being mentioned here for all their help with paperwork. In the cleanroom (DIMES) help from especially Anja van Langen, Arnold van Run, Mark Zuiddam, Roel Mattern, and Marco van der Krogt was very useful.

However enjoyable my time in QT was, it's hard to beat the Swiss mountains. I enjoyed the great ski-mountaineering trips with Jochem Baselmans, Jim Weistra, and Cas van der Avoort. Climbing is another of those relaxing activities and I spent quite a few hours on the wall especially with Martijn Krutzen and Peter (Peewee) ter Winkel. Ellen Oosterhof, thanks for the tips on the cover design. I would like to thank my friends and family, and in particular Bernard, Jan, Jogien, and my mother for their love and support.

One of my promotors once told me that it is unlikely to finish your PhD with the same girlfriend as you start it with. I'm glad promotors are sometimes proven wrong. Sanne, bedankt voor al je vrolijkheid, steun en liefde.

<div align="right">
Hubert Heersche

October 2006
</div>

Contents

Chapter 1

Introduction

1.1   Molecular electronics

Breakthroughs in nanoscale condensed matter physics are often the result of miniaturization or new material systems. Electron transport experiments have explored the electrical conductance of smaller and smaller systems. At the same time, progress in material science has provided the high quality material systems (eg. semiconducting hetero-structures) that allowed for the exploration of new transport regimes.

Presently, miniaturization has brought us to the stage where we can start to explore electron transport on the scale of a single molecule. This implies that many new 'material systems' - the large number of different molecules that have been synthesized today - become available as well. The field of *molecular electronics* [1] is therefore receiving increasing attention from fundamental scientists and industry alike. The advantage of molecules as an electronic building block is that the molecules can be engineered to have some built in functionality or special property (synthetic tailorability), acting, for example, as a light sensitive switch. Furthermore, molecules are small and hence molecular systems could provide a way to scale down electronic devices even further, especially if self-assembly can be used to fabricate nanoscale circuits.

Molecular electronics is a broad field and research ranges from room temperature and application driven to fundamental research at low temperature. For functional devices, a single molecule will generally not be an ideal electronic component, simply because its resistance is too high and many molecules are usually placed in parallel. For fundamental research, on the other hand, the possibility to wire up a single molecule is an exciting new way to study the properties of an individual molecule, Fig. 1.1a. Measurements are usually performed at low temperatures (20 mK - 4 K) both because the system is more stable at these

a

b
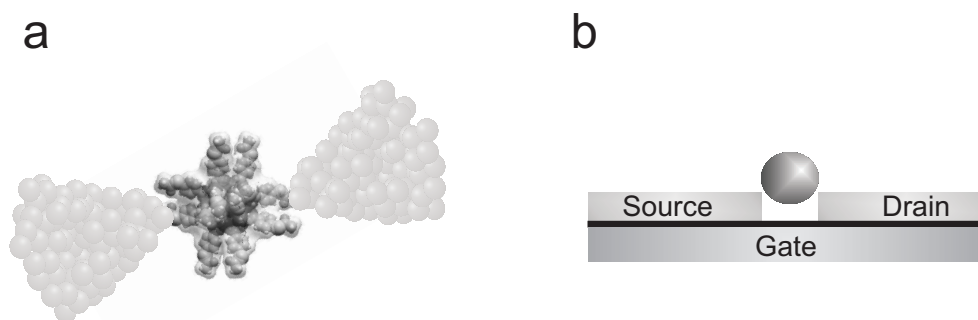
Source   Drain

Gate

Figure 1.1: a, Artist impression of a single molecule magnet contacted by gold elec-
trodes. **b**, Schematic drawing of a single molecule (sphere) contacted by source and
drain electrodes. A third gate electrode is separated from the leads by a thin isolating
oxide layer (black). The separation between the electrodes is approximately 200 nm.

temperatures and because quantum mechanical phenomena are generally 'washed
out' at higher temperatures.

1.1.1   The conductance of a molecule

What is the conductance of a single molecule? Certainly, Ohms law, which predict
a linear relation between current and voltage, is not applicable. Since the 1980's,
it is known that for sufficiently small systems (mean free path longer than sample
dimensions) conductance is quantized in channels that have a conductance of
$12.9\,k\Omega$ each. At low bias voltages, molecules typically consist of only one channel
as a result of their discrete energy spectrum. The contact between the leads and
the molecule is generally not perfect and creates a (tunnel) barrier. This means
that the molecule forms a semi-isolated island that is only weakly coupled to the
leads. The capacitance of this island is so small, however, that a considerable
charging energy has to be paid by an electron, to hop on and off the molecule.
Especially at low temperatures, when the electrons hardly possess any thermal
energy, this means that electrons can only tunnel on and off the molecule one by
one: the sequential electron tunneling (SET) regime. In this transport regime,
the conductance of a molecule is directly affected by the energy spectrum of the
molecule. In combination with a gate electrode that can tune the electrostatic
potential on the molecule (Fig. 1.1), conductance measurements allow us to do
level spectroscopy and study vibrational [2] and other excitations of the molecule.

1.1.2 Wiring up a molecule

Despite the powerful fabrication techniques that a nanoscientist has at his disposal today, creating electrodes with a small enough separation to wire up a single molecule remains challenging. Molecules are generally very small entities (with the exception of some bio-molecules) with a typical size of a few nanometer or smaller. State of the art electron beam lithography (EBL), which is used to create small electronic circuits on a chip, has a resolution of about 20 nm. Over the years, a number of techniques have been developed to contact a molecule. They all have their own advantages and drawbacks. The first attempts to measure the conductance of a molecule made use of scanning probe techniques (SPM). SPM allows controlled two-terminal experiments and transport experiments on individual molecules were performed successfully [4, 3]. Other techniques include nanopore [5], breakjunction [7, 8], electrodeposition [6], and nanolithography.

In this Thesis we used electromigration [9] of thin gold wires on top of a silicon (Si) substrate to fabricate the nanometer scale gaps (nanogaps) required to trap an individual molecule. Although the underlying mechanism is different, the idea is similar to blowing a fuse on purpose. When a fuse blows, you end up with two 'wires' that are separated by a gap. The aim is to make the gap so small that a molecule fits in between (i.e. about a nanometer). This technique has several advantages. First of all, it is fast. Gold wires can be fabricated dozens at a time, and electromigrating ('blowing') them does not require so much effort either. This way, many individual molecules can be characterized after each other, which is necessary to gain some statistics and extract which properties are generic or rather exceptional. A second advantage is that a gate electrode can be fabricated underneath the gap, isolated by a thin layer of insulating oxide. Whereas a two-terminal measurement only allows for a single current-voltage (I-V) measurement, with a gate we can modify the energy spectrum of the molecule and study how this affects the differential conductance.

Although in principle a simple technique, nanogap fabrication through electromigration is quite a subtle process and depends on many parameters. In spite of the fact that the electromigration process has been studied quite extensively in the past to prevent failure of wires in microelectronics, not so much is known about its application as a fabrication method for single molecule contact leads. As a consequence, a significant effort has been made to further investigate nanogap formation and to find ways to gain some control over it. In Chapter 4 we demonstrate electromigration on the atomic scale: single gold atoms are removed one by one resulting in discrete conductance values of the wire. At the same time, characterization of the bare gap conductance demonstrates similar features as

those expected for single molecules. They originate from charge traps in the gap, most likely ultra-small gold grains. These gold grains are a nuisance for single molecule experiments, but form an interesting system on their own.

A serious drawback of both characterization of bare gold gaps and single molecule measurements is that the system is more or less a 'black box'. Imaging techniques, like scanning electron microscopy (SEM), have insufficient resolution to provide detailed information about the electrode geometry. This stimulated us to develop a new technique to image the electromigration process *in situ* with transmission electron microscopy (TEM). This results in detailed, real-time video recordings of the nanogap formation process, that are discussed in Chapter 5.

1.1.3   Choosing the right molecule

Given the fact that small gold grains in the gap can mimic the transport characteristics of a molecule, the choice of molecule has to be such that it has a clear signature to distinguish it. In Chapter 6 we discuss transport measurements on so-called single-molecule magnets (SMM). Although magnetism is usually a bulk property of a material, the magnetic hysteresis observed in crystals of SMMs is related to the high spin ground state of individual, decoupled molecules. In combination with the high anisotropy barrier of the molecules with an easy (or preferred) axis, the high spin ground state can have fixed orientation resulting in a net magnetization at sufficiently low temperature. A magnetic field can effectively reduce the energy barrier between the two spin configurations (parallel or anti-parallel to the easy axis). At sufficiently high field, the energy barrier is so small that the magnetization can tunnel from an anti-parallel to parallel configuration. Tunneling is a quantum mechanical process that is classically not allowed and the 'macroscopic' tunneling of the magnetization is quite a fascinating phenomenon that has received a lot of attention.

When a current is sent through a molecule, electrons are subsequently added to and subtracted from it. Since an electron not only possesses charge but also spin, applying a current bias means that we are constantly changing the total spin of the molecule. Consequently, spin states of the molecule can be excited by electrons from the leads, provided that the total energy and spin of the electron and molecule are conserved. At the same time, transition rates between different spin states are not equal and when certain transitions become available energetically, by increasing the bias voltage, the current may either increase or decrease depending on the detailed situation. The high spin ground state of the molecule therefore results in signatures in the current-voltage characteristics that are not expected for other charge traps and hence provides extra confidence that we are

indeed measuring transport through a single molecule.

1.1.4 Interaction between artificial and real magnetic impurities

Fundamental research is often unpredictable and sometimes a system that was created by accident provides the basis for a nice experiment. While characterizing bare gold nanogaps, we found that in some gaps small gold grains were present that could mimic the transport behavior of a molecule. This was, more or less simultaneously, also realized by other research groups working in the field [10, 11]. Electrons in the ultra-small gold grain are confined by its size and hence the gold grain acts basically as an artificial atom with discrete energy states.

When wires were electromigrated with certain parameters, many of the I-Vs revealed an enhancement of the differential conductance around zero bias voltage compared to higher bias. This so-called zero-bias anomaly originates from the Kondo effect: a quantum many body effect that enhances the conductance due to a coupling between the net electron spin of the gold grain and the spins of the conduction electrons in the leads as a result of spin-flip processes. The Kondo effect has been studied extensively in the last decade in artificial atoms that were created in semiconducting structures.

The spin of magnetic impurities (like cobalt atoms) in a paramagnetic metal (like gold) are also Kondo screened in a bulk material. As a result, the resistance of the polluted metal *increases* when lowering the temperature, due to enhanced spin scattering (the Kondo effect only survives at low temperatures). However, interactions between magnetic impurities suppress the Kondo effect when the concentration of the magnetic impurities becomes too high. The reason is that interactions fix the spin of the impurity, suppressing spin-flip processes that lead to the Kondo effect. The interaction between the spins is indirect, via the conduction electrons of the gold. Since the sign of this interaction (ferromagnetic, anti-ferromagnetic) is 'random', the system, known as a spin glass, possesses many magnetic ground state configurations and is therefore characterized by extremely long relaxation times.

In Chapter 7 we measure the indirect interaction between an artificial magnetic impurity (the gold grain) and cobalt impurities in the leads. The energy scale on which the Kondo effect is suppressed is a measure for the interaction strength. The system provides an exciting new method to study Kondo and RKKY interactions in metals at the level of a single spin.
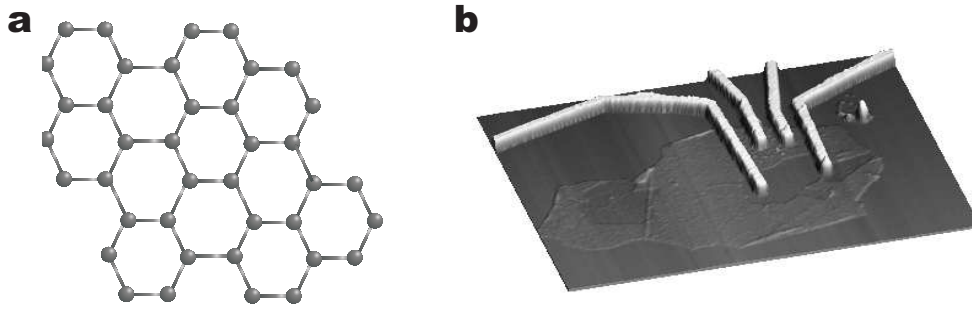
Figure 1.2: a, Graphene is a 2-dimensional sheet of conjugated carbon atoms. **b**, Atomic force microscopy picture (AFM) of a few layer graphene sheet contacted by metallic electrodes for electrical characterization.

1.2 Graphene

Whether graphene - a 2-dimensional sheet of conjugated carbon atoms (Fig. 1.2)- is still a molecule is debatable, but it certainly is a very fascinating system from a quantum-transport point of view. Graphene is a gap-less semiconductor, or semi-metal, in which the Fermi-energy can be tuned continuously from the valence band, where current is carried by holes, to the conduction band, where electrons carry the current. As a result of its conical band structure at low energies, electrons behave as if they were massless Dirac particles. This is quite special for a solid-state system and requires a different mind-set when trying to explain transport experiments in graphene. We study graphene, in contrast to the single molecules, in the limit of transparent interfaces between graphene and electrodes. The contact material was chosen such that it becomes superconducting at low temperatures. Due to the Josephson effect, we could induce a supercurrent (a current that flows without dissipation) in graphene. The experiment is described in detail in Chapter 8. The device is effectively a Josephson field-effect transistor (JOFET) in which the supercurrent can be tuned with a gate voltage. Moreover, the supercurrent is bipolar: depending on gate voltage it is carried either by holes or electrons. The physical mechanism behind supercurrent transport in graphene is Andreev reflection which, interestingly, couples the two sub-bands of graphene.

1.3 Outline

The content of this Thesis is outlined below:

Chapter 2: This Chapter gives an introduction to the theoretical concepts used throughout this work. We start by discussing Coulomb blockade and the

constant interaction model (CIM). Next we treat modifications and additions to the CIM that are specific for single molecule quantum dots, like vibrational modes. Also, we briefly discuss the special properties of single molecule magnets (high-spin molecules). We give an introduction to the Kondo effect and how it is affected by indirect (RKKY) interactions with magnetic impurities. Finally, we provide a basic introduction to the special properties of graphene and briefly discuss the Josephson effect.

Chapter 3: We describe how the graphene samples are fabricated. In addition we discuss Raman spectroscopy measurements from which the layer thickness of graphite samples can be determined. General fabrication and measurement techniques are also briefly summarized.

Chapter 4: This Chapter summarizes the most important findings of thousands of wires that we broke, using electromigration. We are able to break gold wires atom by atom and demonstrate some control over the final gap size. We also show that bare gold junctions can show features (Coulomb blockade, Kondo effect) similar to those expected for molecules.

Chapter 5: Aiming at getting a better control over electromigration-induced nanogap fabrication, we developed a new technique to image the breaking process *in situ* using transmission electron microscopy (TEM). Real-time recordings of the breaking demonstrate void and hillock formation in the early stages of electromigration. Zooming in on the narrowest constriction, we recorded the final stage of the breaking with high resolution. We show that a relatively large deformation takes place at the moment of breaking. The shape of the remaining electrodes is important for single molecule transport experiments.

Chapter 6: How does the high spin ground state of a molecule effect electron transport? In this Chapter we study transport through Manganese-12 derivatives, known as single molecule magnets, in the Coulomb blockade regime. Spin excitations of the molecule are shown to influence its transport properties. Experimental results are compared to a simple model.

Chapter 7: Quantum dots, consisting of ultra-small gold grains, can act as an artificial magnetic impurity when they possess a net spin. In this Chapter we study the indirect (RKKY) interaction between such an artificial magnetic impurity and cobalt atoms. It is demonstrated that the interaction results in a suppression of the Kondo effect at low bias voltages. Moreover, when the inter-

action is anti-ferromagnetic the Kondo effect can be restored by a magnetic field.

Chapter 8: The relativistic transport properties of graphene are very unusual in the field of condensed matter physics. We contacted graphene sheets, by superconducting electrodes. Owing to the Josephson effect, we observe proximity induced supercurrents in graphene. We show that supercurrents survive even at the charge neutrality (or Dirac) point, demonstrating phase coherence in this regime.

References

[1] For review papers see e.g.: Joachim, C., Gimzewski, J. K. & Aviram, A. *Electronics using hybrid-molecular and mono-molecular devices.* Nature **408**, 541 (2000); Heath, J. R. & Ratner, M. A. *Molecular electronics.* Phys. Today **56**, 43 (2003).

[2] Park, H. *et al. Nanomechanical oscillations in a single-C60 transistor.* Nature **407**, 57 (2000).

[3] Bumm, L. A. *et al. Are single molecular wires conducting?* Science **271**, 1705 (1996).

[4] Joachim, C., Gimzewski, J. K., Schlittler, R. R. & Chavy, C.*Electronic Transparency of a Single C-60 Molecule.* Phys. Rev. Lett. **74**, 2102-2105 (1995).

[5] Reed, M. A. *et al. The electrical measurement of molecular junctions.* Molecular Electronics: Science and Technology **852**, 133 (1998).

[6] Morpurgo, A.F., Marcus, C.M. & Robinson, D.B. *Controlled fabrication of metallic electrodes with atomic separation.* Appl. Phys. Lett., **74**, 2084 (1999).

[7] Reed, M. A., Zhou, C., Muller, C. J., Burgin, T. P. & Tour, J. M. *Conductance of a molecular junction.* Science **278**, 252 (1997).

[8] Kergueris, C. et al. *Electron transport through a metal-molecule-metal junction.* Phys. Rev. B **59**, 12505 (1999).

[9] Park, H., Lim, A. K. L., Alivisatos, A. P., Park, J. & McEuen, P. L. *Fabrication of metallic electrodes with nanometer separation by electromigration.* Appl. Phys. Lett. **75**, 301 (1999).

[10] Houck, A. A., Labaziewicz, J., Chan, E. K., Folk, J. A. & Chuang, I. L. *Kondo effect in electromigrated gold break junctions.* Nano Lett. **5**, 1685 (2005).

[11] Sordan, R., Balasubramanian, K., Burghard, M. & Kern, K. *Coulomb blockade phenomena in electromigration break junctions.* Appl. Phys. Lett. **87**, 013106 (2005).

Chapter 2

Theory

This Chapter provides background theory related to the experiments described in subsequent Chapters. We start with the theory of quantum dots and the constant interaction model. Subsequently, we make the link to single molecules, in particular single molecule magnets, that are weakly coupled to metallic leads. We further discuss the Kondo effect and RKKY exchange interaction between impurity spins. We also give a brief introduction to the transport properties of graphene and, finally, summarize some properties of the Josephson effect.

2.1   Quantum Dots

A quantum dot (QD) is a small conducting island that is weakly coupled to lead electrodes, such that electrons can be exchanged (see Fig. 2.1). Because it is semi-isolated, the electrons are confined by the size of the dot. Similar to the famous 'particle in a box' problem treated in quantum mechanics courses, the resulting energy spectrum is discrete. The level separation increases when the dot becomes smaller. The QD is also capacitively coupled to one or more 'gate' electrodes, that can be used to tune the electrostatic potential of the dot with respect to the reservoirs. Quantum dots have been studied in many different material systems including metallic nanoparticles, semiconductor heterostructures, and carbon nanotubes. In these structures, the confinement is implemented by introducing barriers, often through gate electrodes. A molecule is in fact a natural quantum dot and has many similarities to the systems mentioned above. This is why we start with a general introduction to quantum dot physics closely following ref. [1].
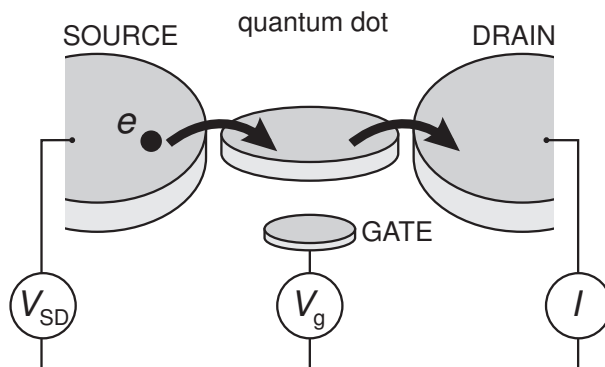
Figure 2.1: Schematic picture of a quantum dot. The quantum dot (represented by a disk) is connected to source and drain contacts via tunnel barriers, allowing charge carriers to tunnel to and from the quantum dot. Here, current through the device, I, is measured in response to a bias voltage, V_{SD} and a gate voltage, V_g.

2.1.1   Constant interaction model

A simple, yet very useful model to understand electronic transport through QDs is the constant interaction (CI) model [2]. In this model two important assumptions are made. First, the Coulomb interactions between electrons in the dot are captured by a single constant capacitance, C. This is the total capacitance to the outside world, i.e. $C = C_S + C_D + C_g$, where C_S is the capacitance to the source, C_D that to the drain, and C_g to the gate. Second, the discrete energy spectrum is independent of the number of electrons on the dot. Under these assumptions the total energy of an N-electron dot with the source-drain voltage, V_{SD}, applied to the source (and the drain grounded), is given by

$$U(N) = \frac{[-|e|(N - N_0) + C_S V_{SD} + C_g V_g]^2}{2C} + \sum_{n=1}^{N} E_n \quad , \tag{2.1}$$

where $-|e|$ is the electron charge and N_0 the number of electrons on the dot at zero gate voltage. The terms $C_S V_{SD}$ and $C_g V_g$ can change continuously and represent the charge on the dot that is induced by the bias voltage (through the capacitance C_S) and the gate voltage V_g (through the capacitance C_g), respectively. The last term of Eq. 2.1 is a sum over the occupied single-particle energy levels E_n, which are separated by an energy $\Delta E_n = E_n - E_{n-1}$. These energy levels depend on the characteristics of the confinement potential.

To describe transport experiments, it is often more convenient to use the electrochemical potential, μ. This is defined as the minimum energy required to add an electron to the quantum dot

$$\mu(N) \equiv U(N) - U(N-1) =$$
$$= (N - N_0 - \frac{1}{2})E_C - \frac{E_C}{|e|}(C_S V_{SD} + C_g V_g) + E_N \quad , \tag{2.2}$$

where $E_C = e^2/C$ is the charging energy. A diagram with electrochemical potentials for different electron numbers, N, is shown in Fig. 2.2a. The discrete levels are spaced by the so-called addition energy, $E_{add}(N)$

$$E_{add}(N) = \mu(N+1) - \mu(N) = E_C + \Delta E \quad . \tag{2.3}$$

The addition energy consists of a purely electrostatic part, the charging energy E_C, and the energy spacing between two discrete quantum levels, ΔE. Note that ΔE can be zero, when two consecutive electrons are added to the same spin-degenerate level or if there are additional degeneracies present.

Transport can occur when an electrochemical potential level (or state) lies within the 'bias window' between the electrochemical potential of the source (μ_S) and the drain (μ_D), i.e. $\mu_S \geq \mu \geq \mu_D$ with $-|e|V_{SD} = \mu_S - \mu_D$. Only then an electron can tunnel from the source onto the dot, and tunnel off to the drain without losing or gaining energy. The important point to realize is that since the dot is very small, it has a very small capacitance and therefore a large charging energy E_C. If the electrochemical potential levels are as shown in Fig. 2.2a, this energy is not available (at low temperatures and small bias voltage). So, the number of electrons on the dot remains fixed and no current flows through the dot. This effect is known as Coulomb blockade. The charging energy becomes important when it exceeds the thermal energy, $k_B T$, and when the barriers are sufficiently opaque such that the electrons are located either in the reservoirs or in the dot. The latter condition implies that quantum fluctuations in the number of electrons on the dot must be sufficiently small. A lower bound for the tunnel resistances R_t of the barriers can be found from the Heisenberg uncertainty principle. The typical time Δt to charge or discharge the dot is given by the RC-time. This yields $\Delta E \Delta t = (e^2/C)R_t C > h$. Hence, R_t should be much larger than the quantum resistance h/e^2 to sufficiently reduce the uncertainty in the energy.

It turns out that there are several ways to lift Coulomb blockade. First, we can change the voltage applied to the gate electrode. This changes the electrostatic potential of the dot with respect to that of the reservoirs, shifting the whole 'ladder' of electrochemical potential levels up or down. When a level falls within
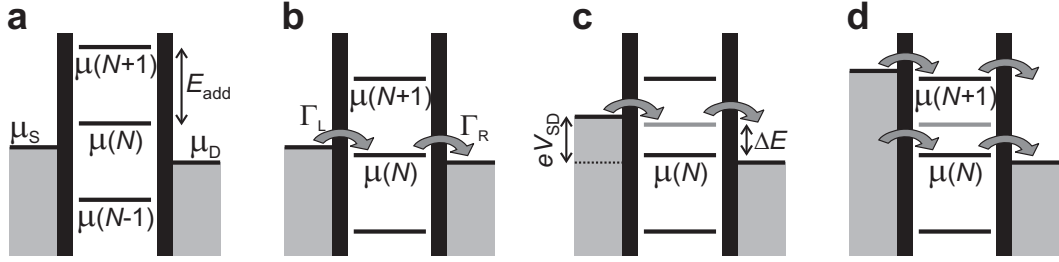
Figure 2.2: Schematic diagrams of the electrochemical potential of the quantum dot for different electron numbers. **a**, No level falls within the bias window between μ_S and μ_D, so the electron number is fixed at $N-1$ due to Coulomb blockade. **b**, The $\mu(N)$ level is aligned, so the number of electrons can alternate between N and $N-1$, resulting in a single-electron tunneling current. The magnitude of the current depends on the tunnel rate between the dot and the reservoir on the left, Γ_L, and on the right, Γ_R. **c**, Both the ground-state transition between $N-1$ and N electrons (black line), as well as the transition to an N-electron excited state (gray line) fall within the bias window and can thus be used for transport (though not at the same time, due to Coulomb blockade). This results in a current that is different from the situation in (b). **d**, The number of electrons can alternate between $N-1$, N, and $N+1$.

the bias window, a current can flow through the device. In Fig. 2.2b $\mu(N)$ is aligned, so the electron number alternates between $N-1$ and N. This means that the Nth electron can tunnel onto the dot from the source, but only after it tunnels off to the drain another electron can tunnel onto the dot from the source. This cycle is known as single-electron tunneling.

By sweeping the gate voltage and measuring the current, we obtain a trace as shown in Fig. 2.3a. At the positions of the peaks, an electrochemical potential level is aligned with the source and drain and a single-electron tunneling current flows. In the valleys between the peaks, the number of electrons on the dot is fixed due to Coulomb blockade. By tuning the gate voltage from one valley to the next one, the number of electrons on the dot can be precisely controlled. The distance between the peaks is proportional to $E_C + \Delta E$, and can therefore give information about the energy spectrum of the dot.

A second way to lift Coulomb blockade is by changing the source-drain voltage, V_{SD} (see Fig. 2.2c). (Typically, the drain potential is kept fixed, and only the source potential is changed.) This increases the bias window and also 'drags' the electrochemical potential of the dot along, due to the capacitive coupling to the source. Again, a current can flow only when an electrochemical potential level falls within the bias window. By increasing V_{SD} until both the ground state and an excited state transition fall in the bias window, an electron can tunnel not only
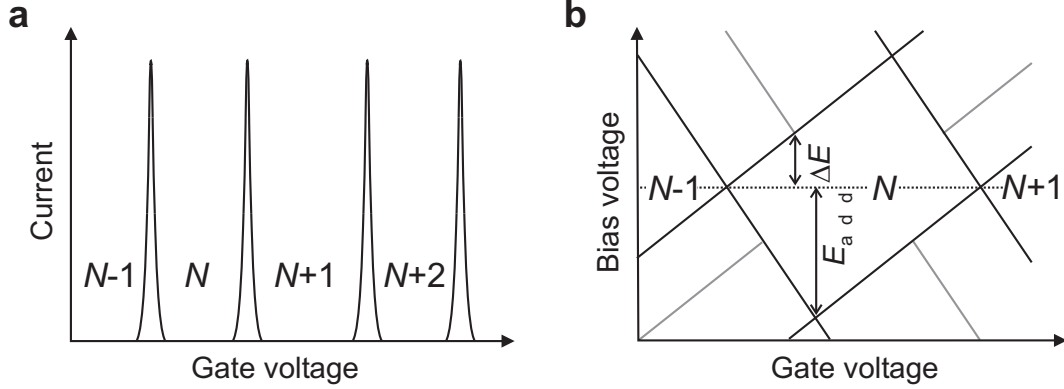
Figure 2.3: Electron transport through a quantum dot. **a**, Coulomb peaks in current versus gate voltage in the linear-response regime. **b**, Coulomb diamonds in differential conductance, dI/dV_{SD}, versus V_{SD} and V_g, up to large bias. The edges of the diamond-shaped regions (black) correspond to the onset of current. Diagonal lines emanating from the diamonds (gray) indicate the onset of transport through excited states.

through the ground state, but also through an excited state of the N-electron dot. This is visible as a change in the total current. In this way, excited-state spectroscopy can be performed.

Usually, the current or differential conductance is measured while sweeping the bias voltage, for a series of different values of the gate voltage. Such a measurement is shown schematically in Fig. 2.3b. Inside the diamond-shaped region, the number of electrons is fixed due to Coulomb blockade, and no current flows. Outside the diamonds, Coulomb blockade is lifted and single-electron tunneling can take place (or for larger bias voltages even double-electron tunneling is possible, see Fig. 2.2d). Excited states are revealed as changes in the current, i.e. as peaks or dips in the differential conductance. From such a 'Coulomb diamond' the energy of excited-states as well as the charging energy can be determined.

The simple model described above explains how quantization of charge and energy result in effects like Coulomb blockade and Coulomb oscillations. Nevertheless, it is over-simplified in many respects. For instance, the model considers only first-order tunneling processes, in which an electron tunnels first from one reservoir onto the dot, and then from the dot to the other reservoir. But when the tunnel rate between the dot and the leads, Γ, is increased, higher-order tunneling via virtual intermediate states becomes important [3]. Such processes, known as 'co-tunneling', can result in a finite current in regimes where first-order tunneling is prohibited due to Coulomb blockade.
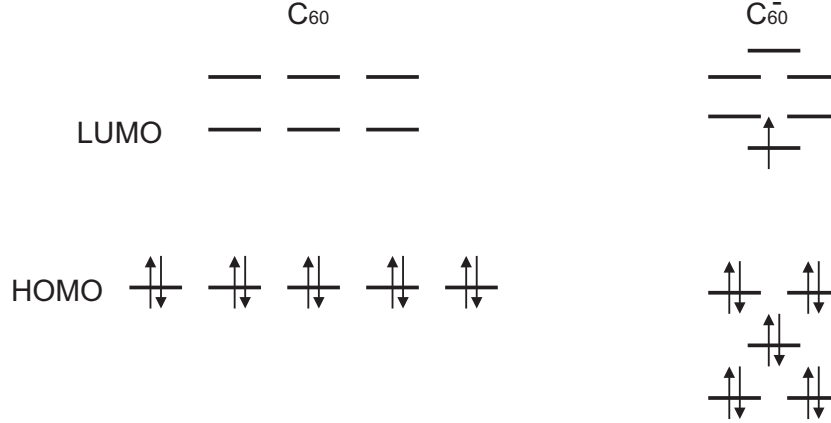
Figure 2.4: Electronic structure of a neutral and reduced C_{60} molecule based on density functional calculations in Ref. [4]. The HOMO-LUMO gap for C_{60} is about 1.65 eV, whereas an extra electron can be added to the same orbital of the charged molecule

2.2 Single-molecule quantum dots

We now consider a single molecule quantum dot. From the previous paragraph we know that the addition energy E_{add} consists of two parts, the charging energy E_c and the level spacing ΔE. For a molecule, the latter is given by the spacing of the molecular orbitals. For an isolated molecule, the level spacing between the highest unoccupied molecular orbital (HOMO) and the lowest unoccupied molecular orbital is often referred to as the HOMO-LUMO gap. In Fig. 2.4 we show the molecular orbitals of both the neutral and the reduced C_{60} molecule. The HOMO-LUMO gap of the neutral molecule is 1.65 eV [4, 5], whereas yet another electron can occupy the same orbital.

For transport, the electrochemical potential of the molecule is important. For a neutral, isolated molecule R with N electrons chemists refer to the ionization energy and electron affinity to denote

$$\mu_{N \to N-1} = U(R) - U(R^+), \qquad \text{(ionization energy)} \tag{2.4}$$

and

$$\mu_{N \to N+1} = U(R^{1-}) - U(R), \qquad \text{(electron affinity)} \tag{2.5}$$

respectively. The addition energy is the difference between these two electrochemical potentials and equals

$$E_{add}^* = E_{HOMO} - E_{LUMO} + E_C^*. \tag{2.6}$$
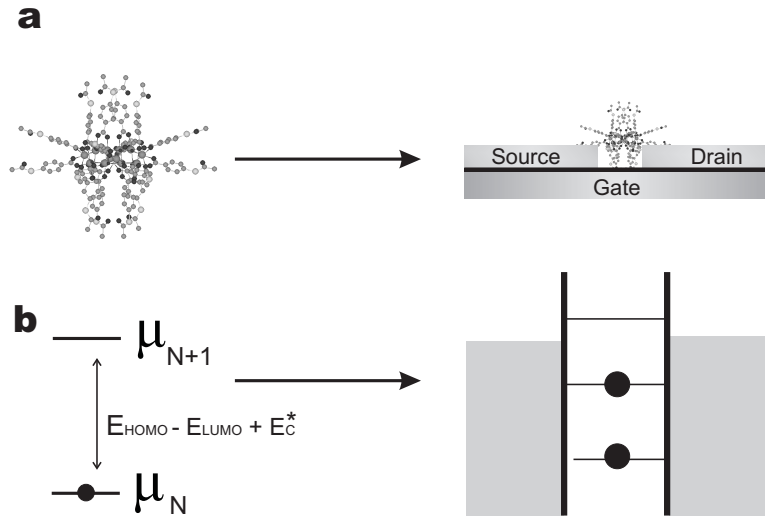
Figure 2.5: When a single molecule (**a**) is weakly contacted by metallic leads it behaves as a quantum dot. **b**, The electronic structure of the isolated molecule is 'compressed' due to screening by the leads.

Here, E^*_{add} and E^*_C denote the addition energy and the charging energy of the isolated molecule.

The situation changes when the molecule is brought into the vicinity of the gold electrodes, see Fig. 2.5. If the molecule is approximated by a metallic sphere of radius r, then the charging energy E^*_C decreases by a factor $(1 - r/R)$, where $R > r$ is the distance between the center of the molecule and the gold. This means that the difference in electrochemical potentials becomes smaller and it ultimately implies that the molecule does not need to be in its 'neutral' state when contacted by leads.

For a simple molecule like C_{60} the metallic sphere approximation may be quite accurate but it certainly breaks down for more complicated molecules, like the manganese-acetate derivative (Mn_{12}) studied in this Thesis. In transition metal complexes, the d-orbitals of the transition metal atoms are usually most easily reduced. Mn_{12} has several equivalent redox-sites. Hence, the concept of the capacitance of the molecule no longer applies and a detailed calculation of the electrostatic environment is necessary to determine the charging energy.

2.2.1 Vibrational excitations

So far we have considered the molecule to be fixed to the leads. In reality, it is not and vibrations of the molecule can also effect its transport properties as demonstrated experimentally by Park *et al.* [6]. Here we discuss an extension of
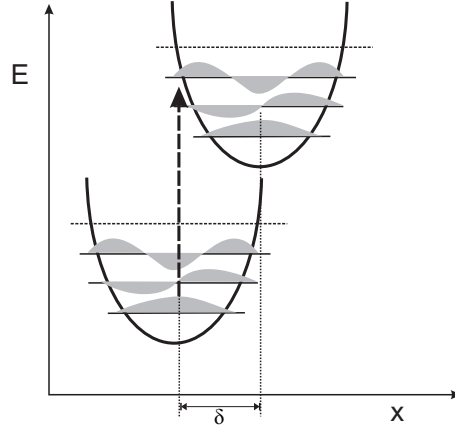
Figure 2.6: Franck-Condon principle. The schematic plot shows vibrational states and their wave functions of the neutral (bottom) and charged molecule (top). Electronic transitions are fast compared to changes in nuclear coordinates (x). Hence, transitions between vibrational states are vertical (arrow) and the corresponding matrix element is given by the wave function overlap.

the constant interaction model to take into account the coupling between electron tunneling and the center of mass motion of the molecule. Vibrational degrees of freedom of the molecule result in i) modification of the tunneling rates and ii) excited states that appear as lines parallel to the Coulomb diamond edge in a $dI/dV(V_g)$ plot.

According to the Franck-Condon principle (Fig. 2.6), electronic transitions are basically instantaneous compared to the time scale of nuclear motions. Semi-classically, this means that transitions between vibrational states before and after electron tunneling can only occur if the nuclear coordinates remain fixed (i.e., transitions are vertical in Fig. 2.6). In a quantum mechanical picture, the transition rates between vibrational states depend on the overlap integral between the corresponding wave functions, the Franck-Condon (FC) factors:

$$P_{mn} = |\langle \Psi_n(x - \delta) | \Psi_m(x) \rangle|^2, \tag{2.7}$$

where $\Psi_m(x)$ denotes the wave function of the molecule in vibrational state m and δ is the displacement of the nuclear coordinate after electron tunneling. Note that $P_{nm} = \delta_{nm}$ for a rigid quantum dot.

The tunneling rates for an electron to source and drain electrodes for a fixed quantum dot are Γ_s and Γ_d, restrictively, which are determined by electron wave function overlap between leads and quantum dot. For a molecule, we also need to take into account the Franck-Condon factors. This means

$$\Gamma_{s(d)} \rightarrow \Gamma_{s(d)} P_{00}, \tag{2.8}$$

a

M=-7
M=-8
M=-9
M=-10

M=7
M=8
M=9
M=10

b

M

B
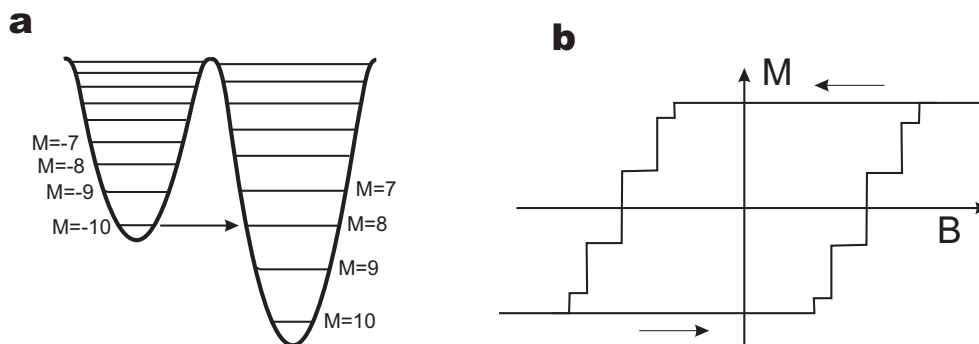
Figure 2.7: a, Energy spectrum of a single molecule magnet with $S = 10$, in the presence of a magnetic field along the easy axis of the molecule. Quantum tunneling of the magnetization (QTM) can occur at values of the magnetic field where the $M = -10$ state becomes aligned with an M state at the other side of the potential barrier. **b**, QTM results in steps in the magnetization curve of Mn_{12} crystals at those values of the magnetic field where the tunneling probability is highest.

for the ground state to ground state transition. When the molecule is bound by an harmonic oscillator potential with the same force constant before and after tunneling the FC factors can be readily calculated and $P_{00} = e^{-(\delta/x_0)^2/2}$, where x_0 is the ground state vibrational amplitude. The coupling of the vibrational ground state of the uncharged molecule to vibrational excited states of the charged molecule increases when δ becomes larger, whereas the ground state to ground state transition is suppressed.

2.3 Single molecule magnets

Although magnetism generally is a bulk property, the spins of the transition-metal ions of a single molecule magnet (SMM) are so strongly exchange coupled that at low temperatures each molecule behaves as a single-domain ferromagnetic particle. The best known, and first discovered, SMM is manganese-acetate (Mn_{12}) [7]. It consists of 8 ferromagnetically coupled Mn^{3+} ions ($S = 2$) that are ferrimagnetically coupled to 4 Mn^{4+} ions ($S = 3/2$) giving Mn_{12} a total spin $S = 10$. Mn_{12} has a large anisotropy barrier that aligns the total spin parallel or anti-parallel to an intrinsic axis, the z-axis. The projection of S on the z-axis, can be in any of the $2S + 1$ different M states, and the spin state of the molecule is labeled by the quantum numbers $|S, M\rangle$. The system can be modeled by the Hamiltonian

$$H = -|D|S_z^2 + B_2(S_x^2 - S_y^2),$$
(2.9)

where D is the anisotropy constant. The second term provides a weak coupling between otherwise orthogonal spin states, allowing for quantum tunneling of the magnetization (QTM). The Hamiltonian gives rise to a ladder of spin states (Fig. 2.7) where, in the absence of a magnetic field, the M and $-M$ states are pairwise degenerate. The spin ground states of the molecule, $|10, 10\rangle$ and $|10, -10\rangle$, are separated by an energy barrier of DS^2, the magnetic anisotropy barrier (MAP), which corresponds to about 6 meV for Mn_{12}. Spin manifolds for which the total spin S is smaller have a higher energy. The groundstate energy Δ=4 meV of the $S' = 9$ spin manifold [8] is smaller than the MAB, $DS^2 < \Delta$, meaning that the two spin manifolds overlap in energy.

Crystals of Mn_{12} molecules show a step-wise, hysteretic magnetization curve, Fig. 2.7. An external magnetic field parallel to the easy axis of the molecule shifts the energy levels with respect to each other. The steps in the magnetization correspond to resonances in the relaxation rate when the levels at opposite sides of the energy barrier are aligned. At the associated magnetic field values, quantum tunneling can reverse the spin direction.

2.3.1 Transport through single molecule magnets

When electrons are added or subtracted from the Mn_{12} molecule in the Coulomb blockade regime, the total spin of the molecule has to change. Since the spin of an electron is $|s, m\rangle = |\frac{1}{2}, \pm\frac{1}{2}\rangle$, the ground state spin manifold of the charged molecule has spin $S_{n+1}, M_{n+1} = 10 \pm \frac{1}{2}$. By subsequent electron tunnel processes the molecule can also reach spin excited states due to the relatively long spin relaxation rates. Similar to the Franck-Condon factors for vibrations, the Clebsch-Gordan coefficients (CGC) determine the transition rates between different spin states:

$$C^{S_{n+1},M_{n+1}}_{S_n,M_n,s,m} = \langle S_{n+1}\ M_{n+1}|S_n\ M_n\ s\ m\rangle. \tag{2.10}$$

All spin transitions that do not obey the spin selection rules $S_{n+1} = S_n \pm \frac{1}{2}$ and $M_{n+1} = M_n \pm \frac{1}{2}$ have zero CGC.

Apart from the above spin conservation the usual energy conservation rules apply for excited state transitions. However, M states become closer in energy for smaller values of M. This means that when the ground state to first excited state transitions become energetically allowed, all excited to excited state transitions (that fulfill spin selection rules) are also allowed. Excited state lines in the $dI/dV(V_g)$ plot therefore no longer correspond to a single transition, but rather to a series of subsequent transitions. Numerical calculations are required to predict how excited state transitions contribute to the conductance of the molecule.
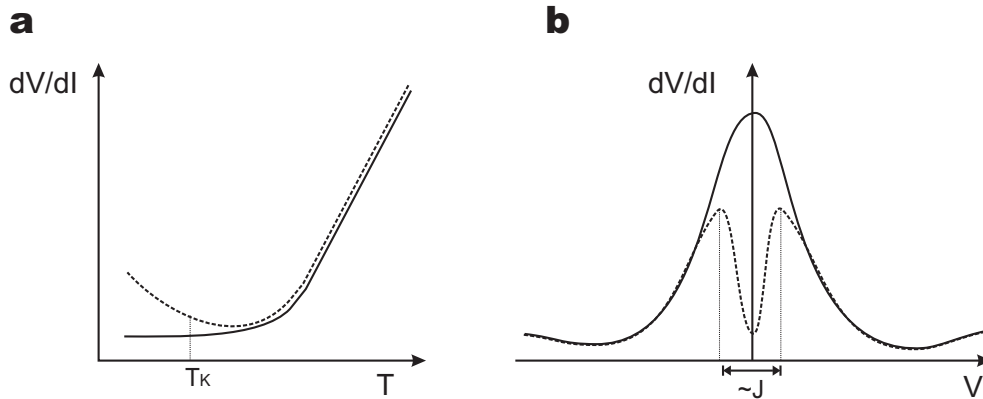
Figure 2.8: **a**, Temperature dependence of the zero bias differential resistance of a metal with (dashed line) and without (solid line) a low concentration of magnetic impurities. As a result of the Kondo effect, the differential resistance increases for decreasing temperatures below the Kondo temperature T_K. **b**, The signature of the Kondo effect is a peak in dV/dI around zero bias voltage (solid line). The width of the peak is a measure for T_K. RKKY exchange interactions suppress the Kondo effect on the energy scale of the average exchange interaction strength J (dashed line).

Although the calculations depend on the precise parameters rather sensitively, some generic features can be observed. These are discussed in more detail in Chapter 6.

2.4 The Kondo effect

The Kondo effect in metals arises from an interaction between the spin of a magnetic impurity atom (cobalt, for example) and the conduction electrons of the otherwise nonmagnetic host metal (eg. gold). In this paragraph we discuss the Kondo effect closely following Ref. [9]

For normal metals, the resistance decreases when the temperature is lowered since electron-phonon scattering is suppressed. Below a certain temperature, defects in the material form the dominant scattering mechanism and the resistance saturates, Fig. 2.8. However, the temperature dependence changes considerably when a low concentration of magnetic impurities are added to the material. Instead of saturating, the resistance now increases when the temperature is lowered further. This effect was first observed in the 1930's but not understood until 1964, when the Japanese theorist Jun Kondo provided an explanation. The effect is now referred to as the Kondo effect.

The Kondo effect in metals occurs because below the so called Kondo temperature $T_K = We^{-1/(\rho J)}$ (W is the bandwidth, ρ is the density of states, and J

the exchange coupling), the conduction electrons in the host metal tend to screen the non-zero total spin of the electrons in the magnetic impurity atom. In the simplest model of a magnetic impurity, introduced by Anderson in 1961, there is only one electron level with energy ϵ_0 and the impurity spin is 1/2. Exchange processes can effectively flip the impurity spin, while simultaneously creating a spin excitation in the Fermi sea. This spin exchange changes the energy spectrum of the system. When many such processes are added coherently, a new state - the Kondo resonance - is generated at the Fermi energy. Since electrons at the Fermi energy are responsible for conductivity of a metal, the strong spin scattering contributes greatly to the resistance. The Kondo effect is a many body phenomenon; the whole system - that is, the magnetic impurity plus the surrounding electrons - form a spin singlet state.

2.4.1   Kondo effect in quantum dots

A quantum dot connected to source and drain leads, can mimic the above situation of a localized spin impurity in a Fermi sea. In 1988, it was realized that the same Kondo effect should occur (at low temperatures) in quantum dots with a net spin [10, 11]. However, in quantum dots the scattering resonance is manifested as an increased probability for scattering from the source to the drain reservoir, i.e. as an increased conductance.

The transport mechanism we described in section 2.1, was sequential tunneling. This first-order tunneling mechanism gives rise to a current only at the Coulomb peaks, with the number of electrons on the dot being fixed between the peaks. This description is quite accurate for a dot with very opaque tunnel barriers. However, for stronger coupled dots, with a tunnel barrier resistance comparable to the resistance quantum, $R_Q \equiv h/e^2 = 25.8$ kΩ, higher-order tunneling processes have to be taken into account. These lead to quantum fluctuations in the electron number, even when the dot is in the Coulomb blockade regime.

An example of such a higher-order tunneling event is shown in Fig. 2.9a. Energy conservation forbids the number of electrons to change, as this would cost an energy of order E_C. Nevertheless, an electron can tunnel off the dot, leaving it temporarily in a classically forbidden 'virtual' state (middle diagram in Fig. 2.9a). This is allowed by virtue of Heisenberg's energy-time uncertainty principle, as long as another electron tunnels back onto the dot immediately, so that the system returns the energy it borrowed. The final state then has the same energy as the initial one, but one electron has been transported through the dot. This process is known as elastic 'cotunneling' [3].

If the electron spin is taken into account, then events such as the one shown
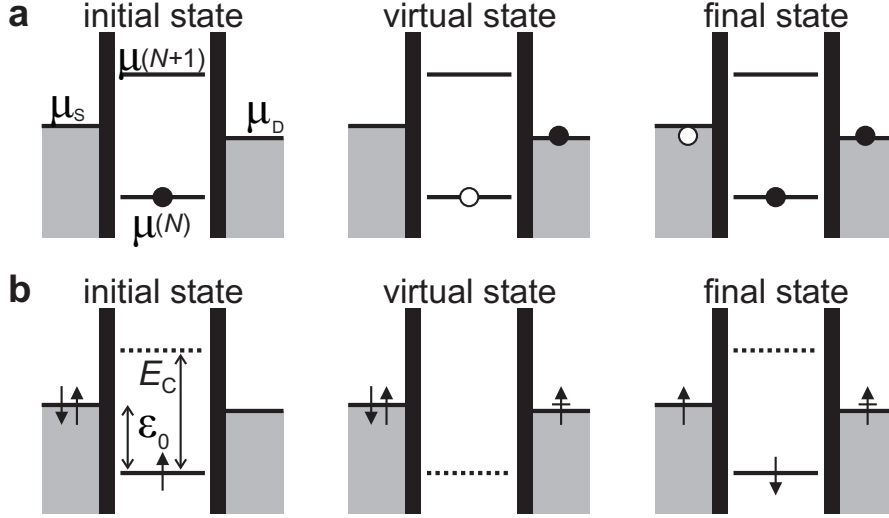
Figure 2.9: Higher-order tunneling events overcoming Coulomb blockade. **a**, Elastic cotunneling. The Nth electron on the dot jumps to the drain to be immediately replaced by an electron from the source. Due to the small bias, such events give rise to a net current. **b**, Spin-flip cotunneling. The spin-up electron jumps out of the dot to be immediately replaced by a spin-down electron. Many such higher-order spin-flip events together build up a spin singlet state consisting of electron spins in the reservoirs and the spin on the dot. Thus, the spin on the dot is screened.

in Fig. 2.9b can take place. Initially, the dot has a net spin up, but after the virtual intermediate state, the dot spin is flipped. Unexpectedly, it turns out that by adding many spin-flips events of higher orders coherently, the spin-flip rate diverges. The spin on the dot and the electron spins in the reservoirs are no longer separate, they have become *entangled*. The result is the appearance of a new ground state of the system as a whole – a spin singlet. The spin on the dot is thus completely screened by the electron spins in the reservoirs.

The Kondo effect appears below the so-called Kondo temperature, T_K, which corresponds to the binding energy of the Kondo singlet state. It can be expressed in terms of the dot parameters as

$$T_K = \frac{\sqrt{h\Gamma E_C}}{2k_B}e^{\pi\varepsilon_0(\varepsilon_0+E_C)/h\Gamma E_C} \tag{2.11}$$

where Γ is the tunnel rate to and from the dot, and ε_0 is the energy level on the dot relative to the Fermi energy of the reservoirs. The great advantage of using quantum dots, in general, to study the Kondo effect, is that they allow these parameters to be tuned *in situ*.

The main characteristics of the Kondo effect in transport through a quantum dot are schematically depicted in Fig. 2.10. For an odd number of electrons on
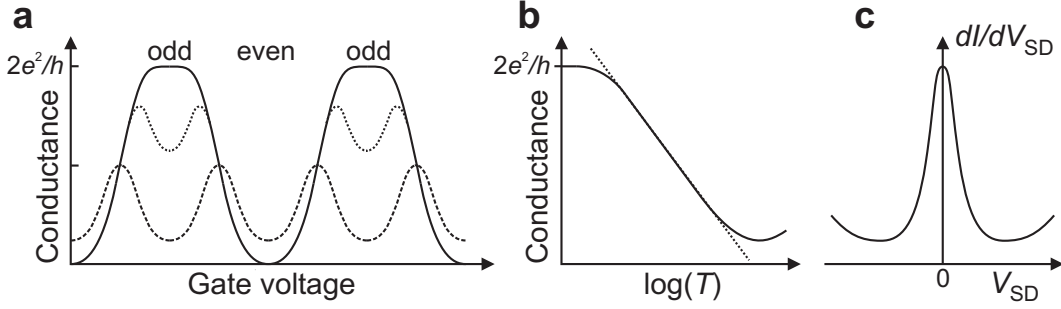
Figure 2.10: Schematic representation of the main characteristics of the Kondo effect in electron transport through a quantum dot. **a**, Linear conductance versus gate voltage, for $T \ll T_K$ (solid line), $T \lesssim T_K$ (dotted line), and $T \gg T_K$ (dashed line). the Kondo effect only occurs for odd electron number, resulting in an odd-even asymmetry between the different Coulomb valleys. **b**, In the odd ('Kondo') valleys the conductance increases logarithmically upon lowering the temperature, and saturates at $2e^2/h$. **c**, The Kondo resonance leads to a zero-bias resonance in the differential conductance, dI/dV_{SD}, versus bias voltage, V_{SD}.

the dot, the total spin S is necessarily non-zero, and in the simplest case $S = 1/2$. However, for an even electron number on the dot – again in the simplest scenario – all spins are paired, so that $S = 0$ and the Kondo effect is not expected to occur. This 'even-odd-asymmetry' results in the temperature dependence of the linear conductance, G, as shown in Fig. 2.10a. In the 'odd' or 'Kondo' valleys the conductance increases as the temperature is lowered, due to the Kondo effect. In the 'even' valleys, on the other hand, the conductance decreases, due to a decrease of thermally excited transport through the dot.

The temperature dependence of the conductance in the middle of the Kondo valleys is shown in Fig. 2.10b. The conductance increases logarithmically with decreasing temperature [10], and saturates at a value $2e^2/h$ at the lowest temperatures [11, 12]. Although the charging energy tends to block electrons from tunneling on or off, the Kondo effect enables electrons to pass unhindered through the dot. This complete transparency of the dot is known as the 'unitary limit' of conductance [13]. The Kondo resonance at the Fermi energy of the reservoirs is manifested as a zero-bias resonance in the differential conductance, dI/dV_{SD}, versus V_{SD}, as shown in Fig. 2.10c. The full width at half maximum of this resonance gives an estimate of the Kondo temperature.
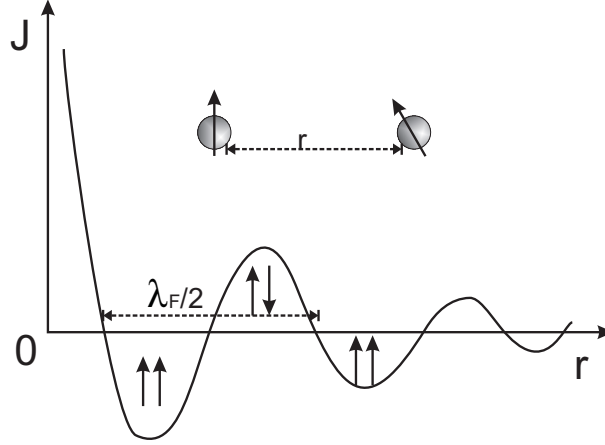
Figure 2.11: RKKY interaction strength J between two spins embedded in a Fermi sea and separated by a distance r. Depending on the separation, the interaction is ferromagnetic or anti-ferromagnetic.

2.5   RKKY interaction between spins

In the previous paragraph, we saw that a low concentration of magnetic impurities in a non-magnetic metal can result in an increase in the resistance due to the Kondo effect. However, for high concentrations of magnetic impurities the Kondo effect is absent. The reason is that spin-flip processes with the conduction electrons are suppressed due to a coupling between the spins of the impurities. Since direct spin-spin interaction is negligible on distances larger than a few atoms there must be another interaction mechanism. This is the indirect, or Ruderman-Kittel-Kasuya-Yosida (RKKY), exchange interaction.

The two impurity spins interact with each other via the conduction electrons of the metal. The interaction is the result of 'screening' of the impurity spin by the conduction electrons, resulting in oscillatory spin density rings around the impurity (Friedel oscillations). When a second impurity is placed in the vicinity of the first, spin density oscillations interfere, resulting in a net interaction. Depending on the separation, the interaction tends to align (ferromagnetic interaction) or anti-align (anti-ferromagnetic interaction) the impurity spins to form a triplet or singlet state, respectively.

The strength and *sign* of the interaction J_{RKKY} oscillates as a function of the separation r between the two spins (Fig. 2.11),

$$J_{RKKY} \sim J_1 J_2 r^{-4}[k_F r \cos(2k_F r) - \sin(2k_F r)], \qquad (2.12)$$

where J_i is the interaction strength between spin S_i with the conduction electrons. A metal with many interacting magnetic impurities is called a spin glass: a pe-

culiar system that has many ground states and is characterized by long magnetic relaxation times (months).

The competition between the Kondo effect and RKKY interactions has been studied in mechanical breakjunctions [14]. The high resistance of thin gold wires makes them suitable for measuring small relative changes in the resistance. With a low concentration of magnetic impurities, the resistance of the breakjunctions has a peak around zero bias voltage due to the Kondo-effect, Fig. 2.8. For higher concentrations, where the impurities start to interact, the Kondo peak in resistance is suppressed at very low bias. The result is an apparent 'split' Kondo peak.

Quantum dots, which can act as artificial magnetic impurities, can be used to study the competition between the Kondo effect and RKKY interactions in a controlled way. Recently, Craig *et al.* [15] coupled two quantum dots, defined by gates on a semiconductor heterostructure, via a common open conducting region. When decoupled, the quantum dots each showed an enhancement of the conductance around zero bias voltage due to the Kondo effect. In this first experimental realization of the two impurity Kondo problem, the authors found that the strength of the non-local RKKY interaction can be used to control the Kondo effect in one dot by tuning gate parameters of the other dot. This opens the way for exchange coupling quantum dots beyond the constraint of nearest neighbor interaction.

From the experiment by Craig *et al.* the sign of the interaction cannot be determined. Both ferromagnetic and anti-ferromagnetic interactions result in the suppression of the $s = 1/2$ Kondo effect. Although the triplet ($s = 1$) state, that is formed by coupling the spins ferromagnetically, can be Kondo screened, its characteristic Kondo temperature is much smaller than the Kondo temperature related to the $s = 1/2$ Kondo effect. In Chapter 7 we study the interaction between real magnetic impurities and a gold grain quantum dot in a all metal system. In this experiment we observe a suppression of the Kondo effect of the dot as a result of RKKY interaction between the spin on the dot and magnetic impurities in its vicinity. By applying an magnetic field we are able to distinguish between ferro- and anti-ferromagnetic interactions.

2.6 Graphene

In this paragraph we discuss the transport properties of graphene - a single layer of graphite. Starting from its bandstructure, we derive the anomalous quantization of the quantum Hall effect. We also consider the normal state conductance as a
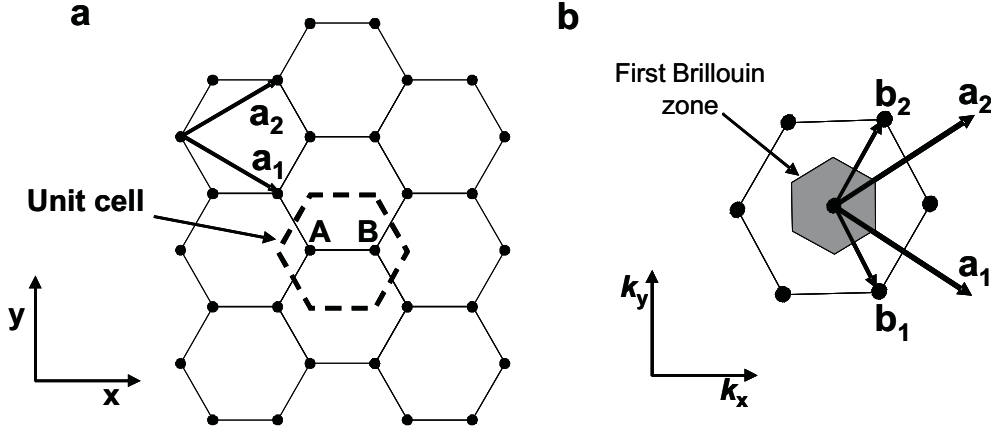
Figure 2.12: a, Real space atomic lattice of graphene with lattice vectors $\mathbf{a}_1$ and $\mathbf{a}_2$. The unit cell contains two inequivalent carbon atoms A and B. **b**, Reciprocal space lattice points (dots) and the hexagonal first Brillouin zone (shaded).

function of gate voltage, which is still not well understood. Finally we discuss the effective breaking of time reversal symmetry in graphene.

2.6.1 Graphene bandstructure

The special electrical properties of graphene can be derived from its bandstructure. Graphene is a 2-dimensional, conjugated sheet of carbon atoms that are arranged in a honeycomb shaped lattice. Each carbon atom has four valence electrons. Three of those occupy the the planar sp^2 hybrid orbital to form covalent in-plane (σ)-bonds. The remaining electron occupies a p_z orbital (the z-axis is perpendicular to the plane). Overlap between p_z orbitals results in free electrons which can contribute to the electrical conductivity.

The triangular Bravais lattice of graphene has two basis atoms, labeled A and B, Fig. 2.12a. All other lattice sites are translations over the primitive vectors $\mathbf{a}_1$ and $\mathbf{a}_2$. The reciprocal lattice is again triangular with a hexagonal first Brillouin zone, see Fig. 2.12b. The lattice vectors in reciprocal space are $\mathbf{b}_1$ and $\mathbf{b}_2$.

The band structure can be calculated to first approximation using a tight binding Hamiltonian [16]:

$$H = -t \sum_{i,j} \left(A^{\dagger}_{\mathbf{R_i}} B_{\mathbf{R_i}+\delta_{\mathbf{j}}} + B^{\dagger}_{\mathbf{R_i}+\delta_{\mathbf{j}}} A_{\mathbf{R_i}} \right), \tag{2.13}$$

where $\mathbf{R_i}$ denote the position of the lattice points in real space, and $\delta_{\mathbf{j}}$ are the vectors connecting an A atom to its neighboring B atoms. $A^{\dagger}$ (A) and $B^{\dagger}$ (B)denote
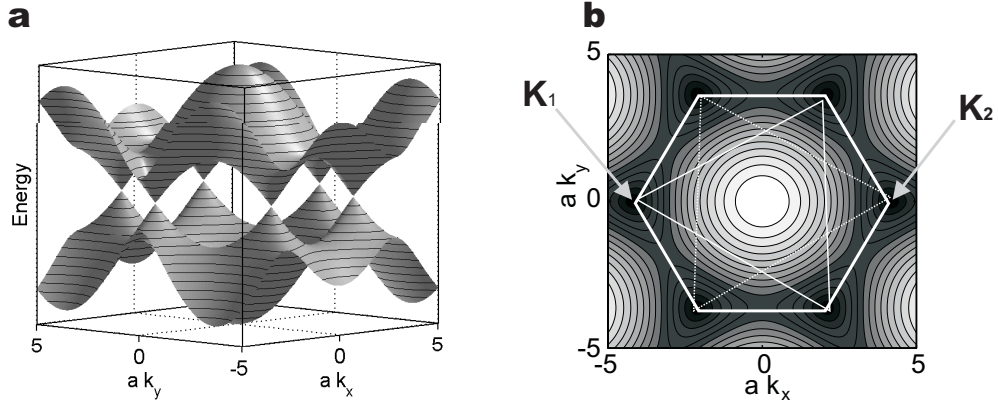
Figure 2.13: a, Graphene bandstructure $E(k_x, k_y)$. Conduction and valence band touch at six points, the K-points. The Fermi energy for undoped graphene lies exactly at these points. **b**, Contour plot of the conduction band (darker indicates lower energy). The hexagon formed by six K-points (black dots) defines the first Brillouin zone of the graphene band structure. The inequivalent K-points, $\mathbf{K}_1$ and $\mathbf{K}_2$, are indicated. Triangles connect the equivalent K-points.

the creation (annihilation) operators for an electron at an A or B atom, respectively, while t denotes the energy overlap integral. The Hamiltonian acts on the wave function:

$$|\Psi\rangle = \left[\alpha_k \sum_i \left(e^{i\mathbf{k}\cdot\mathbf{R_i}} A^{\dagger}_{\mathbf{R_i}} \right) + \beta_k \sum_i \left(e^{i\mathbf{k}\cdot(\mathbf{R_i}+\delta)} B^{\dagger}_{\mathbf{R_i}+\delta} \right) \right] |0\rangle, \tag{2.14}$$

where $|0\rangle$ denotes the vacuum state and α_k and β_k refer to the wave function amplitude on A and B atom sites.

The bandstructure of graphene follows fairly straightforwardly by solving:

$$H|\Psi\rangle = E(k_x, k_y)|\Psi\rangle. \tag{2.15}$$

We omit the lengthy formula (see eg. [17]), but $E(k_x, k_y)$ is plotted in Fig. 2.13a. The bonding and anti-bonding solutions (valance and conduction bands) touch at six points that coincide with the corners of the first hexagonal Brillouin zone. Since there are two valence electrons per unit cell, the Fermi surface reduces to just these six points, which are called 'K'-points. The dispersion relation near a K-point is discussed in the next paragraph.

Figure 2.13b shows a contour plot of the energy of the valence band states. The circular contours around the K points reflect the conical shape of the dispersion relation around them. Only two of the six K-points are inequivalent, labeled

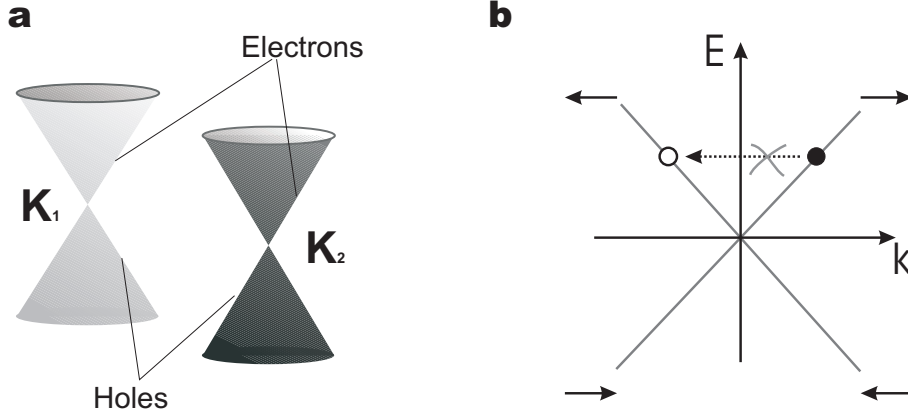**Figure 2.14:** Small k approximation. **a,** The conical approximation of the band structure around the two inequivalent K-points. In the absence of intervalley scattering, the two subbands or valleys are independent. **b,** Projection of one of the two cones on an arbitrary $k - E$ plane. The arrows denote the pseudo spin which is always aligned (anti-aligned) to **k** for electrons (holes). Scatter processes that do not conserve pseudo-spin are not allowed (dashed arrow).

.

$\mathbf{K}_1$ and $\mathbf{K}_2 = -\mathbf{K}_1$. The other 4 K-points in Fig. 2.13b, can be reached by a suitable reciprocal lattice vector translation from $\mathbf{K}_1$ or $\mathbf{K}_2$.

The electronic properties of a conductor are determined by the electrons near the Fermi energy. Therefore the shape and position of the dispersion cones near the K points is of fundamental importance in understanding electronic transport in graphene. The two K points, $\mathbf{K}_1$ and $\mathbf{K}_2$ in Fig. 2.13b have coordinates $(k_x, k_y) = (\pm 4\pi/3a, 0)$. The slope of the cones is $(\sqrt{3}/2)ta$, where $t \sim 2.7$ eV is the energy overlap integral between nearest neighbor carbon atoms [18].

2.6.2 Expansion around $\mathbf{K_1}$

For transport measurements we are most interested in the dispersion relation in a small energy range around the Fermi energy. From the dispersion relation the Fermi velocity (proportional to the first derivative) can be readily obtained. For small energies, the Hamiltonian can be approximated around one of the K-points (say $\mathbf{K_1}$). In the remainder of the text, **k** denotes the position in k-space with respect to $\mathbf{K_1}$. When we expand Eq.2.15 around $\mathbf{K_1}$ we obtain:

$$-\hbar v_F \begin{pmatrix} 0 & k_x - ik_y + O(\mathbf{k}^2) \\ k_x + ik_y + O(\mathbf{k}^2) & 0 \end{pmatrix} \begin{pmatrix} \alpha_k \\ \beta_k \end{pmatrix} = E(\mathbf{k}) \begin{pmatrix} \alpha_k \\ \beta_k \end{pmatrix}, \quad (2.16)$$

which is a 2+1-dimensional Dirac-equation. The solution is $E(\mathbf{k}) = \pm \hbar v_F k$ which corresponds to a cone-shaped band, Fig. 2.14a. For undoped graphene, the Fermi energy lies at the apex of this cone, where electrons and holes are degenerate. Due to the linear spectrum, the electrons behave as relativistic particles with zero rest mass and constant (k-independent) velocity $v_F \approx 10^6$m/s. This is what makes graphene special compared to conventional 2DEGs in which electrons are massive and have an energy dependent Fermi velocity.

Eq. 2.16 can also be written as:

$$-\hbar v_F \mathbf{k} \cdot \overrightarrow{\sigma} \begin{pmatrix} \alpha_k \\ \beta_k \end{pmatrix} = E(\mathbf{k}) \begin{pmatrix} \alpha_k \\ \beta_k \end{pmatrix}, \tag{2.17}$$

where $\overrightarrow{\sigma}$ denotes the vector of Pauli matrices. The spinor $(\begin{array}{cc} \alpha_k & \beta_k \end{array})^T$ is often referred to as *pseudo spin*. Unlike the real spin, the pseudo spin is tight to $\mathbf{k}$. The pseudo spin of an electron is aligned with $\mathbf{k}$ whereas the pseudo spin of a hole is anti-aligned, Fig. 2.14b. This has important implications when an electron travels in a closed loop in real space (eg. a cyclotron orbit). Similar to a real spin that is rotated adiabatically over a full circle, the wave function picks up a phase of π. This phase is referred to as Berry's phase.

2.6.3 Anomalous quantum Hall effect

When a magnetic field is applied, the continuous density of states of graphene collapses in discrete Landau levels (LL). In a semi-classical picture, LL correspond to those cyclotron orbits that enclose an integer number of flux quanta, $\Phi_0 = h/e$. In this way, the electron wave-function gains a phase factor of $2\pi n$ and self-interferes constructively. Therefore, the Landau level degeneracy is gB/Φ_0, where g is the spin degeneracy. In graphene, electrons pick up an additional Berry's phase of π upon completing a cyclotron orbit (see previous paragraph), and hence the cyclotron orbit that corresponds to the first LL only encloses flux $\Phi_0/2$. This results in degeneracy $gB/(2\Phi_0)$ for the first LL and gB/Φ_0 for subsequent LLs [19](In graphene, $g = 4$ due to spin and valley degeneracy).

As a consequence of the halved degeneracy of the first LL, the quantization of the Hall conductance G_{Hall} is anomalous [21, 22], see Fig. 2.15. Plateaus in G_{Hall} occur at half-integer values of $4e^2/h$:

$$G_{Hall} = (n + \tfrac{1}{2})\tfrac{4e^2}{h}. \tag{2.18}$$

The experimental observation of the anomalous quantization of G_{Hall} is a clear signature of single layer graphene [19, 20], since the Hall conductance of bilayer graphene has plateaus at integer values.
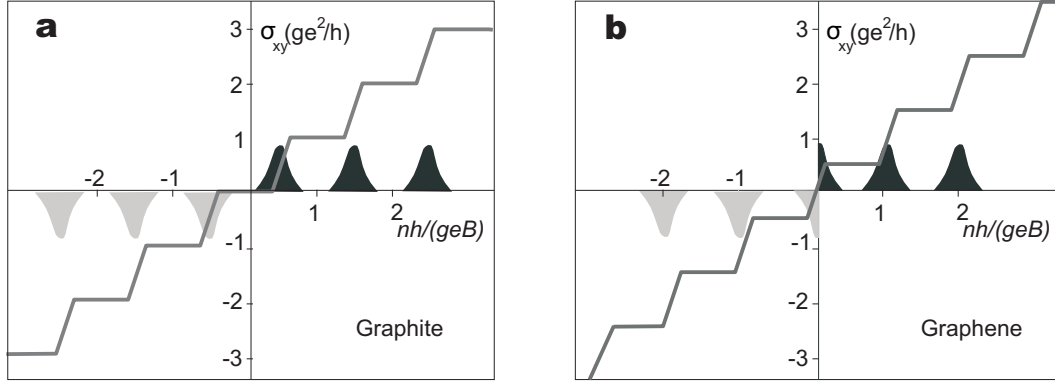
Figure 2.15: Integer quantum Hall effect. Hall conductivity $\sigma_{xy} \equiv \rho_{xy}/(\rho_{xy}^2 + \rho_{xx}^2)$ is plotted as a function of density n for **a**, graphite (or conventional quantum Hall systems) where plateaus occur at $\sigma_{xy} = N(ge^2/h)$, and **b**, graphene with anomalous half integer quantization, $\sigma_{xy} = (N + \frac{1}{2})(ge^2/h)$. The shaded areas along the density axis represent the sequence of Landau levels. The degeneracy of each LL is given by gBe/h, except for the first Landau level of graphene, which has half this degeneracy.

For free-fermion quantum Hall systems, the Landau level energies are $E_N = \hbar\omega_c(N + \frac{1}{2})$ and the lowest states lies at finite energy. In graphene, the Landau level energies E_N can be calculated by substituting the momentum by the canonical momentum operator $\hbar\mathbf{k} \rightarrow (i\hbar\overrightarrow{\nabla} + \mathbf{A})$ in Eq. 2.17. The resulting levels have energies $E_N = \pm v_F\sqrt{2e\hbar BN}$. The lowest LL occurs at $E_0 = 0$ and is filled with both electrons and holes. Note that, whereas the energy spacing between LL is constant for free-fermion quantum Hall systems, the energy spacing of LL in graphene becomes smaller for larger N. Furthermore, the energy spacing of the first LL is much larger compared to conventional quantum Hall systems, so that the quantum Hall plateaus can be observed at much higher temperatures (and in fact even up to room temperature).

2.6.4 Conductance of graphene

As a result of the Dirac-like nature of the charge carriers in graphene, even its most elementary properties, like the conductance, are being debated. The carrier concentration in graphene is tunable with a back-gate and hence the conductance can be studied as a function of carrier density. Two surprising observations were made in the first experiments in which the conductivity of graphene was measured [19, 20].

First of all, in the doped regime, the dependence of the conductivity on density n (and hence on gate voltage, since $n \propto V_g$) appeared to be linear, $G(n) \propto n$,

while no density dependence was predicted based on the Bolzmann conductivity [23, 24]. This observation indicates that the mobility $\mu = \sigma/ne$ is constant at high doping. Smooth intravalley scattering that could be Coulombic in nature can explain the linear dependence of σ on n.

The second surprise is the observation of a minimum conductivity of $4e^2/h$ when the Fermi level lies at the Dirac point (no doping) [19]. As the density of states vanishes at Dirac point, one might expect the conductivity to vanish identically. The conductivity at the Dirac point is still under debate, a discussion in which the role of intervalley scattering plays an important role [24, 25]. Furthermore, the effect of disorder and finite temperature and bias voltage are to be evaluated further.

The experimental observations discussed above were all made in the diffusive regime, where the sample length exceeds the mean free path $L >> l_e$. In Chapter 8 we discuss the first experiments in the semi-ballistic limit, where $L \sim l_e$. The conductance in this regime has been calculated by Tworzydlo *et al.* [26] based on a Landauer-Büttiker approach. Surprisingly, they find that $\sigma \equiv G \times L/W \simeq 4e^2/(\pi h)$ (W denotes the width of the sample) at the Dirac point ($W \gtrsim L$), whereas in conventional ballistic 2DEGs the conductance is independent of the length of the sample. Furthermore, they predict a square-root dependence of the conductance on density. It should be noted, however, that the calculations assume the absence of intervalley scattering.

2.6.5   Time-reversal symmetry

Although one would expect the Hamiltonian of graphene to be time-reversal symmetric, implying $E(\mathbf{k}) = E(-\mathbf{k})$ in the absence of a magnetic field and spin orbit interaction. This seems to be in contrast with Eq. 2.16 if second order terms are taken into account. This paradox is solved when we realize that Eq. 2.16 describes the physics of one sub-band or valley and the total Hamiltonian is time-reversal symmetric. Nevertheless, in perfect graphene, the two valleys (Fig. 2.14a) are independent and charge-carriers remain in the same valley. Therefore, although time-reversal symmetry (TRS) of graphene as a whole is conserved, charge carriers might experience effective TRS breaking even in the absence of a magnetic field.

Although the effective TRS breaking due to second order corrections to the Hamiltonian is weak for low energies (small k), imperfections in graphene can also result in effective TRS breaking [27, 28]. Ripples in the graphene sheet, for example, have the same result as applying a magnetic field (0.1-1 T for typical corrugations) and hence breaking of TRS. Other effective TRS breaking mecha-
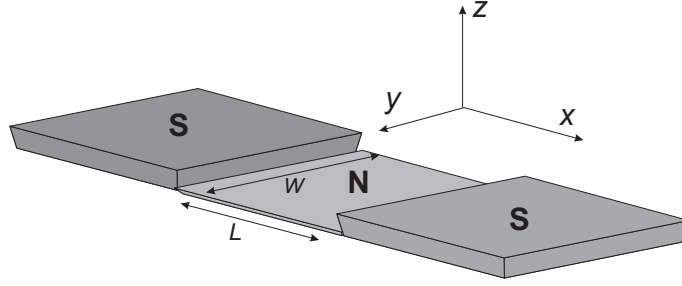
Figure 2.16: Josephson junction consisting of two superconductors (S) coupled by a non-superconducting material (N).

nisms are lattice defects and potential gradients. Short range interactions, on the other hand, result in intervalley scattering and hence couple the two sub-bands. These intervalley scattering events take place on a characteristic time-scale τ_{inv} that should be compared to other relevant time-scales of the system, in particular the phase coherence time τ_ϕ.

In an experiment, the effective breaking of TRS can be inferred from, for example, weak localization (or coherent backscattering) experiments [27]. Weak localization (WL) is a well-studied effect in conventional 2DEGs and leads to an enhancement of the resistance at zero magnetic field. An external magnetic field breaks TRS and hence results in a negative magneto-resistance. In perfect graphene, weak anti-localization (WAL) instead of WL is expected [28, 29], due to the Berry's phase. However, intervalley scattering suppresses WAL (restoring WL) when $\tau_{inv} < \tau_\phi$ and imperfections that lead to effective TRS breaking suppress WAL not restoring WL. It should be noted that both intervalley scattering and imperfections that lead to effective TRS breaking are sample specific. Hence, the magneto-resistance that is observed in an experiment may differ from sample to sample.

2.7 Superconductivity

In this section we provide a brief introduction to superconductivity related phenomena that are important for the experimental work in Chapter 8. As we will see, graphene gives a new twist to some of the well known processes like, for example, Andreev reflection.

2.7.1   Josephson effect

In 1911, Kamerling Onnes discovered that mercury can conduct electrical current without electrical resistance when cooled to sufficiently low temperatures [30]. This phenomena, now known as superconductivity, was explained half a century later by Bardeen, Cooper, and Schrieffer (BCS) in terms of the condensation of electrons into Cooper-pairs that are all described by the same quantum state [31]. This quantum state has the condensate wave function:

$$\Psi = |\Psi|e^{i\phi_s}, \tag{2.19}$$

where ϕ_s is the macroscopic quantum phase and $|\Psi|$ is a measure of Cooper pair density. In 1962, Josephson predicted that a supercurrent can even flow through a thin insulating oxide layer separating two superconductors [32]. The magnitude of the Josephson supercurrent I_{sc} depends on the phase difference between the phases, ϕ, of the two superconductors,

$$I_{sc} = I_c \sin(\phi), \tag{2.20}$$

with I_c denoting the maximum or critical supercurrent. Similarly, the relation between the voltage V across the junction and the phase difference is given by

$$\frac{d\phi}{dt} = \frac{2e}{\hbar}V. \tag{2.21}$$

This relation implies oscillating supercurrents at a frequency determined by the bias voltage. Not only were the predictions by Josephson experimentally confirmed [33], it turned out that Eqs. 2.20 and 2.21 also hold for more general 'weak links' between superconductors (S). A weak link can be formed by constriction or a non-superconducting material (Fig. 2.16). *Proximity induced* supercurrents in non-superconducting materials have been observed experimentally in a number of material systems, like metals, 2-DEGs, semiconducting nanowires [34], and carbon nanotubes [35]. In Chapter 8 of this Thesis, we discuss experiments on the Josephson effect in S-graphene-S junctions.

2.7.2   Supercurrent in magnetic field

In the absence of a magnetic field the phase difference between the two superconductors, ϕ, is independent of y (Fig. 2.16). This changes when a perpendicular (in z-direction) magnetic field B is applied. In this case

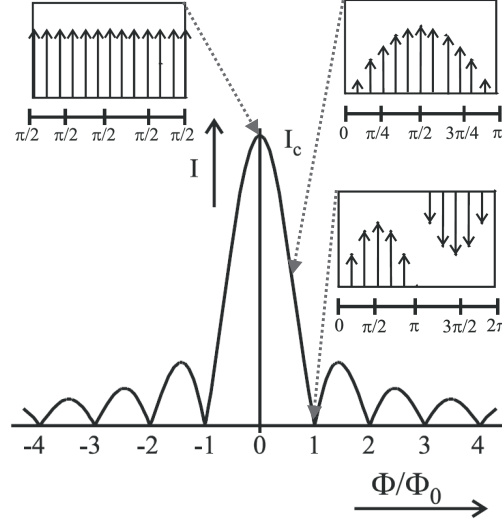$$\phi(y) = 2\pi BL'y/\Phi_0, \tag{2.22}$$

Figure 2.17: Fraunhofer pattern. The critical current $I_c(B)$ is plotted as a function of flux through the junction. The panels show the supercurrent density $J(y)$ along the width of the junction. The phase difference between the superconductors $\phi(y)$, which drives the supercurrent, is plotted underneath. At zero field ($\Phi/\Phi_0 = 0$) the supercurrent density is homogeneous. At $\Phi/\Phi_0 = 0.5$ the current density $J(y)$ is suppressed at the edges. At $\Phi = \Phi_0$ the supercurrent density is both positive and negative, and the critical current vanishes. Adapted from Ref. [36]

where $L' = L + \lambda$ with L the separation between the two superconductors and λ the London penetration depth, which is the length scale on which the field is screened. The position dependent phase, $\phi(y)$, results in a supercurrent density, $J_s = J_s(y)$, which also varies as a function of position (Fig. 2.17) and can be both positive and negative. The maximum supercurrent $I_c(B)$ can be calculated by integrating $J_s(y)$ over the width W of the junction (Fig. 2.17), giving

$$I_c(B) = I_c(0)\frac{\sin(\pi\Phi/\Phi_0)}{\pi\Phi/\Phi_0}, \tag{2.23}$$

where $\Phi = BL'W$. The result is a pseudo-periodic interference pattern known as a Fraunhofer pattern. When $\Phi = N\Phi_0$, the supercurrent vanishes because the supercurrents in positive and negative x direction cancel each other. The quasi-period of the oscillations can differ slightly from Φ_0 due to various reasons [37]. Deviations from the ideal Fraunhofer shape that is plotted in Fig. 2.17 indicate a non-uniform current distribution. For example, when the supercurrent is carried by edge-states only, the oscillations do not decay as a function of Φ because the device is effectively a superconducting quantum interference device (SQUID).

2.7.3   ac Josephson effect

When Eqs. [2.21] and [2.20] are solved for a bias voltage $V(t) = V_0 + V_{rf}\cos(\omega_{rf}t)$, which has both a dc and an ac component, one finds that dc supercurrents occur at finite dc voltages such that $V_n = \hbar\omega_{rf}/2e$. The ac voltage is usually applied in the form of rf-radiation, originating from an antenna somewhere near the device. At fixed rf-frequency, the current-voltage characteristic shows a number of steps that are known as Shapiro steps. The width of the steps is given by

$$\Delta I = 2I_c|J_n(2eV_{rf}/\hbar\omega_{rf})|, \tag{2.24}$$

where J_n denotes the n-th order Besselfunction.

2.7.4   Andreev reflection

In the previous paragraphs we have given a macroscopic picture of supercurrents through SNS junctions. Now we consider the microscopic mechanism behind Cooper pair transport into the N region: Andreev reflection. In the following discussion we consider the normal material to be graphene.

The process of Andreev reflection is schematically shown in Fig. 2.18. Due to the presence of a gap in the excitation spectrum of the superconductor, no electron states are available at energies $E < \Delta$. An electron with charge e, wavevector k_e, and energy $E < \Delta$ ($E_F \equiv 0$) arrives at the SN boundary. In the superconductor the wavefunction of the electron is exponentially damped on a length scale $\xi_s = \hbar v_F/(\pi\Delta)$ [38]. It was shown by Andreev in 1954 that charge transport across a clean SN interface occurs by pairing of the incoming electron with another electron with opposite spin and wavenumber to form a Cooper pair. Equivalently, one can say that the *electron* is Andreev reflected into a *hole* with equal wavenumber. Note that also the opposite Andreev reflection process can occur: a hole impinging on the $N - S$ interface will be reflected as an electron.

2.7.5   Properties of Andreev reflection

The properties of Andreev reflection in graphene depend on whether we are in the doped ($E_F \gg \Delta$) or undoped regime ($E_F = 0$).

Andreev Retro-reflection

In the heavily doped or metallic regime $E_F \gg \Delta$, the Andreev reflection process is similar to that in a normal metal. The energy difference between electron and
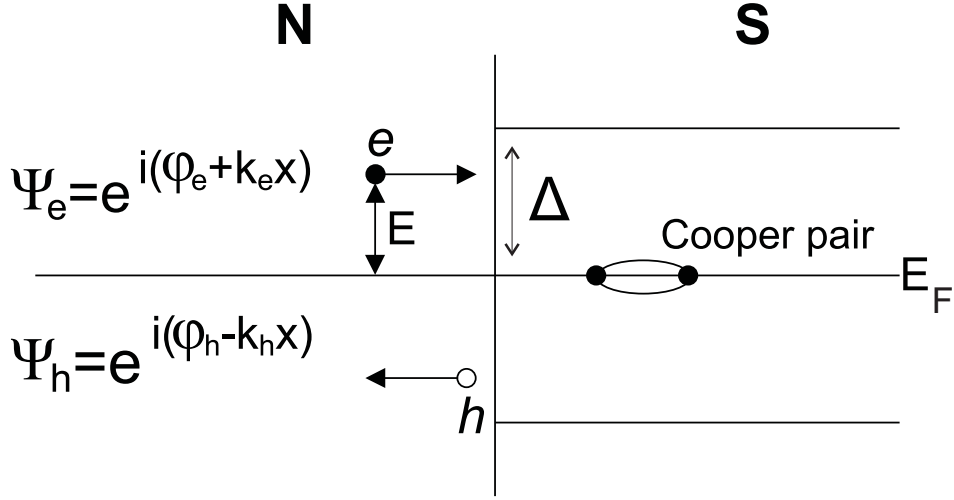
Figure 2.18: Schematic representation of Andreev reflection. An electron in the normal electrode (N, left) with energy E smaller than the superconducting gap Δ (filled circle) pairs with another electron with opposite energy and wave vector to form a Cooper pair in the Superconductor (S, right). The result is a hole (open circle) in N with opposite energy and equal wave vector reflected away from the interface. Adapted from Ref. [39]

hole is small, hence the electron and hole wavevectors are almost identical

$$
\begin{aligned}
k_e &= k_F + \frac{E}{\hbar v_F} \\
k_h &= k_F - \frac{E}{\hbar v_F} \quad .
\end{aligned}
\tag{2.25}
$$

The velocity of the incoming electron is opposite to the velocity of the outgoing hole, $\mathbf{v_e} = -\mathbf{v_h}$, because the velocity of a hole in the conduction band is opposite to its momentum. This is why the hole is called retro-reflected. Although both the electron and the retro-reflected hole are to first approximation massless, the small effective mass that results from higher order corrections is opposite in sign for electrons and holes. Note that the electron and its retro-reflected hole states have different valley index, in order to conserve chirality.

Specular Andreev reflection

In graphene we can have the special situation in which $|E_F| < \Delta$, see Fig. 2.19. Andreev reflection couples electron states from the conduction band with holes from the valence band of the other valley [40]. In this case k is exactly conserved. The 'mass' of a hole in the valence band is positive and hence the hole moves in

a

Superconductor

b

Superconductor

Andreev retro-reflection   Specular Andreev reflection
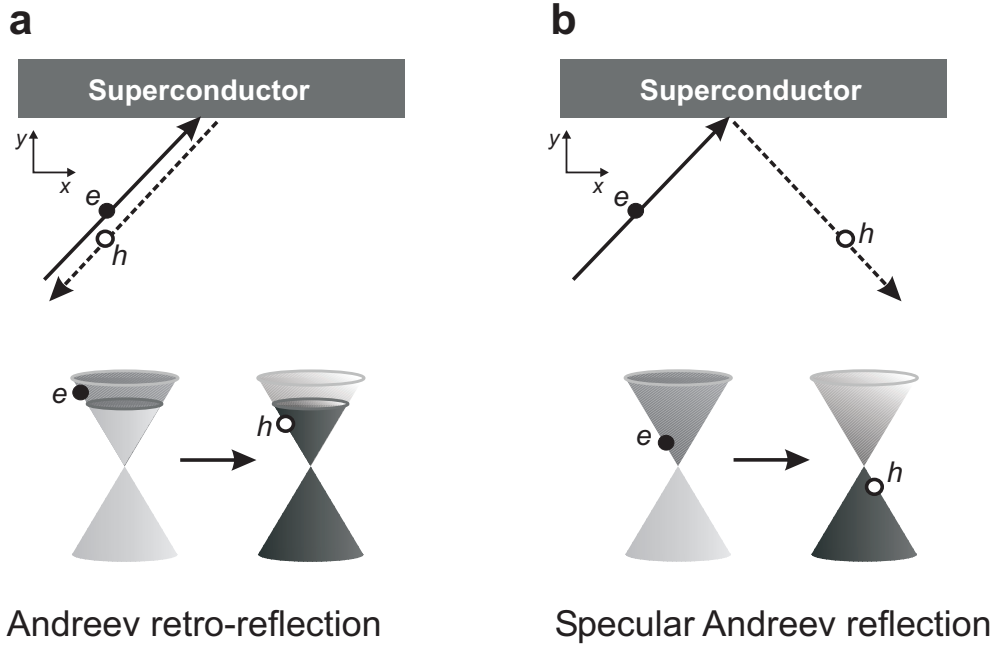
Figure 2.19: a, Andreev retro-reflection in the highly doped regime $E_F \ll \Delta$. An conduction band electron is reflected into a hole in the conduction band with approximately the same momentum. The velocity of a conduction band hole is opposite to its wave vector, hence the hole is retro-reflected. **b**, Specular Andreev reflection in the undoped regime. A conduction band electron is reflected into a valance band hole. A valance band hole moves in the same direction of its wave vector. Hence, v_x remains unchanged whereas v_y changes sign. Both Andreev reflection processes result in a hole in the opposite valley in order to conserve chirality.

the same direction as its wavenumber. Therefore the hole is not retro-reflected, but specular Andreev reflected instead.

Suppression of normal reflection

At normal incidence, backscattering at the NS interface with the conservation of charge ('normal' reflection) is suppressed [40]. This can be understood by considering Fig. 2.14b. The charge and energy conserving backscatter process requires the carrier to scatter to a different sublattice or, in other terms, to flip its pseudo-spin. Since the pseudo-spin states of electrons of opposite **k** are orthogonal, the scattering matrix element for this process vanishes. This means that electrons that approach the NS interface with energy below the superconducting gap are Andreev reflected with unity probability, because Andreev reflection conserves chirality.
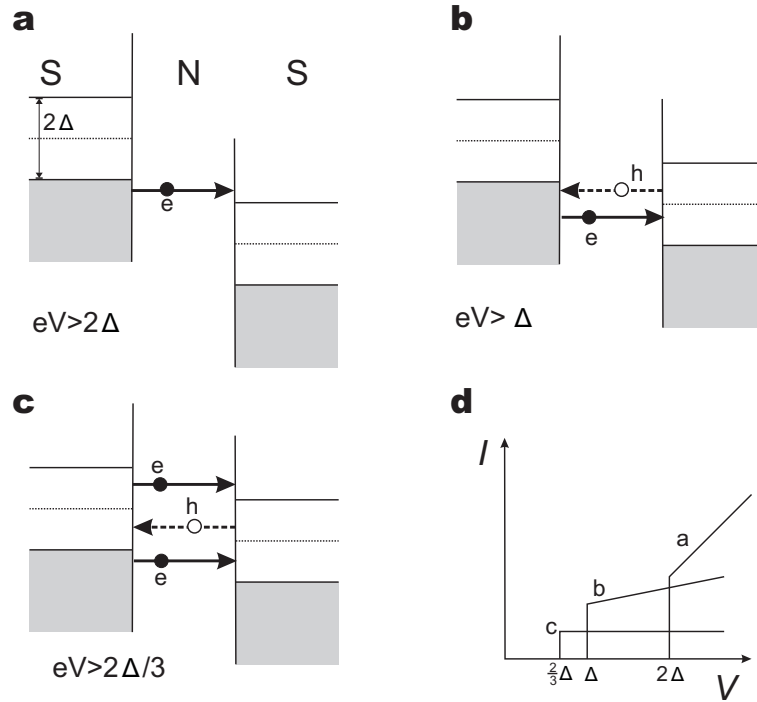
Figure 2.20: a-c, Schematic representation of multiple Andreev reflection processes at different bias voltages. In **d**, the contribution to the current of the processes in **a-c** is indicated.

2.7.6 Multiple Andreev reflections

In an SNS junction, Andreev reflections leave a signature in the dissipative branch of the current-voltage characteristics. Even in the absence of phase-coherence, which is required for the Josephson effect, multiple Andreev reflections (MAR) at the two NS interfaces result in a subgap structure for bias voltages smaller than $2\Delta/e$. MAR were first proposed as an explanation for subgap structures by Klapwijk, Blonder, and Tinkham [42]. Fig. 2.20 shows the qualitative picture. When $eV > 2\Delta$ as in Fig. 2.20a, an electron (quasi-particle) can be transferred directly from an occupied state below the gap in the left lead to an unoccupied state above the gap in the right lead. The contribution of the process to the current is indicated schematically in Fig. 2.20d. At $\Delta < eV < 2\Delta$, the electron has to be retro-reflected at least once, Fig. 2.20b, in order to contribute to the current. In this process, an electron coming from the left lead is converted into a Cooper pair at the right NS interface. The retro-reflected hole is absorbed by the empty hole states below the gap. At even lower bias, only higher order Andreev processes can give a contribution. In general, contributions of n-th order Andreev reflection processes result in an increase of the current at bias voltages exceeding

$2\Delta/n$.

2.7.7   Josephson effect in ballistic graphene

The Josephson effect in short ballistic graphene junctions was discussed recently by Titov and Beenakker [41]. They calculated the maximum supercurrent I_c by solving the Dirac-Bogoliubov-De-Gennes equation in a S-graphene-S junction. The product of normal state resistance and critical current $I_c R_N \simeq \Delta/e$ was found to be finite even at the Dirac point. Furthermore, they predict that I_c, like R_N, depends on the doping of graphene, which can be controlled with a gate electrode.

References

[1] Ronald Hanson, *Electron spins in Semiconductor Quantum Dots*, PhD thesis (2005).

[2] Kouwenhoven, L. P., Marcus, C. M., McEuen, P. L., Tarucha, S., Westervelt, R. M. & Wingreen, N.S. Electron transport in quantum dots, in *Mesoscopic Electron Transport*, edited by Sohn, L. L., Kouwenhoven, L. P. & Schön, G. (Kluwer, Series E **345**, 1997), 105-214.

[3] Averin, D. V. & Nazarov, Yu. V. in *Single Charge Tunneling - Coulomb Blockade Phenomena in Nanostructures*, edited by Grabert, H. & Devoret, M.H. (Plenum Press and NATO Scientific Affairs Division, New York, 1992), p. 217.

[4] Green, W. H. *et al. Electronic structures and geometries of C-60 anions via density functional calculations.* J. Phys. Chem. **100**, 14892 (1996).

[5] Park, J. *Electron transport in single molecule transistors*, dissertation thesis, Berkeley (2003)

[6] Park, H. *et al. Nanomechanical oscillations in a single-C60 transistor.* Nature **407**, 57 (2000).

[7] Friedman, J. R., Sarachik, M. P., Tejada, J. & Ziolo, R. *Macroscopic measurement of resonant magnetization tunneling in high-spin molecules.* Phys. Rev. Lett. **76**, 3830 (1996).

[8] Petukhov, K., Hill, S., Chakov, N. E., Abboud, K. A. & Christou, G. *Evidence for the S=9 excited state in Mn-12-bromoacetate measured by electron paramagnetic resonance.* Phys. Rev. B **70**, 054426 (2004).

[9] Van der Wiel, W. *Electron transport and coherence in semiconductor quantum dots and rings*, dissertation thesis, TuDelft (2002).

[10] Glazman, L. I. & Raikh, M. E. *Resonant Kondo transparency of a barrier with quasilocal impurity states*, JETP Lett. **47**, 452 (1988).

[11] Ng, T. K. & Lee, P. A. *On-site Coulomb repulsion and resonant tunneling*, Phys. Rev. Lett. **61**, 1768 (1988).

[12] Kawabata, A. J. Phys. Soc. Jpn. **60**, 3222 (1991).

[13] van der Wiel, W. G. *et al.*, *The kondo effect in the unitary limit*, Science **289**, 2105 (2000).

[14] N. van der Post, N. *et al.* , *Size-dependence study of the spin glass CuMn.*, Phys. Rev. B **53**, 15106 (1996)

[15] N. J. Craig *et al.* , *Tunable nonlocal spin control in a coupled-quantum dot system.*, Science **304**,565 (2004).

[16] Wallace, P. R. *The Band Theory of Graphite*, Phys. Rev. **71**, 622-634 (1947).

[17] Dresselhaus, M. S., Dresselhaus, G. & Eklund, P. C. *Science of Fullerenes and Carbon Nanotubes* (Academic Press, San Diego, 1996).

[18] White, C. T. & Mintmire, J. W. *Density of states reflects diameter in nanotubes.* Nature **394**, 29 (1998).

[19] Novoselov, K. S. et al. *Two-dimensional gas of massless Dirac fermions in graphene.* Nature **438**, 197 (2005).

[20] Zhang, Y. B., Tan, Y. W., Stormer, H. L. & Kim, P. *Experimental observation of the quantum Hall effect and Berry's phase in graphene.* Nature **438**, 201 (2005).

[21] Gusynin, V.P. & Sharapov, S.G., *Unconventional integer quantum Hall effect in graphene*, Phys. Rev. Lett. **95**, 146801 (2005).

[22] Castro Neto, A. H., Guinea, F., Peres, N. M. R., Phys. Rev. B, **73**, 205408 (2006).

[23] Shon, N.H. & Ando, T., *Quantum transport in two-dimensional graphite system*, J. Phys. Soc. Jpn. **67**, 2421 (1998).

[24] Nomura, K. & MacDonald, A. H., *Quantum transport fo massless Dirac fermions in graphene*, cond-mat/0606589 (2006).

[25] Aleiner, I.L. & Efitov, K.B., *Effect of disorder on transport in graphene*, cond-mat/0607200 (2006).

[26] Tworzydlo, J., Trauzettel, B., Titov M., Beenakker, C. W. J., *Sub-Poissonian Shot Noise in Graphene*, Phys. Rev. Lett. **96**, 246802 (2006).

[27] Morozov,S.V.,Novoselov,K.S., Katsnelson, M.I., Schedin, F.,Ponomarenko, L.A.,Jiang, D., Geim, A.K.,Strong suppression of weak (anti)localization in graphene, Phys. Rev. Lett. **97**, 016801 (2006).

[28] Morpurgo, A.F. & Guinea, F., *Intervalley scattering, long-range disorder, and effective time reversal symmetry breaking in graphene*, cond-mat/0603789 (2006).

[29] McCann, E., Kechedzhi, K., Fal'ko, V. I., Suzuura, H., Ando, T. & B.L. Altshuler, Weak localisation magnetoresistance and valley symmetry in graphene, cond-mat/0604015 (2006).

[30] Kamerlingh Onnes, H., Akad. van Wetenschappen (Amsterdam)**14**, 818 (1911).

[31] Bardeen, J., Cooper, L.N. & Schiefer, J.R., Phys. Rev. **108**, 1175 (1957).

[32] Josephson, B.D., Phys. Lett., **1**, 251 (1962).

[33] Anderson, P.W. & Rowell, Phys. Rev. Lett. **10**, 230 (1963).

[34] Doh, J., van Dam,J.A., Roest, A.L.,Bakkers, E.P.A.M., Kouwenhoven, L.P. & De Franceschi, S., *Tunable Supercurrent Through Semiconductor Nanowires*, Science **309** 272 (2005).

[35] Jarillo-Herrero, P., van Dam, J.A. & Kouwenhoven, L.P., *Quantum supercurrent transistors in carbon nanotubes*, Nature **439**, 953 (2006).

[36] Heida, J.P., *Josephson currents in two dimensional mesoscopic ballistic conductors*, PhD thesis (1998).

[37] Ledermann, U., Fauchere, A. L. & Blatter, G. *Nonlocality in mesoscopic Josephson junctions with strip geometry*, Phys. Rev. B **59**, R9027 (1999).

[38] See for instance M. Tinkham, *Introduction to Superconductivity*, McGraw-Hill, Singapore, (1996).

[39] Jochem Baselmans, *Controllable Josephson Junctions*, PhD thesis (2002).

[40] Beenakker, C.W.J., *Specular Andreev reflection in graphene*, Phys. Rev. Lett. **97**, 067007 (2006)

[41] Titov, M. & Beenakker, C.W.J., *Josephson effect in ballistic graphene*, Phys. Rev. B **74**, 041401(R), (2006)

[42] Klapwijk, T.M., Blonder, G.E. & Tinkham, M., *Explanation of subharmonic energy gap structure in superconducting contacts*, Physica B **109**, 1657(1982).

Chapter 3

Device fabrication & measurement techniques

This Chapter provides a brief description of the fabrication and measurement techniques used for the experimental work in this thesis. We first discuss the fabrication of graphene devices, including layer thickness characterization using Raman spectroscopy. Further, we summarize e-beam lithography fabrication methods and measurement setups. The fabrication and characterization of nanogaps for single molecule transport experiments are discussed in the next Chapter.

3.1 Graphene device fabrication

A method to fabricate graphene devices was developed by Novoselov *et al.* [1, 2]. We used natural graphite powder originating from North Korea (Fig. 3.1 a). A few grains of graphite are deposited on a 3x15 cm^2 piece of moderately sticky tape. Repeated folding and unfolding of the tape results in a homogenous distribution of graphite flakes on the tape (Fig. 3.1 b). Subsequently, a freshly cleaned substrate with a predefined marker pattern is pressed on the tape. In this way, graphite flakes of varying thicknesses are deposited on the substrate. Our substrates are degenerately doped p++ Si wafers with a dry thermal oxide layer.

Optical microscopy is used to identify few (including single) layer flakes. It is important that the SiO$_x$ thickness is close to 280 nm to maximize the color contrast between thin graphite flakes and bare substrate. The size of the thin flakes is typically a few square micrometer (although we are aiming at obtaining larger flakes). By taking a photograph of the optical microscope image, the position of the flake relative to a unique marker set is known for further processing.

Atomic force microscopy (AFM) can be used to further investigate the thickness and homogeneity of the flake (Fig. 3.1 d). However, it has turned out that
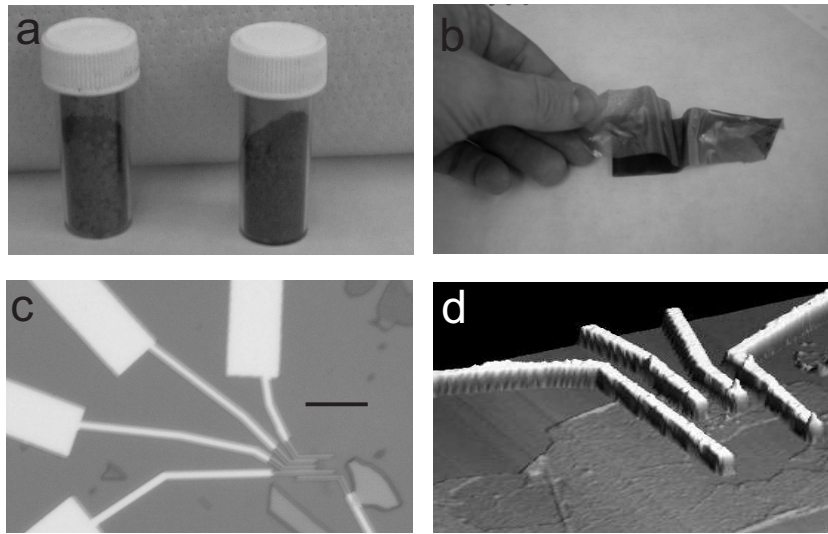
Figure 3.1: **a**, Small containers with natural graphite powder, **b**, Tape that is used to exfoliate graphite grains, **c**, Optical microscope image of thin graphite flake (barely visible) contacted by metallic electrodes. The thin, contacted flake is surrounded by thicker flakes. Scale bar corresponds to 4 μm. **d**, Atomic force microscope (AFM) image of a few layer graphene sheet contacted by metal electrodes. The width of the electrodes is 200nm. The thickness of the graphene sheet is inhomogeneous.

AFM does not provide conclusive information about the number of graphene layers. Although the thickness of a graphene layer is 0.34 nm, the measured height (using tapping mode AFM) of a single layer of graphene is about 1.5 nm. The discrepancy can be explained by the difference in interaction strength between tip and SiO_x and tip and graphene.

The optical photographs of thin graphite flakes are imported in a CAD program in which the electrode design is made. After standard electron beam lithography (see below), a bilayer of Ti (10 nm) and Al (50 nm) is evaporated followed by lift-off in acetone. The sample is now ready to be mounted in a chip carrier and wire-bonded (Fig. 3.1 c).

3.2   Raman spectroscopy on graphene

Although optical inspection provides a good indication of the layer thickness of a graphite sheet, it is not a conclusive method. Recently, Raman spectroscopy has been experimentally demonstrated to be a reliable method to identify the number of layers of graphite [3, 4], especially for thin layers. We tested this method on a thick (at least 6 layers) and a thin graphite flake using a laser with a wavelength of
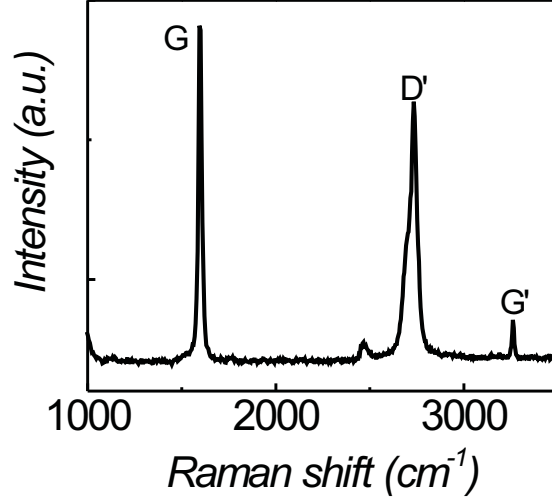
Figure 3.2: Raman spectrum of a relatively thick graphite sample, using a laser excitation of 532 nm. The most prominent peaks are the G, D' and G'.

532 nm (green). Using a lens with a numerical aperture of NA=0.75 we obtained a spot size of about 0.5 μm.

The raman spectrum of graphite is shown in Fig. 3.2. The dominant peak in this figure is the G line around 1594 cm^{-1}, which results from an in-plane optical mode (E_{2g} phonon), close to the Γ point. The D' peak around 2700 cm^{-1} is very pronounced even though the D peak cannot be resolved. The G' peak at 3260 cm^{-1} is just visible.

The layer thickness can be inferred from the details of the Raman spectrum. The G peak intensity decreases for thinner layers whereas the peak shifts to higher wave numbers at the same time, see Fig. 3.3a. To compare intensities of different samples, the intensity ratio $I_G^* = I_G/I_{D'}$ can be used since it scales linearly with the number of layers for few layer sheets. For the thin flake in Fig. 3.3a the relative intensity is $I_G^* = 0.46$, corresponding to ~ 3 layers according to the calibration in Ref [4]. For the thick flake $I_G^* = 0.67$ which means the number of layers is at least 6.

Another measure for the number of layers is the width of the D' peak, Fig. 3.3b. Based on model calculations, the integrated intensity remains the same whereas the single D' peak that corresponds to graphene is split into two peaks that overlap for graphite. Indeed the measurements in Fig. 3.3b show that the D' peak of the thick layer is much wider than the D' peak of the thin layer.
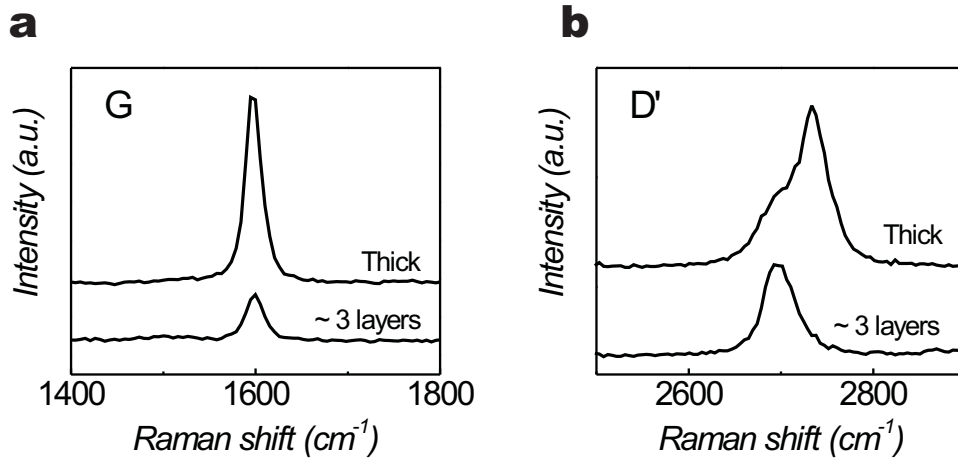
a

b

Figure 3.3: a, Comparison of the G peak of a thick and thin layer of graphite. For thinner layers the G peak intensity decreases and the maximum shifts slightly to higher wave numbers. **b**, The D' peak is broader for a thick layer compared to a thin layer.

These preliminary measurements demonstrate that raman spectroscopy is indeed a useful method to determine the layer thickness of a graphene sample. In combination with automated scanning of a substrate, it may replace optical microscopy as a method to identify single and double layer flakes that are suitable for device fabrication.

3.3   Electron beam lithography

We have used electron beam lithography (EBL) for defining the electrodes in a layer of resist. This process is illustrated schematically in Fig. 3.4 and consists of the following steps: (i) Spinning of resist, (ii) E-beam exposure, (iii) Metal deposition, (iv) Lift-off.

(i) For this Thesis we have used a double layer of polymethyl methacrylate (PMMA). The double layer improves the lift-off process due to a better resist profile with an undercut. This results from a higher sensitivity of the bottom layer compared to the top layer. The bottom layer (8% PMMA/MMA in ethyl-L-lactate for breakjunctions, PMMA 350K 3% in chlorobenzene for graphene devices) is spun for 55 seconds at 3000rpm and subsequently baked at 175°C for 15 minutes. The top layer (2% 950k PMMA in chlorobenzene) is spun at 6000 rpm for 55 seconds. We use a final bake at 175°C for 60 minutes.

(ii) The CAD design is written in the resist by an e-beam pattern generator (EBPG). Due to the exposure by an electron beam bonds in the polymer are
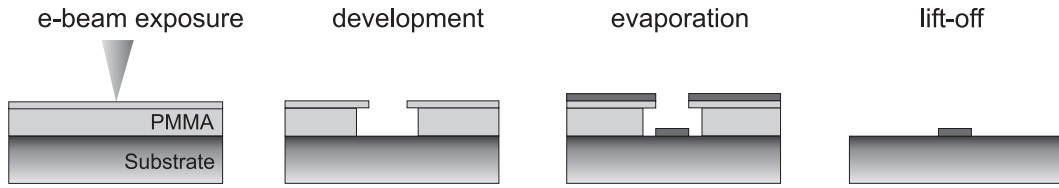
Figure 3.4: Schematic of the electrode fabrication process. In the first step a double-layer of e-beam resist (PMMA) is exposed using an e-beam pattern generator (EBPG). Then the exposed areas are dissolved with a suitable developer and a metal film is deposited using e-beam evaporation. In the last step the remaining resist is removed using a solvent (right panel).

broken and the resist becomes soluble in a developer. We have used methyl-isobutyl-ketone (MIBK):IPA 1:3 as a developer with a development time of 60 seconds. Subsequently, the sample has been rinsed for 60 seconds (120 seconds for graphene) in IPA.

(iii) Metal deposition is typically done by e-beam evaporation in a vacuum system with a background pressure of $3 \cdot 10^{-8}$ mBar using deposition rates of 0.1-0.5 nm/s.

(iv) The final step in the fabrication process is lift-off. In this step the remaining resist is dissolved by immersing the sample in hot acetone (50°C) for 15 minutes. Subsequently, the sample is rinsed in cold acetone and dried with a nitrogen flow.

3.4 Device packaging

The samples (with a typical size of 5×5 mm) are glued on a 32-pin chip-carrier using silver paint. The silver paint ensures a good electrical connection between the silicon substrate and the chip-carrier which is important if we use the substrate as a global gate. Electrical connections from the chip to the chip-carrier are made by ultrasonic bonding using Al/Si(1%) wires. Because the electrical contacts on the chip are separated from the substrate by a thin silicon oxide of 250 nm, the bonding has to be done carefully in order to prevent gate leakage. Therefore we use a flat bonding-tool and minimize the force during bonding (equivalent to ~18 gram).

3.5 Measurement techniques

Measurements have been performed at low temperatures in order to study the quantum mechanical phenomena of interest, like superconductivity and discrete energy spectra. The temperature ranges from 4.2 Kelvin down to 30 mK. For measurements between 1.5 and 4.2 Kelvin we have used a dip-stick which is immersed in a liquid helium dewar. By pumping on a 1-K pot the temperature can be reduced to 1.5 Kelvin. For other measurements we have used a dilution refrigerator in order to reach temperatures as low as 20 mK.

Although various different systems have been used throughout this thesis to cool down samples, the equipment for the electrical measurements has always been very similar. We have used battery-powered, in-house-built measurement equipment for all our electrical measurements in order to minimize the noise level. Voltage and current sources are computer-controlled and optically isolated from the electrical environment of the sample. Also the outputs of voltage amplifiers and IV-converters are optically isolated from the measurement computer.

In many experiments the filtering of noise is a crucial ingredient for a successful experiment. This is particularly important for measuring supercurrents because noise strongly suppresses the magnitude of the supercurrent. For these measurements we have used three stages of filtering: a π-filter, a copper-powder filter (CuF), and a two-stage RC filter (RCF). Together these filters cover the whole spectrum from low frequencies (kHz) up to the microwave regime.

References

[1] Novoselov, K. S. *et al.* , *Electric field effect in atomically thin carbon films.* Science **306**, 666-669 (2004).

[2] Novoselov, K. S. et al. *Two-dimensional gas of massless Dirac fermions in graphene.* Nature **438**, 197-200 (2005).

[3] Ferrari, A. C., *The Raman Fingerprint of Graphene*, cond-mat/0606284 (2006).

[4] Graf, D. *et al.* , *Spatially Resolved Raman Spectroscopy of Single- and Few-Layer Graphene*, cond-mat/0607562 (2006)

Chapter 4

Nanogap fabrication

4.1 Introduction

Control of the molecular conductance by a third electrode is not only a necessary requirement for integration of molecular devices [2] in circuits, but also essential for a thorough study of transmolecular conduction. To date, three-terminal molecular devices have been fabricated by several approaches mostly based on lithographic techniques. These include electromigration [3] in which a metal wire is broken with an electric field, shadow evaporation [4] and electrochemical techniques [5, 6, 7, 8]. In all these cases, nanoscale gaps are produced in metallic wires that are bridged by molecules, sitting on top of a gate electrode separated by an oxide layer. The gate electrode electrostatically modifies the potential of the molecular orbitals independently from the bias voltage. With the gate, the molecule can be oxidized or reduced and tuned between nonconducting and conducting states [9, 10, 11, 12, 13]. Electromigration is currently a widely adapted technique to fabricate molecular junctions and is reported to be a statistical method with poor control over the gap size [3]. We have extensively studied this electromigration method and found that some control can be obtained.

4.2 Wire fabrication

We will now outline our method in more detail starting with device fabrication. In short, it consists of four lithographic steps. In the first step, contact pads and wide wires are defined by evaporation of 3 nm Ti, 35 Au and 15 nm AuPd.

Parts of this chapter have been published as a Faraday Discussion in Ref. [1]
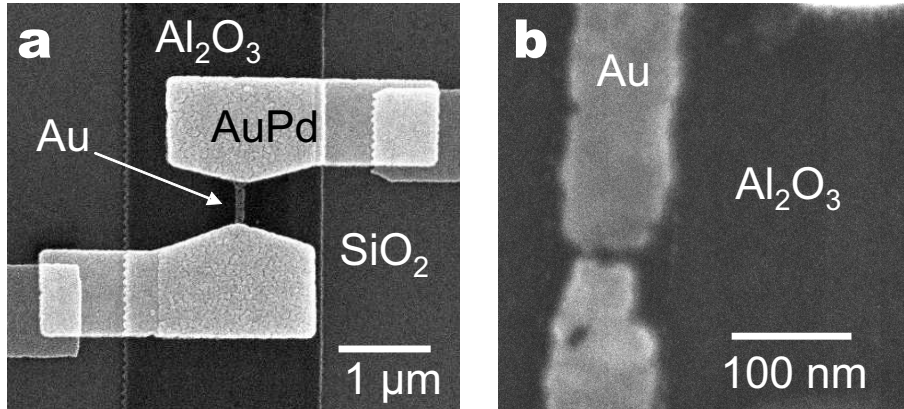
Figure 4.1: Scanning electron microscopy (SEM) pictures of a gold wire on top of an aluminium gate. **a**, Before electromigration. **b**, Zoom in after electromigration.

Secondly, the aluminum gate electrode is defined. The one-micron wide electrode is 50 nm thick with a sticking layer of 3 nm Ti. When taken out of the vacuum chamber of the evaporator, the aluminum oxidizes in air. The native oxide is typically 3 nm thick. The third step involves the definition of the thin and narrow gold wire that will be broken. A 10-12 nm thick and typically 100 nm wide gold wire without sticking layer is evaporated on top of the aluminum gate. In the last step, the thin wire is connected to the coarse pads by evaporation of 110 nm of AuPd.

4.3   Gap fabrication

The electrical circuit that is used to break the wire is shown in Fig. 4.2. It consists of a voltage source with a resistor in series, R_s. The current through the gold wire increases by ramping the voltage of the source; the current is determined by measuring the voltage across the series resistance. Electromigration-induced breaking [14] in gold is dominated by momentum transfer from charge carriers to the atoms, which is directed opposite to the electric field. The corresponding force is proportional to the current density and breaking occurs above a certain threshold value.

Experiments performed at 4.2 K demonstrate that the ratio between the series resistance and the resistance of the gold wiring on the chip plays a crucial role (see Fig. 4.3). Wires with a resistance of 80 Ω break completely when using $R_s = 1$ kΩ. With $R_s = 10$ Ω, they break only partially as illustrated Fig. 4.3 a. The wires first breaks to a plateau of 1 kΩ and only after increasing the voltage to 0.6 V, the wire breaks completely. To investigate the dependence of the zero-bias gap
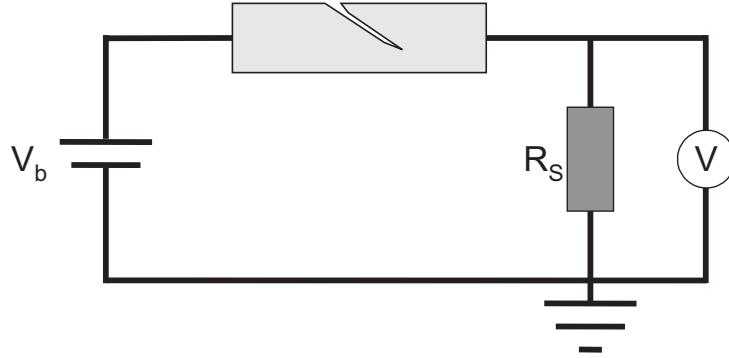
Figure 4.2: Electrical circuit used to break the thin metallic wires.

resistance on R_s, 26 Au wires on the same chip have been broken with different R_s. The resistance of the gold wires before breaking was approximately 50Ω. Six wires are broken with $R_s = 10$ Ω, six with $R_s = 50$ Ω, six with $R_s = 100$ Ω, four with $R_s = 300\Omega$ and four with $R_s = 500$ Ω. Immediately after breaking the wire, the voltage has been swept to zero. Figure 4.4 shows the break curves for the five different values of R_s. Higher values of R_s yield higher break voltages, while the current at which breaking occurs remains approximately constant as expected for electromigration. The zero-bias resistance of each broken wire is plotted in Fig. 4.4 b. A clear dependence is observed: the higher the series resistance in the electrical circuit, the larger the gap resistance. The difference in breaking can be understood as follows. The circuit with a high R_s compared to the bridge
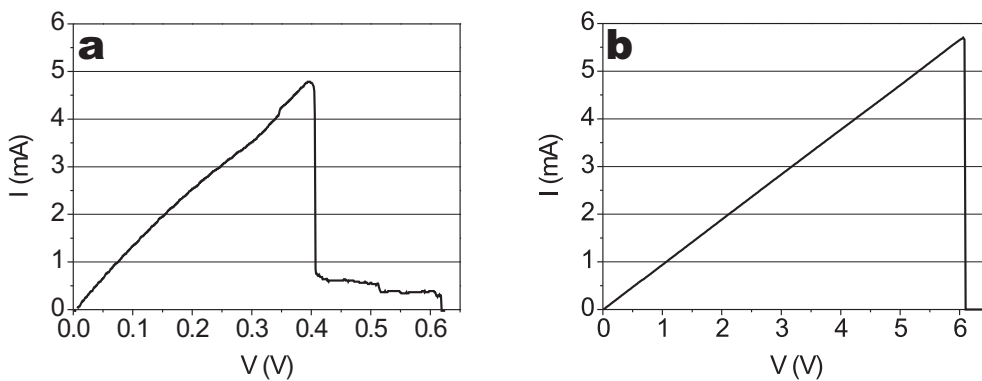
Figure 4.3: Break curves for two different series resistances. The current, determined by measuring the voltage across R_s, as a function of the voltage that is ramped linearly in time. **a**, Break curve for $R_s = 10$ Ω. The wire first breaks to a plateau of 1 kΩ before it breaks completely. **b**, Break curve for $R_s = 1$ kΩ. The wire breaks completely.

Figure 4.4: Twenty six Au wires broken with five different R_s. The higher the series resistance, the higher the zero-bias resistance of the gap. **a**, Representative break curves for different R_s, each represented with a different symbol. **b**, Zero-bias resistance of ea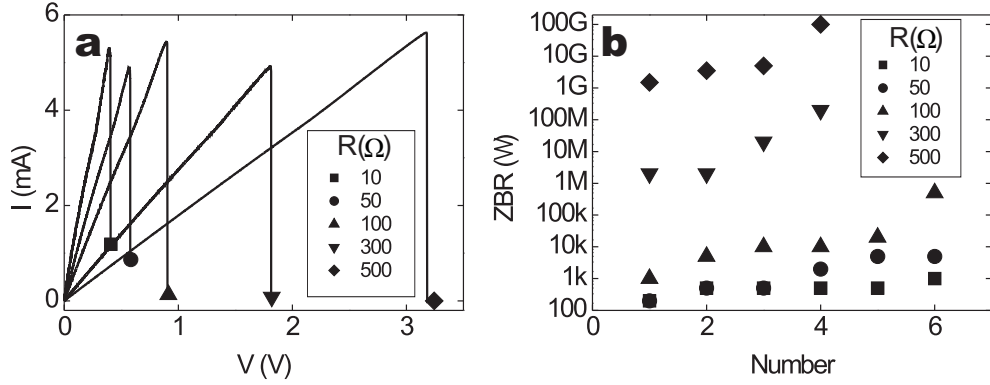ch wire. Different symbols correspond to different R_s (see legend). The values within one set are ordered from left (low) to right (high).

resistance is equivalent to that of a current source in which the current is kept constant. When increasing the bias voltage, the junction cross section decreases and the current density increases thereby accelerating the electromigration process. Before breaking most of the voltage drop is across R_s; during breaking this voltage is transferred to the junction. For low series resistances on the other hand, the voltage drop is mainly across the junction during the whole breaking process (connection to a voltage source) - this results in a less powerful breaking compared to the high-series-resistance case. A further improvement can be obtained by using an active feedback loop to monitor the resistance during breaking. While the electromigration process is inherently unpredictable, the catastrophic event that forms the void typically occurs in a time scale of $\sim 100\mu s$ - enough time to actively monitor the breaking process and adjust the voltage that is driving it. Different algorithms may be implemented to do this [15, 16]. We ramp the voltage until a decrease in the absolute conductance is observed upon which the applied voltage is returned to zero and the loop is repeated until a desired resistance has been reached. Compared with simply ramping the voltage to a fixed limit, the yield of devices made with controlled electromigration is greatly increased from about 50% to more than 90%.

4.4 Electromigration on the atomic scale

Remarkably, at low temperature (4.2 K) the electromigration process continues gradually even on the atomic scale as is demonstrated in Fig. 4.5. The panels
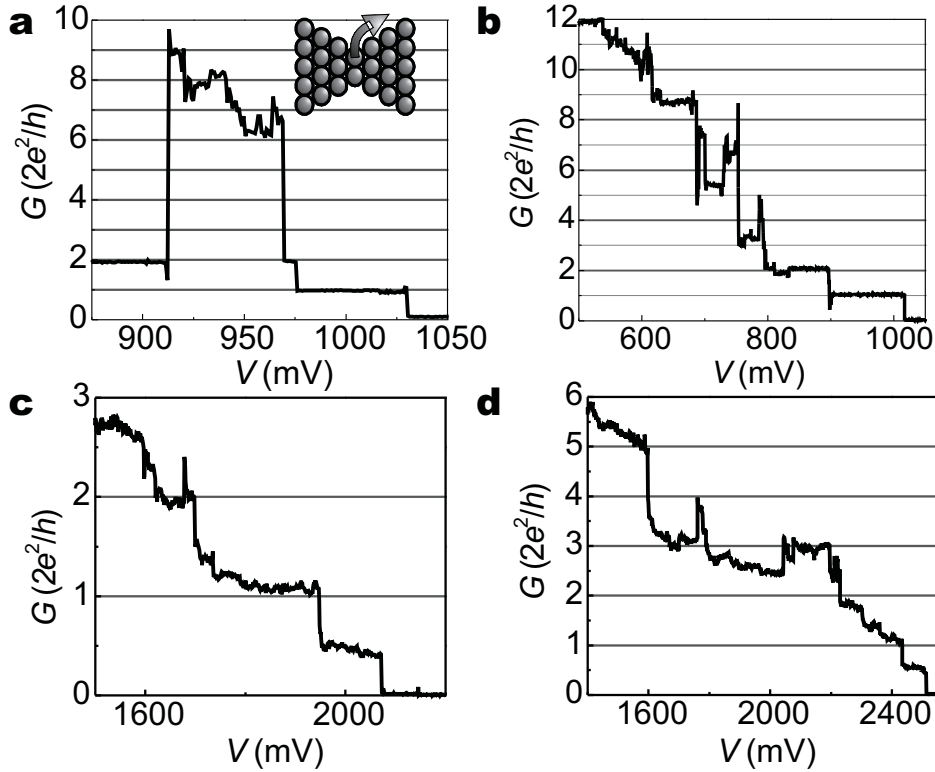
Figure 4.5: Atomic scale electromigration. At the final stage of the electromigration process an atomically thin wire is formed. Upon ramping the voltage across the wire, atomic rearrangements occur resulting in abrupt changes in G. **a**, **b**, In some devices, G is stable at $2e^2/h$, and $4e^2/h$ indicating that the wire is only connected by one or two atoms, respectively. **c**, **d**, Other devices did not show this behavior.

of this figure each show a zoom in on the final stage of a break with low R_s, similar to the one in Fig. 4.4 a. Upon slowly ramping the voltage (typically 1 V/min) the atomic configuration of the wire changes, resulting in sharp jumps in the conductance of the wire. Generally, the conductance decreases, which is consistent with a picture in which atoms are removed from the contact, but sometimes the conductance increases for a certain voltage range (see Fig. 4.5 a). The voltage at which the wire finally breaks, V_{break}, is very sample dependent and ranges between 0.8 V $< V_{break} <$ 3 V. In about 10-20% of the samples the conductance stabilizes at $2G_0$ and G_0 before breaking, see Fig. 4.5 a,b, where $G_0 = 2e^2/h$ denotes the quantum of conductance. In gold, a single atom point contact corresponds to one (spin degenerate) propagating mode and hence a conductance of G_0. This was experimentally demonstrated by the observation of

clear peaks at nG_0 (n is an integer) in the conductance histograms of mechanical break-junctions [17]. The height of these peaks as a function of bias voltage has been studied by Itakura *et al.* [18]. They found that for bias voltages exceeding ~ 1 V the height of the conductance peaks is strongly suppressed. This explains why we do not observe quantized conductance plateaus in samples that break at a higher bias voltage (~ 2 V), Fig. 4.5 c,d.

4.5 Current-voltage characteristics

To characterize the bare gold nanogaps, we have measured their current-voltage (IV) characteristics. A surprising result is that the IV's curves generally do not follow the dependence expected from direct, through-space tunneling with its characteristic $\sinh(V)$ form [21]. We have collected the IV's in seven different categories: i) IV's that do not show a current (< 1 pA for $V = 100$ mV) indicating that the gap distance is a few nanometer or larger, ii) IV's that are linear, iii) IV's that show a suppression (ZBS) of the current at low bias [19] (see Fig. 4.6 a), iv) smooth asymmetric IV's (see Fig. 4.6 b), v) IV's with steps (see Fig. 4.6 c), vi) IV's that are consistent with Coulomb blockade [20] (CB) (see Fig. 4.6 d,e), and vii) IV's with a zero-bias enhancement (ZBE) of the conductance around zero-bias. A gate effect is observed for the IV's with steps, with a zero-bias anomaly and IV's consistent with CB. An important consequence of the absence of direct tunneling behavior is that we cannot directly relate the gap resistance to a particular gap size.

The relative occurrence of the different IV-types is visualized in Fig. 4.7. A substantial number of IV's shows Coulomb blockade features. These not only include the IV's with Coulomb blockade and a gate effect (CB) but also the IV's with a gate-dependent zero-bias enhancement (ZBE) of the conductance indicative of a Kondo effect in an island with an odd number of electrons [10, 11, 13] and the IV's with steps that are reminiscent of transport through an island with asymmetric barriers (Steps). From Fig. 4.7, one can conclude that in at least one third of the cases, Coulomb blockade features are observed. Most likely, small islands in the form of gold grains are present in the gap region. A similar conclusion has been drawn by J. Consalez *et al.* [22] who detect fluorescence from small grains produced by electromigration and by Houck *et al.* [16] who report on the Kondo effect in bare gold electro-migrated junctions. The appearance of nanometer-sized gold grains near the gap is a problem if one wants to distinguish transport through molecules from that through grains: the energies to add or withdraw an electron may be of the same order in both cases. We have also

investigated the breaking process with wires that contain a self-assembled layer of OPV-3 molecules ((E,E)-1,4-Bis[4-(acetylthio)styryl]benzene; see Fig. 4.7). Prior to breaking, the wires are dipped in a 1 mM solution of OPV-3 in chloroform. Upon binding to gold, the acetate group falls off and the sulfur atom ensures a good bonding. After 12 hours, the sample with typically 24 individual wires is rinsed with chloroform and blow-dried. Then it is transferred to the measuring set-up and cooled to 4.2 K, where the wires are broken. As a control measurement, we have measured nanogaps that were only dipped in the solvent for 12 hours.

Figure 4.7 summarizes the result. Samples are all from the same fabrication run; measurements on other batches -not included- show similar behavior. In all three types of junctions, in about one third of the cases no current is detected (< 1 pA for $V = 100$ mV). In about one third of the cases, Coulomb blockade features (Steps, ZBE and CB) are seen. Surprisingly, samples that have been exposed to chloroform show more IV's with a ZBE, but less IV's with pure CB features. Another significant difference is that the samples with OPV-3 show more asymmetric IV's. These IV's show no gate effect and their origin is unclear at the moment. From the comparison, we conclude that the breaking process itself and the measurement of current-voltage characteristics at low temperature do not provide statistical evidence for the presence of molecules in the gap.

4.6   Molecular junctions

As the current-voltage characteristics themselves do not provide clear signs for the presence of molecules inside the gap, the electromigration method raises questions about which samples can be disregarded and which not. This is a tricky point because comparing two batches, one with molecules and one without, may not be conclusive since the molecules may influence the electro-migration process. Additional information is needed and in this respect a gate electrode seems to be of crucial importance. The key question is what characteristic features can be used to distinguish molecular transport from transport through gold grains. It is important to note that at low temperatures up to now three-terminal measurements on molecular junctions have all shown Coulomb blockade features [3, 10, 11, 12, 13] including the Kondo effect [10, 11, 13]. Our measurements presented in the previous section, however, show that Coulomb blockade itself is not a distinctive feature.

The above discussion has motivated us to study electron transport through molecules that have a distinct feature which can serve as a fingerprint for the molecule. In Chapter 6 we discuss an experiment on Manganese-12 (Mn12)
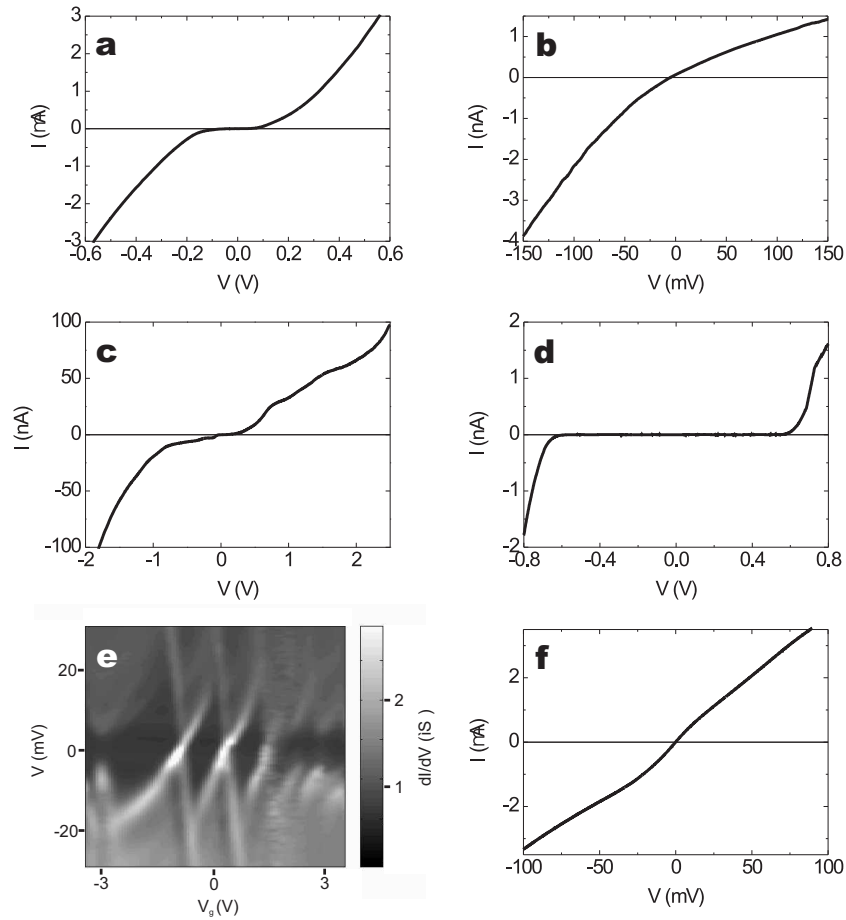
Figure 4.6: Different types of current-voltage characteristics of bare gold nanogaps measured at 4.2 K: **a**, *IV*'s with a zero-bias suppression (ZBS) of the current, **b**, asymmetric, smooth *IV*'s, **c**, *IV*'s with steps, **d**, *IV*'s consistent with Coulomb blockade and **f**, with a zero-bias enhancement of the conductance. In **e**, a stability diagram of a sample with Coulomb blockade is shown. Plotted is dI/dV as function of gate and bias voltage. In the black regions, the current is blocked (Coulomb diamond). Each black diamond-like structure corresponds to a different charge state.

derivatives in which reproducible features, related to the high spin ground state of the molecule, were observed. Note also, that for the Mn12 experiments we used a relatively high R_s. As a result, the gaps that formed were larger and the statistics discussed here do no longer apply. Instead, we found in control experiments that none of the wires without molecules had a finite resistance after breaking (more details in Chapter 6).

	Total	NC	Linear	ZBS	Asymm.	Steps	CB	ZBE
Bare gold	52	18	13	5	0	4	12	5
Chloroform	47	20	12	7	1	3	4	12
OPV-3	74	34	14	4	10	6	6	14

Figure 4.7: Distribution of the different types of current-voltage characteristics measured on three different types of samples from the same fabrication run: bare gold wires, wires that have been exposed to the solvent for 12 hours and wires that are exposed to the solvent with the OPV-3 molecules. NC stands for "no current", ZBS stands for "zero-bias suppression", Asymm. for "asymmetric IV", CB for "Coulomb blockade", and ZBE for "zero-bias enhancement". The table lists the number of junctions corresponding to each of the cases.
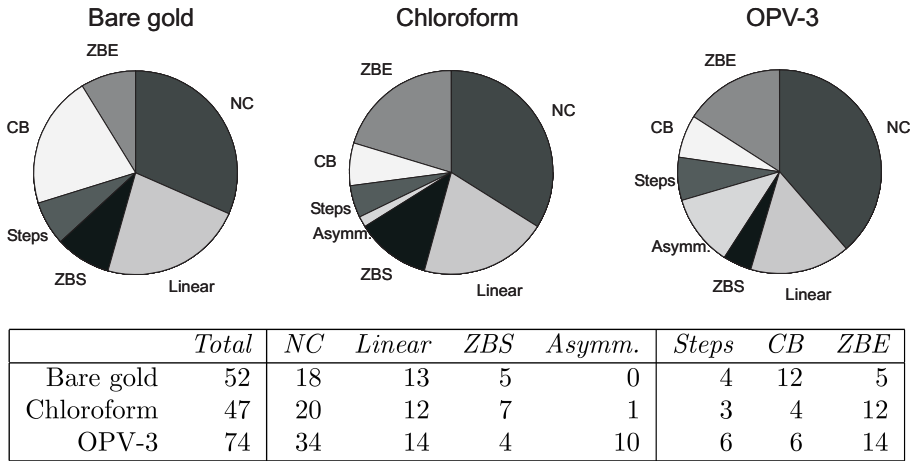
4.7   Gate coupling

The extent to which the orbital levels can be shifted up and down is controlled by the gate coupling parameter. This parameter is related to the gain of the device and in Coulomb theory it equals the ratio of the gate capacitance to the total capacitance of the islands. In an experiment, it should be as large as possible in order to access different charge states. The geometry plays an important role in the gate coupling and one should take care that the electrodes themselves do not screen the gate potential. For example, when using electro-deposition to create nanogaps, three-dimensional growth usually occurs and structures may be created that are effective screens (see Fig. 4.8). The molecule-electrode distance and the break-through voltage of the gate oxide are other important parameters. Currently, two gate materials are frequently used: heavily doped silicon substrates with thermally grown SiO_x on top and aluminum strips with a native oxide of only a few nanometers. In Fig. 4.8 b, we plot the gate-coupling factor calculated from Laplace's equation for a 1.24 and 2 nm wide junction as a function of the gate oxide thickness. For large thicknesses the dependence is $\sim 1/t_{ox}$. For the aluminum gates with $\epsilon_r = 9$, the gate coupling is about 0.1 so that with a typical break voltage of 4 V at low temperatures, the potential of the molecular levels can be shifted by 0.4 eV. For a silicon device ($\epsilon_r = 3$) with an oxide thickness

a

Source   Drain

Gate

b
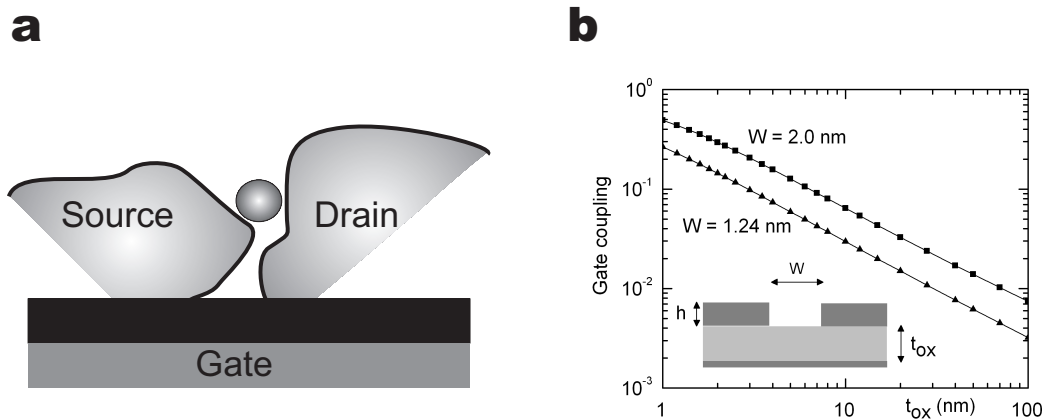
Figure 4.8: 1 **a**, For the nano-object trapped in between two metallic electrodes, fabricated for example by three-dimensional electro-deposition growth, the two leads can be effective screens against the gate. **b**, Gate coupling as a function of oxide thickness for two different gap sizes W. Calculation performed by solving Laplace's equation for the geometry shown in the inset with $\epsilon_r = 9$ and $h = 0.6$ nm.

of 250 nm, extrapolation yields a gate coupling of about 10^{-3}. With a typical breakthrough voltage of 100 V, the range over which the potential on the molecule can be varied equals 0.1 eV. Here, we have not corrected for the different relative permeability of the two oxides. Calculations show that this is a small effect.

References

[1] H.S.J. van der Zant *et al.* , Faraday Discuss., 2006, **131**, 347

[2] C. Joachim, J. K. Gimzewski, and A. Aviram, Nature, 2000, **408**, 541.

[3] H. Park, A. K. L. Lim, A. P. Alivisatos, J. Park, and P. L. McEuen, Appl. Phys. Lett., 1999, **75**, 301.

[4] K. Liu, Ph. Avouris, J. Bucchignano, R.Martel and S. Sun, Appl. Phys. Lett., 2002, **80**, 865; M.S.M. Saifullah, T. Ondaruhu, D.K. Koltsov, C. Joachim and M.E. Welland, Nanotechnology, 2002, **13**, 659.

[5] C. Z. Li, and N. J. Tao, Appl. Phys. Lett., 1998, **72**, 894.

[6] A. F. Morpurgo, C. M. Marcus, and D. B. Robinson, Appl. Phys. Lett., 1999, **74**, 2084.

[7] Y.V. Kervennic, H.S.J. van der Zant, A.F. Morpurgo, L. Gurevich and L.P. Kouwenhoven, Appl. Phys. Lett., 2002, **80**, 321.

[8] Y.V. Kervennic, D. Vanmakelbergh, L.P. Kouwenhoven and H.S.J. van der Zant, Appl. Phys. Lett., 2003, **83**, 3782.

[9] H. Park, J. Park, A.K.L. Lim, E.H. Anderson, A.P. Allivisatos and P.L. McEuen, Nature, 2000, **407**, 57.

[10] J. Park, A. N. Pasupathy, J. I. Goldsmith, C. Chang, Y. Yaish, J. R. Petta, M. Rinkoski, J. P. Sethna, H. D. Abruna, P. L. McEuen, and D. C. Ralph, Nature, 2002, **417**, 722.

[11] W. Liang, M.P. Shores, M. Bockrath, J.R. Long and H. Park, Nature, 2002, **417**, 725.

[12] S. Kubatkin, A. Danilov, M. Hjort, J. Cornil, J.-L.A.L. Bredas, N. Stuhr-Hansen, P. Hedegård and T. Bjørnholm, Nature, 2003, **425**, 698.

[13] L.H. Yu and D. Natelson, Nanoletters, 2004, **4**, 79.

[14] P.S. Ho and T. Kwok, Rep. Prog. Phys., 1989, **52** 301; M. Mahadevan and R.M. Bradley, Phys. Rev. B., 1999, **59**, 11037.

[15] D.R. Strachan, D.E. Smith, D.E. Johnston, T.-H. Park, M.J. Therien, D.A. Bonneel and A.T. Johnson, Appl. Phys. Lett., 2005, **86**, 043109.

[16] A.A. Houck, J. Labaziewicz, E.K. Chan, J.A. Folk and I.L. Chang, Kondo effect in electromigrated break junctions, Cond-mat, 2004, 0410752.

[17] For a review on atomic-sized conductors see: N. Agraït, A.L. Yegati, and J.M. van Ruitenbeek, Quantum properties of atomic-sized conductors, Phys. Reps., 2003, **377**, 81

[18] K. Itakura, K. Yuki, S. Kurokawa, H. Yasuda, and A. Sakai, Phys. Rev. B, 1999, **60**, 11163

[19] The *IV*'s with a linear behavior at high current/voltage are consistent with Environmental Coulomb Blockade (see e.g. K. Flensberg *et al.* , Phys. Scr., 1992, T42, 189) but more measurements (temperature dependence) are needed to draw definite conclusions.

[20] See e.g. L.P. Kouwenhoven, D.G. Austing, and S. Tarucha, Reports on Progress in Physics 2001, **64**, 701.

[21] J.G. Simmons, J. Appl. Phys., 1963, **34**, 1793.

[22] J.Gonzales, T.-H. Lee, M.D. Barnes, Y. Antoku and R.M. Dickson, Phys. Rev. Lett., 2004, **93**, 147402.

Chapter 5

In situ imaging of electromigration-induced nanogap formation

Hubert B. Heersche, Günther Lientschnig, Kevin O'Neill, Herre S. J. van der Zant, Henny W. Zandbergen

Nanometer-spaced electrodes are needed to contact single molecules and nanocrystals electrically. Electromigration - current-induced material transport - of thin gold wires has been used to fabricate ultra-small gaps [1] in which single molecules were trapped succesfully [2, 3, 4, 5]. Here, we imaged *in situ* the electromigration-induced nanogap formation by transmission electron microscopy (TEM) providing insight into the underlying mechanism. Real-time video recordings show that edge-voids form near the cathode side and narrow the polycrystalline gold wires down until a single-grain boundary intersects the constriction along which the breaking continues. During the last 50 ms of the break, a relatively large deformation of the constriction's geometry occurs. We suggest that the high electric field across the gap at the moment of failure induces this rapid deformation [6]. The shape of the anode (blunt) and the cathode (sharp) is asymmetric when the wire breaks with a bias voltage applied, but symmetric when a narrow constriction breaks spontaneously.

5.1   Introduction

A number of techniques have been developed for nanogap fabrication. Electromigration of a metallic wire [1] is a promising method because a large number of small (~1 nm) gaps can be produced with high yield. Furthermore, the electromigration technique is compatible with a back-gate electrode so that the electrostatic potential in the gap can be tuned independently of the applied bias. Several studies have worked on feedback mechanisms, based on resistance monitoring, to control the electromigration process thereby creating smaller gaps [7, 8, 9]. However, the characterization of the gaps obtained by electromigration is problematic. The resolution of both scanning electron microscopy and scanning tip microscopy (due to the shape of the electrodes and the tip) are generally too low to assess their size and shape. Resistance measurements can give an indication of the separation between the electrodes [10] but do not provide a reliable method of characterizing nanogaps. Recently, the resulting gap after electromigration has been imaged *ex situ* using TEM by Strachan *et al.* [11]. They find clean (debris free) ~ 5 nm nanogaps that relax to about 20 nm over time (months).

5.2   *In situ* transmission electron microscopy

The next step is to study the dynamics of the nanogap formation. For this purpose, we imaged the electromigration process *in situ* with TEM. We started by fabricating thin (12 nm) gold wires with small constrictions on top of transparent Si_3N_4 membranes. To contact the wires electrically while monitoring them by TEM, the junctions were mounted in a home-built TEM holder with wire feedthrough. Si_3N_4 membranes were obtained commercially. They consist of 30×30 μm^2 Si_3N_4 (20 nm thick) windows etched out of Si/Si_3N_4 wafers (Fig. 5.1a). Thin gold wires were first evaporated on top of the membrane without using an adhesion layer. In a second fabrication step, the thin wires were contacted by 100 nm thick leads and bonding pads. The total device resistance was 600-800 Ω. A small piece of wafer containing a membrane window and the patterned wiring was then glued onto a small printed circuit board (PCB) and wire-bonded. The sensitivity of the devices to electronic discharging complicated the experiments. The design of the TEM holder was such that primary electrons do not hit the PCB or glue preventing contamination. A Philips CM300UT-FEG electron microscope was used and video data were recorded with 20 images per second. The resulting recordings are available on-line [12]. Wires were electromigrated using either a passive breaking scheme (1 device) or an active breaking scheme with resistance feedback (3 devices). In the passive scheme, a voltage is ramped over
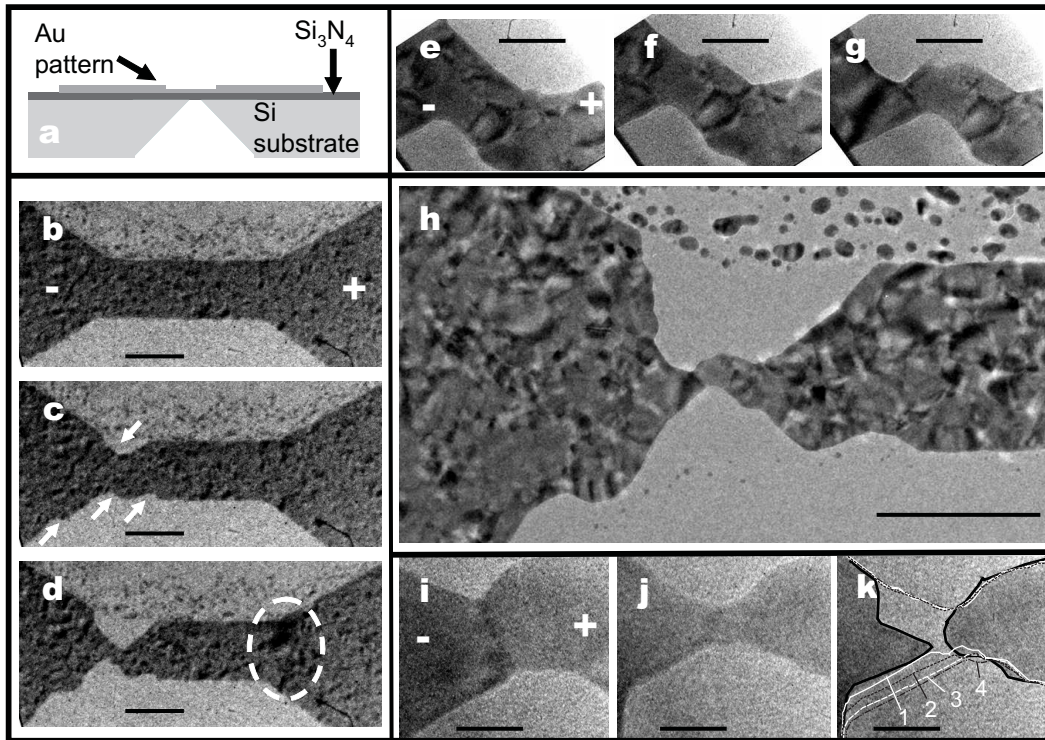
Figure 5.1: a, Sample schematic (cross section). **b-l**, Passive breaking of a 12 nm thick Au wire by ramping a bias voltage. **b**, Initial (polycrystalline) device before breaking. **c**, Voids form at the cathode side of the wire (arrows). **d**, Hillocks can be observed at the anode side (circle) **e-g**, The wire narrows down further until a single grain boundary spans the width of the constriction. **h**, High resolution overview image. **i-k**, The thick black line in **k** indicates the shape of the gap. The lines number 1-4 in **k** correspond to the shape of the wire in **j** and three images frames 100, 200 and 300 milliseconds earlier, respectively. The wire finally breaks along the grain boundary with a final gap size of 6 nm. Scale bars correspond to: 200 nm (**b-d, h**), 40 nm (**e-g**), 20 nm (**i-k**). Arrows indicate grain boundaries.

the junction while the current is monitored until the junction breaks (typically the electromigration process starts at a few mA). To slow down the breaking process [7, 8, 9], we also developed an active scheme in which a computer program ramps the voltage until either the resistance rises above a threshold or a maximum voltage is reached, whereupon the voltage is returned to zero and the ramp is started over. The cycle time is 25-50 ms. Upon electrically stressing the wire with 1-2 mA, a reversible resistance increase of about 10 percent was observed which can be attributed to heating. The resistance did not increase significantly further until the wires broke abruptly and the resistance became infinite. Remarkably, the same currents were needed irrespective of the stage of

the gap formation. This means that the current densities increased from initially 10^8 Acm^{-2} to current densities of about an order of magnitude larger in the final stage of the breaking process.

5.3   Passive breaking

We first discuss the breaking of a polycrystalline gold wire (Fig. 5.1b) using the passive breaking scheme. The bridge is initially 200 nm wide and 600 nm long with a distribution of grain sizes up to about 50 nm. We interrupted the breaking twice, by ramping the bias voltage quickly to zero, in order to zoom in on the region of interest. Fig. 5.1b,d correspond to the first ramp. Four voids appear at different locations near the cathode (indicated by arrows in Fig. 5.1c), strikingly not only at the narrowest part of the wire. The voids grow larger in time and they remain approximately at the same position in the wire. Note that the edges of the voids are almost parallel to the original edge of the cathode. In Fig. 5.1d a dark area can be observed near the anode (dotted circle), indicating the deposition of material forming a hillock.

After changing to a higher magnification the electromigration process was continued, see Fig. 5.1e-g. The constriction, resulting from two voids at opposite sides of the wire, narrows down further due to material that is gradually removed mostly along one edge of the constriction. At the same time, grain boundaries rearrange as the shape of the constriction changes. In Fig. 5.1g, a single grain boundary spans the width of the constriction. Fig. 5.1h shows an image of the constriction formed after the second interruption of the breaking process. A zoom in on the grain boundary that separates the constriction is shown in Fig. 5.1i. Failure occurs when the wire is about 15 nm wide on a timescale shorter than our sampling time (50 ms, Fig. 5.1j and k are consecutive frames). The resulting gap is about 5 nm and the electrode shape is asymmetric: the cathode side of the gap has a relatively sharp, point-like shape whereas the anode side is more rounded. The constriction geometry at 50, 150, 250, and 350 ms before breaking are shown in Fig. 5.1k by the lines 1-4, respectively. This shows that layers in front of the grain boundary are 'pealed off'; the video recordings [12] show that this pealing-off process starts at the grain boundary.

5.4   Active breaking

Figure 5.2 a-d, e-h, and i-l show the active breaking of three different samples in bright field, bright field, and dark field imaging modes, respectively. The width of
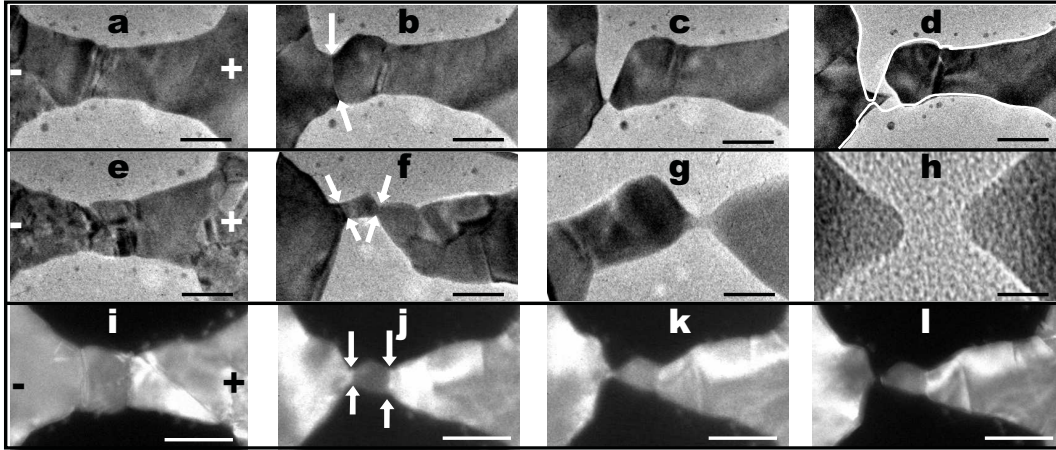
Figure 5.2: Active breaking of three devices (three rows, respectively). Frames show the wires before electromigration **a,e,i**, the initial stage of the electromigration in which grains fuse and voids start to form along grain boundaries **b,f,j,** the last frame before breaking occurs **c,k,** and the corresponding subsequent frame **d,l,** (sampling frequency 20 Hz). After frame **g**, the active breaking was stopped, but the device broke nevertheless, **h**. Frames **i-l** were taken in dark field mode. Scale bars corresponds to: 50 nm (**a-e, i-l**), 25 nm (**f**), 10 nm (**g**), 5 nm (**h**). Arrows indicate grain boundaries.

the lithographically defined constrictions is 50 nm and the length about 200 nm. Grain boundaries span the width of the constriction (transgranular or bamboo wires). In the active scheme, each break has been performed in a 30 s to 2 minutes time span. The void formation in Fig. 5.2a-d occurs along a single grain boundary (indicated by arrows in Fig. 5.2b) at the cathode side of the wire and proceeds as in the last stage of the breaking in Fig. 5.1. Just before the void formation starts, several grains fuse to become larger grains. The process is preceded by a movement of a grain boundary in the direction of electron flow. In Fig. 5.2 c, the constriction has become so small that a bridge of only a few nanometers connects the two electrodes. The consecutive frame (see Fig. 5.2d) shows the formation of a gap. A remarkably rapid deformation of the electrodes - of the order of 10^5 atoms have been transported in the last 50 ms compared to 10^2 atoms in the 50 ms before - has occurred during this final stage of the breaking. Comparing the constriction's shape just before (white line in Fig. 5.2d) and after breaking even suggests backflow of material towards the cathode. The cathode side of the electrode has again a point-like shape (radius ~ 1 nm) whereas the anode side is flat. The final gap is 6 nm.

The gap formation process in another device (Fig. 5.2e-h) is similar except for the final stage, in which we stopped the electromigration process by reducing

the bias voltage to zero. In the first stage, grains fuse and grain boundaries rearrange. Subsequently, the wire narrows down along two different grain boundaries (Fig. 5.2f). At this point, the breaking was interrupted and we zoomed in on the narrowest point of the constriction. The breaking was continued until the wire became as narrow as 2 nm. The active breaking was stopped once again, and the wire broke spontaneously within 15 s while no bias voltage was applied. The remaining gap is 5 nm. Note the symmetric shape of the contacts after the spontaneous break in contrast to the asymmetric shape that was observed in samples that broke with an applied bias. We imaged the breaking of another wire in dark field mode (Fig. 5.2i-l), in which the contrast depends strongly on the orientation of the grains. The breaking follows the same pattern as for the other two transgranular wires: voids grow along two grain boundaries and breaking occurs along a grain boundary when the wire has a width of 4 nm. After breaking the gap is 6 nm.

5.5   Discussion and conclusions

Electromigration is a widely studied phenomenon due to its relevance for microelectronics where it can result in failure of electrical interconnects. Mass flux is the result of a net force exerted on the ions when an electric field is present [13]. Divergences in the mass flux, for example due to temperature gradients, can result in the formation of voids (where material is depleted) and hillocks (where material is deposited). Two regimes are generally considered depending on the ratio between grain diameter D and wire width W. In the polycrystalline regime ($W \gg D$), as in the case of the sample in Fig. 5.1, mass transport is initially mediated mainly by surface and grain boundary diffusion. This is apparent in Fig. 5.1c where multiple voids have formed at different positions along the wire and in Fig. 5.1d where the associated hillock have formed. Since momentum transfer between electrons and gold ions (wind force) dominates the direct force of the electric field, which is in the opposite direction, voids are expected to form at the cathode side of the wires. In all 4 wires studied, this expectation is confirmed.

Our data show that grains fuse to form larger ones and grain boundaries rearrange in the initial stage of the breaking. In the final stage, all wires have become transgranular, i.e. one grain boundary intersects the whole wire width ($W = D$). The grain boundary that divides the wire now forms the bottleneck for electron transport and the wire starts narrowing down along it. Au atoms are stripped off at the grain boundary followed by a whole plane of Au atoms on the cathode

side. The final break occurs at, or very close to, the grain boundary. This in contrast to studies in Al lines where intragranular voids have been observed [14]. The large deformation (Figs. 5.1 k and 5.2 d) during the last 50 ms of the breaking is unexpected. It suggests that the electron wind force, which is the driving force for mass transport throughout the breaking process, no longer dominates at the very last moment of breaking. Mechanical stress can also be excluded as a driving force, since the deformations are very local. A possible explanation is that the direct force of the electric field, which becomes very high near the gap at the instant the wire breaks, results in a quick deformation of the electrodes [6] (Figs. 5.1 k and 5.2 d) and in a backflow of material (Fig. 5.2d). The effect of the electric field could also explain the difference in electrode shape which is asymmetric (blunt anode and sharp cathode, Figs. 5.1 k and 5.2 d) or symmetric (Fig. 5.2h) after breaking with and without voltage bias applied, respectively. An asymmetric shape was not observed by Zandbergen *et al.* [15] in gold wires that were broken with a high intensity electron beam.

Heating explains the reversible resistance increase that is observed when the wire is biased. However, the fact that the grain boundary along which the final breaking occurs remains visible until a gap has formed indicates that electromigration and not melting is the cause of the nanogap formation. The final gap size in these experiments is 5-6 nm, similar to previous findings[11]. The gap size of the sample that broke without bias is similar to the gap size obtained with samples that broke with an applied bias, heating does not determine the final electrode separation. Smaller gaps have been reported on different substrate materials (SiO_x, Al_2O_3) [1, 10] indicating a substrate dependence of the gap size that can be verified in future experiments. Detailed imaging of the breaking process of thin gold wires is an important step towards the controlled and reproducible fabrication of nanometer spaced electrodes.

References

[1] Park, H., Lim, A. K. L., Alivisatos, A. P., Park, J. & McEuen, P. L. *Fabrication of metallic electrodes with nanometer separation by electromigration.* Appl. Phys. Lett. **75**, 301-303 (1999).

[2] Park, H. *et al. Nanomechanical oscillations in a single-C-60 transistor.* Nature **407**, 57-60 (2000).

[3] Park, J. *et al. Coulomb blockade and the Kondo effect in single-atom transistors.* Nature **417**, 722-5 (2002).

[4] Liang, W. J., Shores, M. P., Bockrath, M., Long, J. R. & Park, H. *Kondo resonance in a single-molecule transistor.* Nature **417**, 725-729 (2002).

[5] Yu, L. H. *et al. Inelastic electron tunneling via molecular vibrations in single-molecule transistors.* Phys. Rev. Lett. **93**, 266802 (2004).

[6] Mayer, T. M., Houston, J. E., Franklin, G. E., Erchak, A. A. & Michalske, T. A. *Electric field induced surface modification of Au.*, J. Appl. Phys. **85**, 8170-8177 (1999).

[7] Esen, G. & Fuhrer, M. S. *Temperature control of electromigration to form gold nanogap junctions.* Appl. Phys. Lett. **87**, 263101 (2005).

[8] Strachan, D. R. *et al. , Controlled fabrication of nanogaps in ambient environment for molecular electronics.* Appl. Phys. Lett. **86**, 043109 (2005).

[9] Houck, A. A., Labaziewicz, J., Chan, E. K., Folk, J. A. & Chuang, I. L. *Kondo effect in electromigrated gold break junctions.* Nano Lett. **5**, 1685-1688 (2005).

[10] Lambert, M. F., Goffman, M. F., Bourgoin, J. P. & Hesto, P. *Fabrication and characterization of sub-3 nm gaps for single-cluster and single-molecule experiments.* Nanotechnology **14**, 772-777 (2003).

[11] Strachan, D. R. *et al. , Clean electromigrated nanogaps imaged by transmission electron microscopy.* Nano Lett. **6**, 441-444 (2006).

[12] For video recordings see: *http://med.tn.tudelft.nl/tem/.*

[13] Scorzoni, A., Neri, B., Caprile, C. & Fantini, F. *Electromigration in Thin-Film Interconnection Lines - Models, Methods and Results.* Mat. Sci. Rep. **7**, 143-220 (1991).

[14] Rose, J. H. *Fatal Electromigration Voids in Narrow Aluminum-Copper Interconnect.* Appl. Phys. Lett. **61**, 2170-2172 (1992).

[15] Zandbergen, H. W. *et al. Sculpting nanoelectrodes with a transmission electron beam for electrical and geometrical characterization of nanoparticles.* Nano Lett. **5**, 549-553 (2005).

Chapter 6

Electron transport through single Mn_{12} molecular magnets

H. B. Heersche, Z. de Groot, J. A. Folk, H. S. J. van der Zant, C. Romeike, M. R. Wegewijs, L. Zobbi, D. Barreca, E. Tondello, and A. Cornia

We report transport measurements through a single-molecule magnet, the Mn_{12} derivative $[Mn_{12}O_{12}(O_2C\text{-}C_6H_4\text{-}SAc)_{16}(H_2O)_4]$, in a single-molecule transistor geometry. Thiol groups connect the molecule to gold electrodes that are fabricated by electromigration. Striking observations are regions of complete current suppression and excitations of negative differential conductance on the energy scale of the anisotropy barrier of the molecule. Transport calculations, taking into account the high-spin ground state and magnetic excitations of the molecule, reveal a blocking mechanism of the current involving non-degenerate spin multiplets.

6.1   Introduction

During the last few years it has been demonstrated that metallic contacts can be attached to individual molecules allowing electron-transport measurements to probe their intrinsic properties. Coulomb blockade and the Kondo effect, typical signatures of a quantum dot, have been observed at low temperature in a single-molecule transistor geometry [1, 2, 3]. In the Coulomb blockade regime, vibrational modes of the molecule appear as distinct features in the current-voltage (I-V) characteristics [4, 5, 6]. Conformational, optical or magnetic properties of molecules may also affect electron transport. With respect to the latter, an interesting class of molecules is formed by the single-molecule magnets (SMMs). These molecules show magnetic hysteresis due to their large spin and high anisotropy barrier, which hampers magnetization reversal. The prototypal SMM, Mn_{12}-acetate, has total spin $S = 10$ and an anisotropy barrier of about 6 meV [7]. Spin excitations play an important role in the magnetization reversal process through quantum tunneling of the magnetization (QTM) [8]. Although the electronic and magnetic properties of SMMs have been studied intensively on bulk samples and thin films [9, 10, 11, 12, 14], the effect of the high-spin ground state on electron transport in isolated molecules remains an unexplored topic [13].

   In this Letter we discuss transport through individual SMMs that are weakly coupled to gold electrodes (see Fig. 6.1). Experimental data show low-energy excited states with a strong negative differential conductance (NDC) and regions of complete current suppression (CCS). We have modeled tunneling through a single Mn_{12} molecule taking into account its magnetic properties. Sequential tunnel processes can result in spin-blockade of the current, providing a possible explanation for the observed NDC and CCS. This effect is different from conventional spin blockade [15, 16] where there is no spin anisotropy.

6.2   Sample fabrication

We use the single-molecule magnets $[Mn_{12}O_{12}(O_2C\text{-}R\text{-}SAc)_{16}(H_2O)_4]$ (Mn_{12} in the rest of the text), where R=$\{C_6H_4, C_{15}H_{30}\}$. Both are tailor-made Mn_{12}-acetate derivatives. These molecules feature thiol groups in the outer ligand shell and consequently exhibit a strong affinity for gold surfaces [12, 17]. Beside ensuring robust tethering of the clusters to the surface, the ligands are also believed to serve as tunnel barriers, so that the molecule is only weakly coupled electronically to the gold. We assume that its magnetic properties are conserved in the vicinity of gold electrodes. The diameter of the molecule (core plus ligands) is about 3 nm for R=C_6H_4 and 5 nm for R= $C_{15}H_{30}$. In this paper we focus on the
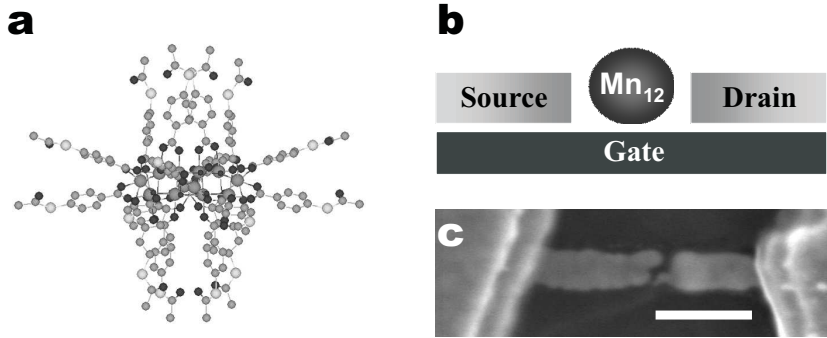
Figure 6.1: a, Side view of a Mn_{12} molecule with tailor made ligands containing acetyl-protected thiol end groups ($R=C_6H_4$). Atoms are color labelled: Manganese (gray, large), oxygen (dark gray), carbon (gray), sulfur (light gray). The diameter of the molecule is about 3 nm. **b**, Schematic drawing of the Mn_{12} molecule (circle) trapped between electrodes. A gate changes the electrostatic potential on the molecule enabling energy spectroscopy. **c**, Scanning electron microscopy image of the electrodes. The gap is not resolvable. Scale-bar corresponds to 200 nm.

transport features that are measured on the $R=C_6H_4$ derivative, which is depicted in Fig. 6.1a.

Electromigration [18] produced the nanometer-scale gaps in which the molecules were trapped. We fabricated thin (~ 10 nm) gold wires (width 100 nm, length 500 nm) on top of a Al/Al_2O_3 gate using e-beam lithography. The wires were contacted by thick (100 nm) gold leads. Samples were cleaned in acetone and iso-propanol, descumed with an oxygen plasma, then soaked in a 0.1 mM Mn_{12}-solution containing a catalytic amount of aqueous ammonia (to promote deprotection of the -SAc groups, see Ref. [17]) for at least 1 hour. After taking a sample out of the solution it was dried in a nitrogen flux and mounted in a 4He system with a 1 K pot. The bridges were electromigrated in vacuum at room temperature by ramping a voltage across them while monitoring the current using a series resistor of 10 Ω. The junctions broke at about 1 V.

6.3 Experimental results

After breaking, the samples were cooled down to 4 K and the junction conductances were measured as a function of gate voltage. Although about 10 % of 200 junctions showed Coulomb blockade related features, only four samples were stable enough for detailed measurements [19]. In Fig. 6.2a we plot the differential conductance G as a function of gate (V_g) and bias voltage (V_b) for one such a device ($T = 3$ K, $R=C_6H_4$). The lines separating the conducting regions from

the diamond-shaped Coulomb blockade regions have different slopes for the three different charge transport regions. Within orthodox Coulomb blockade theory this implies that the transport regions belong to different quantum dots, since the capacitance to the environment is assumed constant for each dot. However, for molecular quantum dots it is not possible to rule out that these three regions come from three different charge states of the same molecule. Kubatkin *et al.* found that the charge distribution - and therefore also the capacitance - of a (large) molecule depends on its charge state [3]. In either scenario, however, the current in the non-overlapping transport regions is determined by a single molecule.

Lines in transport regions running parallel to the diamond edges correspond to the onset of transport through excited states of the molecule. We have observed an excitation at 14 ± 1 meV in all 6 of the stable transport regions that were observed in the four samples. This excitation is indicated with arrows in Figs. 6.2c-f and Fig. 6.3a and appears to be a fingerprint of the molecule. Its origin can be vibrational since the Raman-spectrum exhibits strong peaks beyond this energy, which are associated with vibrations of the magnetic core of the molecule [20]. A fingerprint is needed since metal grains that are formed during electromigration can mimic the transport properties of single-molecules [21, 22, 23]. Moreover, we have studied the electromigration process extensively and found that the gap size can be tuned by the total (on- and off- chip) series resistance [24]. A relatively large series resistance (200 Ω) has been used to create a gap larger than ~ 1 nm. Using this technique, we did not measure any conductance up to 1 V in 50 control samples without molecules deposited.

6.3.1 Low energy excitations

The focus of this paper is on transport features at low-energy ($\lesssim 5$ meV): a region of complete current suppression (CCS) and a strong negative differential conductance (NDC) excitation line in the stability diagrams. Both are visible in Fig. 6.2a. At the left degeneracy point in this figure the current is fully suppressed at positive bias voltage above the left diamond edge (dashed line). Transport is restored beyond an excitation that lies at 5 meV. Remarkably, the right diamond edge *does* continue all the way down to zero bias, defining a narrow strip (~ 1 mV wide) where transport is possible. In the right conductive regime in Fig. 6.2a, two excitations at an energy of 2 meV and 3 meV are the most pronounced features. The 2 meV excitation is visible as a bright line with positive differential conductance (PDC); the 3 meV excitation as a black line (NDC). The strength of the NDC is clearly visible in the I-V_b plot in Fig. 6.2b.
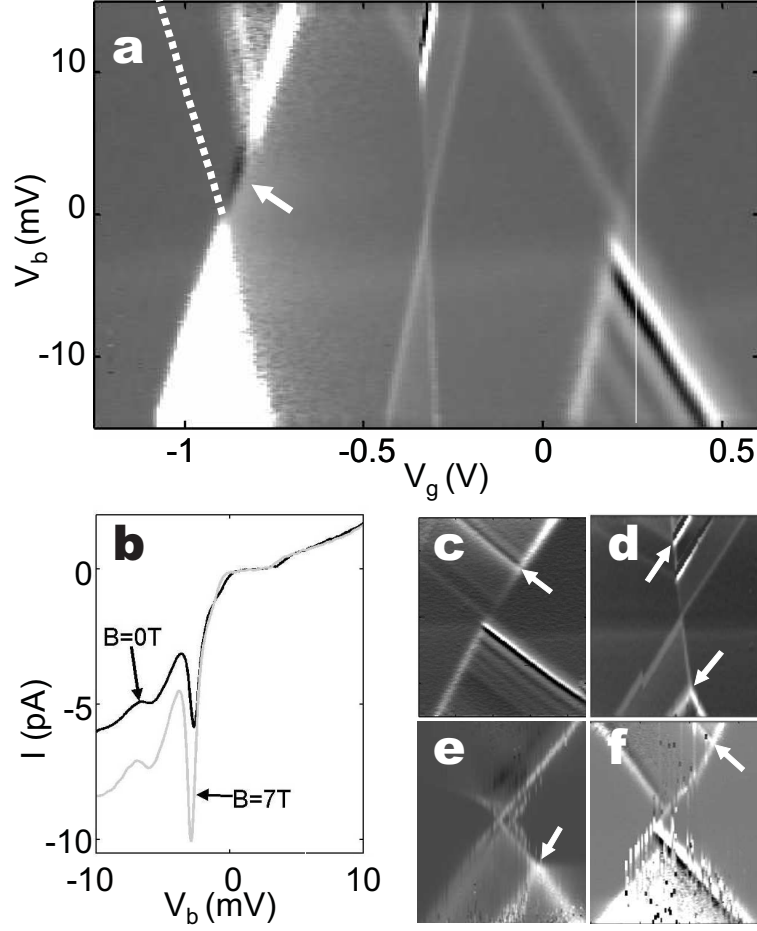
Figure 6.2: a, Differential conductance (gray-scale) as a function of gate voltage (V_g) and bias voltage (V_b) ($T = 3$ K, R=C_6H_4). A region of complete current suppression (left degeneracy point, arrow) and low-energy excitations with negative differential conductance (right degeneracy point) are observed. The dashed line near the left degeneracy point indicates the suppressed diamond edge. (gray-scale from -0.8 nS [black] to 1.4 nS [white]). **b**, I-V_b at the gate voltage indicated in (a) with a line. NDC is clearly visible as a decrease in $|I|$ upon increasing $|V_b|$. Upon applying a magnetic field, current is increased for negative bias. **c-f**, Same as (a) for 4 transport regions in which the 14 meV excitation is indicated with arrows. Bias voltage ranges are: $V_b = \pm 30$ mV, $V_b = \pm 20$ mV, $V_b = \pm 25$ mV, $V_b = \pm 15$ mV, respectively. (c,d) are the right and center charge transport regions of the sample in (a), respectively. (e,f) are measured in devices with the R=$C_{15}H_{30}$ ligands.

PDC and NDC excitations at 2 meV and 3 meV were also observed in a different device, see Fig. 6.3. Although the details varied from sample to sample, these two features were consistently observed. In all cases, the 14 meV excitation
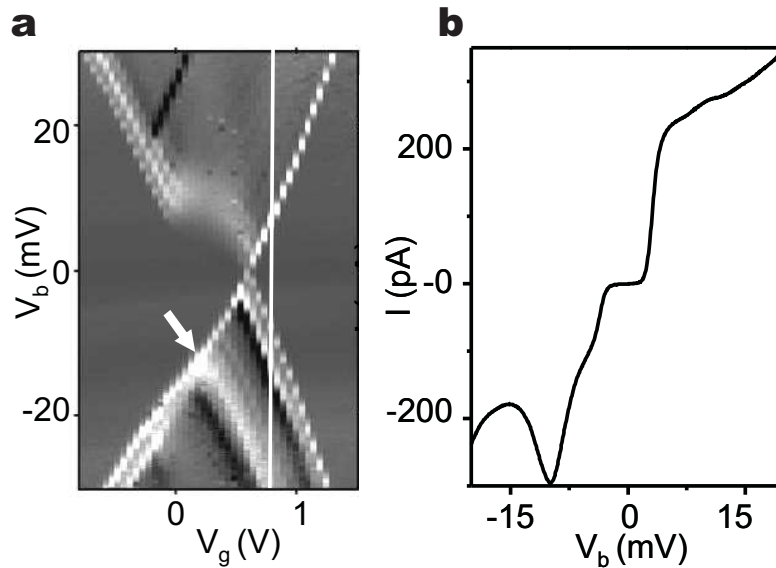
Figure 6.3: a, Differential conductance (grayscale) as a function of gate voltage (V_g) and bias voltage (V_b) for another device ($T = 1.5$ K, R=C$_6$H$_4$) in which the 2 meV and 3 meV excitations are also observed (negative bias). The 14 meV excitation is indicated by a white arrow. The origin of the step in the diamond edge at positive bias is unclear, but most likely not related to the magnetic properties of the molecule. (gray-scale from -3 nS [black] to 10 nS [white]) **b**, I-V_b along the line in (a).

is visible, suggesting that this feature originates in the core of the molecule. We emphasize that we never observed similar low-energy features (CCS or NDC) in bare gold samples or in samples with other molecules deposited despite measuring over one thousand junctions in total.

6.4   Transport model

The observations of CSS and NDC lines at low energy do not follow in a straightforward way from conventional Coulomb blockade theory. For a qualitative comparison to the experimental data, we have developed a standard sequential tunneling model that incorparates the spin-Hamiltonian description of the high-spin ground state of Mn$_{12}$ and its ladder of spin excited states (see Fig. 6.4). Both the total spin of the molecule S and its projection M on the intrinsic anisotropy axis of the molecule (the z-axis) are taken into account. Briefly: the spin-selection rules $|\Delta S|, |\Delta M| = \frac{1}{2}$ apply to adding or subtracting an electron. Spin states of the molecule which differ by more than $\frac{1}{2}$ from the ground states are accessible via subsequent tunnel processes, but only if each step in the sequence is ener-

getically allowed. A sequence of tunnel processes can result in a non-equilibrium population of certain excited states that can only be depopulated slowly by a violation of the spin-selection rules induced by QTM. Transport is then hindered or blocked at sufficiently low temperatures leading to NDC or CCS.

Our calculations (see Fig. 6.4) take as a starting point the basic spin-Hamiltonian for a SMM in charge state N ($N = n$ neutral, $N = n - 1$ oxidized, $N = n + 1$ reduced) and two S-states $\alpha = 0, 1$ for each charge state (energy splitting Δ_N) and total spin $S_{N\alpha}$:

$$H_{N\alpha} = -D_{N\alpha}S_z^2 + B_2 \left(S_x^2 - S_y^2\right), \tag{6.1}$$

where $D_{N\alpha} > 0$ is an anisotropy constant and B_2 the lowest order QTM perturbation due to deviations from perfect axial symmetry. For $B_2 = 0$ this Hamiltonian gives rise to a ladder consisting of the $2S_{N\alpha} + 1$ different M states, see Fig. 6.4a. The states $M = \pm S_{N0}$ are degenerate ground states of the molecule and are separated by the magnetic anisotropy barrier (MAB). Transition rates between spin states upon adding or subtracting an electron are determined by Clebsch-Gordan coefficients and spin selection rules. We consider weak QTM (small B_2) where this picture is still correct up to weak violations of the spin-selection rules which are taken into account. Electronic- and spin-excitation relaxation rates are assumed to be much smaller than the tunnel rates [25].

6.4.1 Model parameters

Measurements show that the MAB of the neutral Mn_{12} molecule ($D_{n0}S_{n0}^2$) equals 5.6 meV. Recently, it has been demonstrated that the first excited spin state in a neutral Mn_{12} derivative has $S_{n,1} = 9$ and lies about Δ_n=4 meV above the $S_{n,0} = 10$ ground state [26], as theoretically predicted by Park et al. [27]. Little is known about positively- or negatively- charged Mn_{12} clusters, except that one-electron reduced species have a $S_{n+1,0} = 9\frac{1}{2}$ ground state and a lower MAB [28]. We therefore have performed calculations for various values of the remaining parameters and found that NDC and CCS are generic features whenever (i) the MAB is charge state dependent (ii) the spin multiplets within a charge state overlap in energy ($D_{N0}S_{N0}^2 > \Delta_N$).

6.4.2 Results

An example of CCS obtained from calculations is indicated in Fig. 6.4b for the $n-1 \leftrightarrow n$ transition and parameters listed in Ref. [29]. In contrast to conventional spin-blockade, the current is not blocked in the narrow region where only the
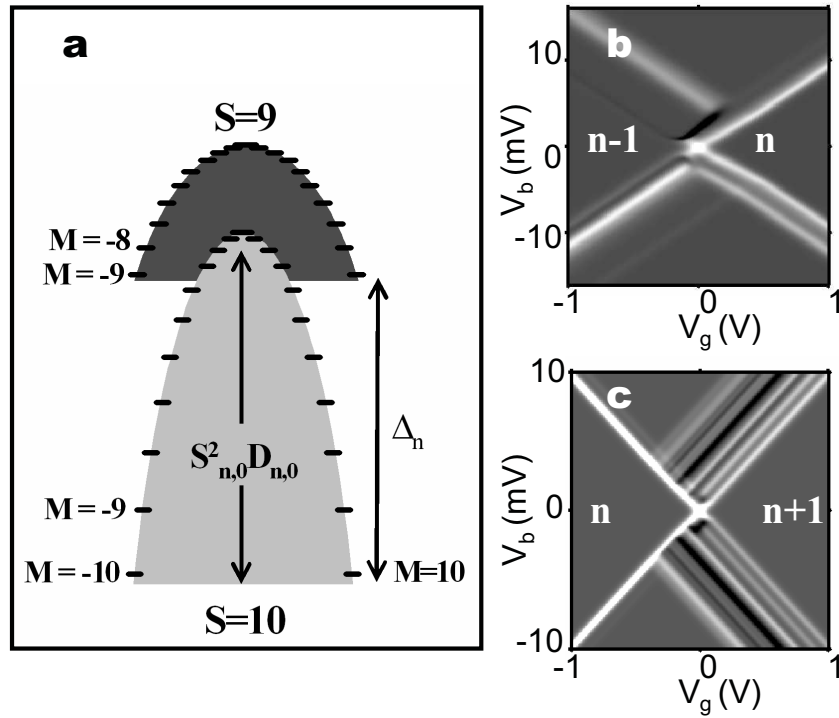
Figure 6.4: Model calculations. **a**, Energy diagram of the S_z states for the electronic ground state ($\alpha = 0$, light gray) and first excited state ($\alpha = 1$, dark gray) of the neutral molecule ($N = n$). **b,c**, Differential conductance (grayscale from -0.8 [black] to 1 [white] a.u.) modeling CCS (b) and NDC (c).

ground states of the molecule are accessible. This is also observed experimentally. Excitations with NDC are obtained for the $n \leftrightarrow n + 1$ transition (see Fig 6.4c). The mechanism is similar as for CCS, but requires a lower MAB of the charged ground state spin multiplet [29]. It is important to note that other parameter choices also give rise to CCS and NDC, so that a quantitative comparison cannot be made at the moment.

6.5   Discussion

Other explanations for the NDC and CCS have also been considered. Both intrinsic and extrinsic (i.e. lead) properties could result in the observation of NDC. The observation of an NDC excitation in different samples implies that it results from an intrinsic property of the molecule, such as vibrational excitations. In some rather special situations they are also predicted to result in NDC [30, 31, 32, 33]. A CCS feature of the type observed here, however, has not been reported. Our model naturally gives rise to CCS and NDC due to the intrinsic

properties of the magnetic molecule: charge induced distortion of the magnetic parameters and low-lying magnetic and spin-excitations.

The low-energy features of the different transport regions in Fig. 6.2a are not identical, possibly because they correspond to different charge state transitions. In addition, the (magnetic) parameters may be effected by the different coupling to the electrodes. Since the lines in the transport regions correspond to sequences of transitions rather than to a single excitation, the pattern is sensitive to variations of the magnetic parameters (and other parameters like temperature and tunnel coupling).

The effect of a magnetic field in transport experiments is much less obvious than in magnetic measurements on ensembles of molecules. Firstly, the angle of the external field with respect to the easy axis of the molecule is unknown and cannot be controlled in our experimental setup. A transverse field leads to mixing of spin eigenstates, allowing transitions which are inhibited due to spin selection rules in the absence of a field, whereas a longitudinal field will only shift the energies of the S_z states. However, estimates for the anisotropic g factors in the charge states are required to extend our basic model. Furthermore, the electron tunnel couplings can be modified by the field. The increase of the current upon applying a magnetic field, Fig. 6.2b, may be related to all of the above effects but a full analysis of the magnetic field effects is beyond the scope of the present paper.

6.6 Conclusion

In conclusion, we have measured transport through single Mn_{12} molecules that are weakly coupled to gold electrodes. Current suppression and negative differential conductance on the energy scale of the anisotropy barrier have been observed. These features can be understood qualitatively with a model, that combines the spin properties of the molecule with standard sequential tunneling theory. These results provide a new direction in the study of single-molecule magnets and possibly lead to electronic control of nano-magnets.

References

[1] J. Park *et al.* , Nature **417**, 722 (2002).

[2] W. Liang *et al.* , Nature **417**, 725 (2002).

[3] S. Kubatkin *et al.* , Nature **425**, 698 (2003).

[4] H. Park *et al.* , Nature **407**, 57 (2000).

[5] L. H. Yu *et al.* , Phys. Rev. Lett. **93**, 266802 (2004).

[6] A. N. Pasupathy *et al.* , Nano Lett. **5**, 203 (2005).

[7] R. Sessoli, D. Gatteschi, A. Caneschi, and M. A. Novak, Nature **365**, 141 (1993).

[8] D. Gatteschi and R. Sessoli, Angew. Chem. Int. Ed. **42**, 268 (2003).

[9] J. R. Friedman, M. P. Sarachik, J. Tejada, and R. Ziolo, Phys. Rev. Lett. **76**, 3830 (1996).

[10] E. J. L. McInnes *et al.* , J. Am. Chem. Soc. **241**, 9219 (2002).

[11] M. Cavallini *et al.* , Angew. Chem. Int. Ed. **44**, 888 (2005).

[12] M. Mannini *et al.* , Nano Lett. **5**, 1435 (2005).

[13] G-H Kim and T-S Kim, Phys. Rev. Lett. **92**, 137203 (2004).

[14] K. Kim *et al.* , Appl. Phys. Lett. **85**, 3872 (2004).

[15] D. Weinmann, W. Häusler, and B. Kramer. , Phys. Rev. Lett. **74**, 984 (1995).

[16] Hüttel *et al.* , Eur. Phys. Lett. **62**, 712 (2003).

[17] A. Cornia *et al.* , Angew. Chem. Int. Ed. **42**, 1645 (2003).

[18] H. Park *et al.* , Appl. Phys. Lett. **75**, 301 (1999).

[19] The yield was similar for both types of derivatives. Two of the stable samples where obtained with the R=C$_{15}$H$_{30}$ derivative.

[20] M. R. Pederson, N. Bernstein, and J. Kortus, Phys. Rev. Lett. **89**, 097202 (2002).

[21] R. Sordan, K. Balasubramanian, M. Burghard, and K. Kern, Appl. Phys. Lett. **87**, 013106 (2005).

[22] A. A. Houck *et al.* , Nano Lett. **5**, 1685 (2005).

[23] H. B. Heersche *et al.* , Phys. Rev. Lett. **96**, 017205 (2006).

[24] H.S.J. van der Zant *et al.* , Faraday discussions **131**, 347 (2006).

[25] W. Wernsdorfer *et al.* , Eur. Phys. Lett. **50**, 552 (2000).

[26] K. Petukhov *et al.* , Phys. Rev. B **70**, 054426 (2004).

[27] K. Park and M. R. Pederson, Phys. Rev. B **70**, 054414 (2004).

[28] N.E. Chakov *et al.* , Inorg. Chem. **44**, 5304 (2005).

[29] Model parameters (energies in [meV]) $(S_{n,0}, S_{n,1}) = (10, 9)$, $(D_{n,0}, D_{n,1}) = (0.056, 0.04)$ $\Delta_n = 4.0$ and $B_2 = 10^{-4}$. Parameters for CCS, $(S_{n-1,0}, S_{n-1,1}) = (9\frac{1}{2}, 9\frac{1}{2})$, $(D_{n-1,0}, D_{n-1,1}) = (0.02, 0.05)$, $\Delta_{n-1} = 1.3$, $\Gamma_L/\Gamma_R = 2$, and $T = 2$ K. Parameters for NDC, $(S_{n+1,0}, S_{n+1,1}) = (9\frac{1}{2}, 9\frac{1}{2})$, $(D_{n+1,0}, D_{n+1,1}) = (0.02, 0.02)$, $\Delta_{n+1} = 0.6$, $B_2 = 10^{-5}$, $\Gamma_L/\Gamma_R = 10$, and $T = 1$ K. The NDC *strength* can only be reproduced for a temperature lower than the experimental one in Fig. 6.2, 6.3.

[30] J. Koch and F. von Oppen. Phys. Rev. Lett. **94**, 206804 (2005).

[31] M. R. Wegewijs and K. C. Nowack, New J. Phys. **7**, 239 (2005).

[32] K. C. Nowack and M. R. Wegewijs, cond-mat/0506552 (2004).

[33] A. Zazunov, D. Feinberg, and T. Martin, cond-mat/0510066.

Chapter 7

Kondo effect in the presence of magnetic impurities

H.B. Heersche, Z. de Groot, J.A. Folk, L.P. Kouwenhoven, H.S.J. van der Zant, A. A. Houck, J. Labaziewicz, I.L. Chuang

We measure transport through gold grain quantum dots fabricated using electromigration, with magnetic impurities in the leads. A Kondo interaction is observed between dot and leads, but the presence of magnetic impurities results in a gate-dependent zero-bias conductance peak that is split due to an RKKY interaction between the spin of the dot and the static spins of the impurities. A magnetic field restores the single Kondo peak in the case of an antiferromagnetic RKKY interaction. This system provides a new platform to study Kondo and RKKY interactions in metals at the level of a single spin.

7.1   Introduction

The observation of the Kondo effect in quantum dot systems has generated re-
newed experimental and theoretical interest in this many-body effect. The Kondo
effect is the screening of a localized spin by surrounding conduction electrons. The
localized spin can take the form of a magnetic atom, or the net spin in a quan-
tum dot (QD). The Kondo effect has been studied extensively in quantum dot
systems such as semiconductor quantum dots [1, 2], carbon nanotubes [3], and
single molecules contacted by metal leads [4, 5, 6, 7].

The Kondo effect in a quantum dot can be used to probe interactions of a
local spin with other magnetic moments. Whereas the Kondo effect enhances the
zero-bias conductance through spin flip processes, exchange interactions tend to
freeze the spin of the QD. This competition results in a suppression and split-
ting of the Kondo resonance. The Kondo effect has been used to study the
direct interaction between spins on a double dot [8, 9], the exchange interaction
with ferromagnetic leads [10], and the indirect Ruderman-Kittel-Kasuya-Yoshida
(RKKY) interaction of two QDs separated by a larger dot [11]. In bulk metals
with embedded magnetic impurities, the competition between the Kondo effect
and RKKY coupling between impurities gives rise to complex magnetic states
such as spin glasses [12].

In this Letter, we use the Kondo effect to study the RKKY interaction between
the net spin of a quantum dot and magnetic impurities in the leads of an all-metal
device. The system consists of a small gold grain in the vicinity of magnetic
cobalt impurities, Fig. 7.2a. By itself, the Kondo interaction with the net spin on
such a grain induces a zero-bias peak in conductance. This feature is regularly
observed in samples without impurities [13]. In the present experiment, cobalt
impurities deposited intentionally cause the zero-bias peak to split. The splitting
is explained by the RKKY interaction between the impurities and the spin of the
grain. Temperature and magnetic field dependence of the split zero-bias peak
(SZBP) confirm this interpretation.

7.2   Sample fabrication

Measurements are performed on gold wires that have been broken by a controlled
electromigration process, which is tailored to produce narrow gaps. Two substan-
tially different procedures were followed, in two laboratories, but yielded similar
results. Both procedures begin with a 12 nm gold bridge on top of an Al/Al_2O_3
gate electrode, see Fig. 7.1a. A sub-monolayer of cobalt (Co) is evaporated on
the sample before electromigration. For the first method, we monitor the change

in resistance during electromigration (at room temperature) and adjust the applied voltage to maintain a constant break rate [13, 14]. For the second, the junctions are broken by ramping the voltage across the circuit at $T = 4.2$ K and a series resistor is used to control the final gap size. The series resistance in our measurements was typically 50 Ω.

7.3 The Kondo effect in bare gold junctions

The differential conductance of the junctions is measured after breaking as a function of gate and bias voltage. As in samples without Co [13], Coulomb blockade and/or the Kondo effect were observed in 30 percent of the junctions that showed any conductance (this percentage depends on the precise electromigration procedure). Both effects are attributed to transport through ultra-small gold grains, small enough to act as quantum dots with discrete energy levels [13, 15]. This explanation is supported by the observation of electroluminescence from 18-22 atom gold grains in samples prepared in a similar manner [16].

An example of a gate dependent Kondo resonance in a gold grain *without* Co is shown in Fig. 7.1b. The Kondo effect enhances the differential conductance $G \equiv dI/dV_b$, around zero bias (dotted line) left of the charge degeneracy point (crossing point of Coulomb diamond edges, dashed lines). The zero-bias peak in G is suppressed with increasing temperature (Figs. 7.1(b,c)). The height of the peak fits closely to the predicted functional form, $G(T) = G(0)/[1 + (2^{1/s} - 1)(T/T_K)^2]^s$ [17, 18] with $s = 0.22$ for a spin $\frac{1}{2}$ dot, yielding a Kondo temperature $T_K \approx 60$ K.

7.4 Kondo effect and magnetic impurities

When magnetic impurities are scattered on the surface of the wire before breaking, over ten percent of the samples [19] show a split peak around zero bias rather than the single peak described above [20]. In Fig. 7.3a, the differential conductance of one such device is plotted as a function of gate and bias voltage. Left from $V_g = -1$ V, a split zero-bias peak is observed; no SZBP is present at the right hand side. The onset of the SZBP coincides with a change in the number of electrons on the gold grain, as indicated by the diamond edge that intersects at $V_g \approx -1$ V (the fact that not all four diamond edges can be resolved is typical for these strongly coupled dots [7]). The parity effect observed in Fig. 7.3a, like that in Fig. 7.1b, is explained by a change of the net spin of the dot on the addition of an extra electron.
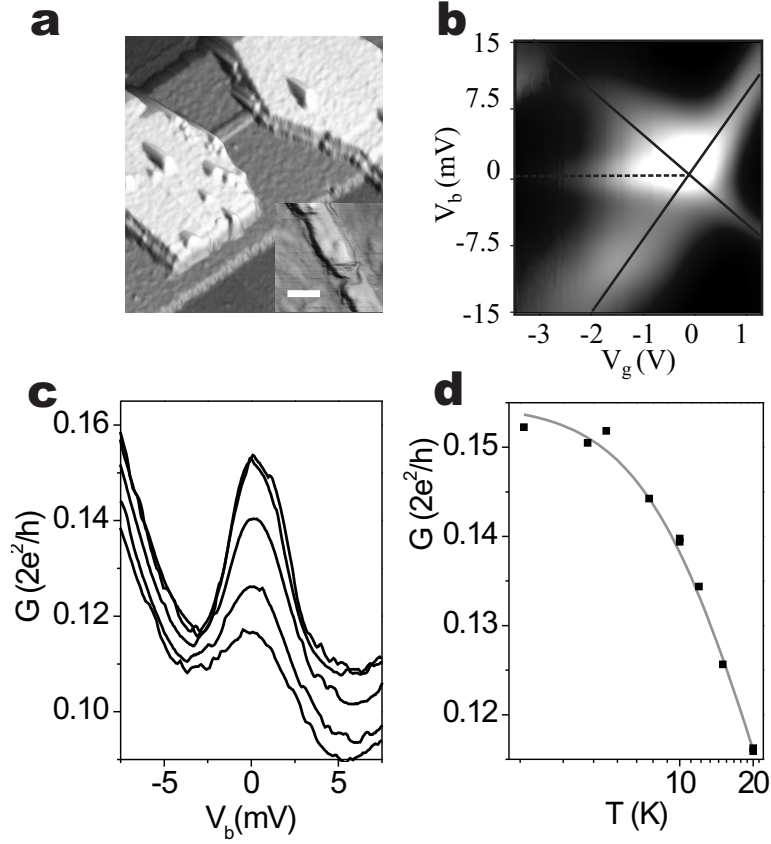
Figure 7.1: Kondo effect in a gold grain quantum dot without magnetic impurities. **a**, Atomic force microscopy picture of the device. A thin (12 nm) Au wire, connected to thick leads, lies on top of an oxidized Al gate (width 1 μm). *Inset* After electromigration, a small gap ($\lesssim$1 nm, too small to resolve) is created containing small grains. (Scale bar corresponds to 100nm). **b**, Differential conductance as a function of bias (V_b) and gate voltage (V_g). At $V_g \sim -0.2$ V, four diamond edges (peaks in $G = dI/dV_b$) come together in a charge degeneracy point. At the left hand side of the degeneracy point a conductance enhancement around $V_b = 0$ V is observed due to the Kondo effect. The dashed (diamond edges) and dotted (Kondo effect) lines are drawn as guides to the eye. Color scale ranges from 2 μS (black) to 22 μS (white). $T = 2.3$ K. **c**, The height of the Kondo peak (at $V_g = -2$ V) decreases as a function of temperature. Curves correspond to (fttb) T =2.3, 4.2, 10, 15, and 20 K. **d**, Fit (gray curve) of the peak height to the expected temperature dependence suggests $T_K \approx 60$ K.

The SZBP can be explained by a competition between the Kondo effect and the RKKY coupling of the spin on the dot to one or more magnetic impurities in its vicinity (see Fig. 7.2a for a schematic of the system). The relevant energy scales are T_K and the RKKY interaction strength I. An RKKY interaction suppresses
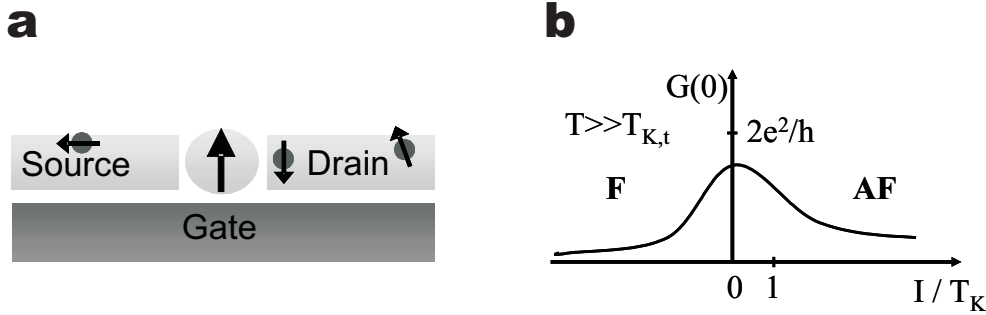
Figure 7.2: A gold grain quantum dot in the presence of magnetic impurities. **a**, Schematic of the device. **b**, Sketch of the expected dependence of the zero-bias conductance $G(0)$ on the scaled RKKY coupling strength (I/T_k) , at temperatures higher than the triplet Kondo temperature $T_{K,t}$ [26] . $G(0)$ is suppressed both for strong ferromagnetic (F) and antiferromagnetic (AF) interactions.

elastic spin-flip processes and therefore suppresses the Kondo effect for low bias. Recently, the competition between RKKY interaction and the Kondo effect was studied theoretically by Vavilov *et al.* [21] and Simon *et al.* [22].

Peaks in conductance at $eV_b \simeq \pm I$ correspond to the voltage above which inelastic spin flip processes are energetically allowed. The devices measured in Fig. 7.3 both give peak separations of 6 ± 1 meV, yielding $I = 3$ meV. Most devices that were measured fell in the range 1 meV $\lesssim I \lesssim$ 3 meV. The Kondo temperature, estimated from the total width of the SZBP, is found to be of the same order as I/k_B.

7.4.1 Temperature dependence

The temperature dependence of the zero-bias conductance is expected to be non-monotonic due to the competition between the Kondo effect and RKKY interaction [23, 24, 25]. With increasing temperature, conductance increases due to thermal broadening of the peaks at $eV_b = \pm I$. The temperature of maximum zero-bias conductance is $T_m \sim I/k_B$, where both peaks have come together to form a single peak around zero bias. For $T > T_m$, the zero-bias conductance decreases for increasing temperature, similar to the Kondo effect without interactions. This behavior is also observed experimentally. The temperature dependence of the SZBP in Fig. 7.3a is shown in Fig. 7.4. Here $T_m = 25 \pm 5$ K$\simeq 0.7I$, with I extracted from the peak separation.
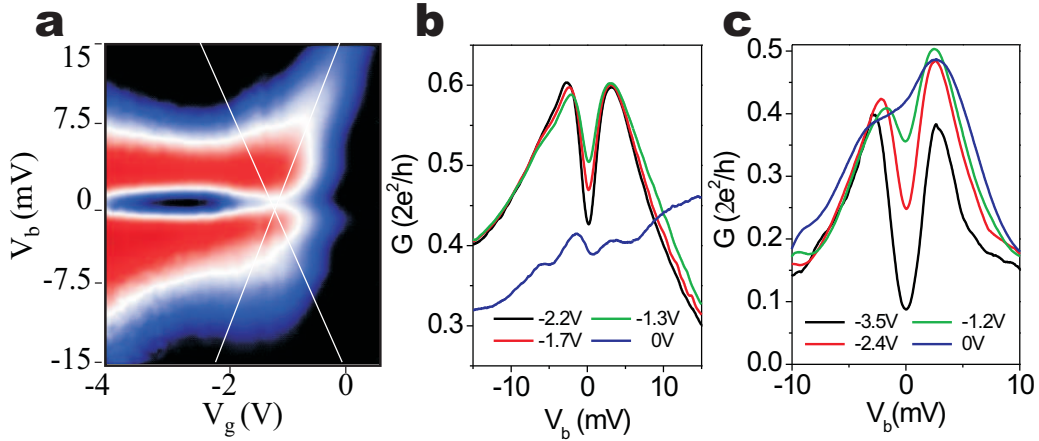
Figure 7.3: Split zero-bias peak (SZBP) of a gold grain quantum dot in the presence of magnetic impurities. **a**, Differential conductance G as a function of bias (V_b) and gate voltage (V_g). The split zero-bias anomaly vanishes when an extra electron is added to the quantum dot ($V_g = -1$ V). Dashed lines (diamond edges) are a guide to the eye. Color scale from 28 μS (black) to 55 μS (white). $T = 2.3$ K. **b**, Line plots from (**a**), showing suppression of zero-bias dip near charge degeneracy. **c**, $G \equiv dI/dV_b$ versus bias for several gate voltages from a different device. Here the Kondo peak can be nearly restored with the gate. The depth of the zero-bias suppression is strongly gate dependent, but the peak separation remains constant.

7.4.2   Magnetic field dependence: F vs. AF interaction

The sign of I is determined by the phase ϕ of the RKKY interaction, which is periodic in distance with the Fermi wavelength. Depending on the sign of I, the RKKY interaction is ferromagnetic ($I < 0$) or antiferromagnetic ($I > 0$). Both ferromagnetic (F) and antiferromagnetic (AF) interactions suppress the $S = \frac{1}{2}$ Kondo effect when $|I| \gtrsim T_K$ and $|eV_b| < |I|$. For an AF interaction, the dot and impurity spins form an unscreened singlet ($S = 0$) state. In this case, the single peak due to an $S = \frac{1}{2}$ Kondo effect is replaced by an SZBP with peaks at $eV_b = \pm I$, at which bias the singlet-triplet transition becomes energetically available. For a F interaction, the spins form a triplet ($S = 1$) state. The Kondo temperature associated with the triplet state, T_{K-t}, is much smaller than T_K [22, 21]. At temperatures larger than T_{K-t}, an SZBP is observed also for a ferromagnetic I. As a result, the zero-bias conductance $G(0)$ as a function of the RKKY interaction I is maximum at $I \simeq 0$ (assuming $T > T_{K-t}$) [26] (see Fig. 7.2b).

The magnetic field dependence of the SZBP depends on the sign of I, and is therefore an important tool to determine whether the interaction is F or AF.
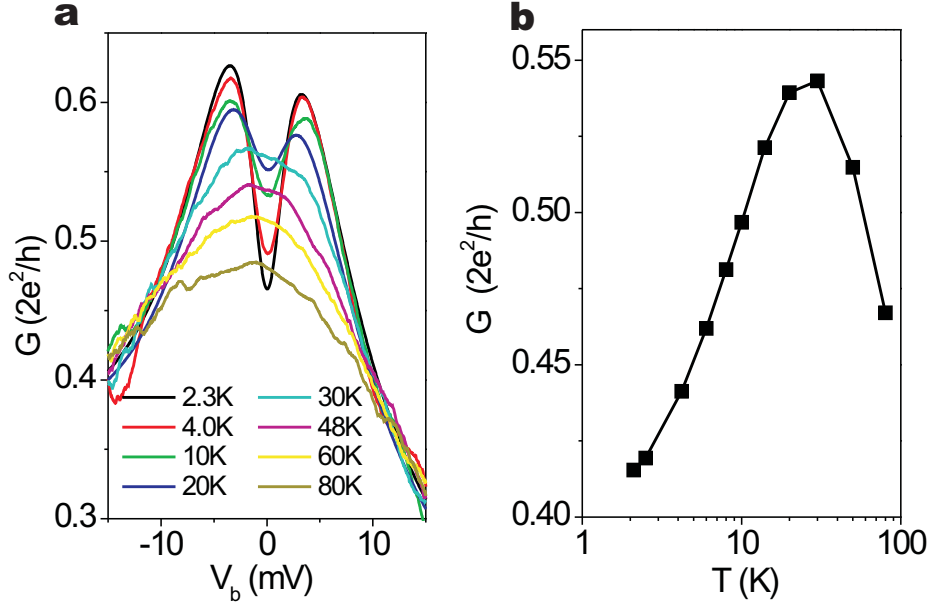
Figure 7.4: Temperature dependence of the split zero-bias peak (same device as in Fig. 7.3(b)). **a**, $G \equiv dI/dV_b$ as a function of bias for different temperatures. **b**, Non-monotonic temperature dependence of the conductance at $V_b = 0$ V. Data points are measurements, the line is a guide to the eye.

An external field can restore the Kondo effect if the RKKY interaction is AF [22, 21]. This is because the energy between the singlet ground state and the $|S=1,m=-1\rangle$ triplet state decreases with $|B|$, Fig. 7.5a. A Kondo state is restored at $B = I/(g\mu_B)$, where singlet and triplet states are degenerate and the external field compensates the AF interaction. For an F interaction, on the other hand, the peak spacing is expected to increase monotonically with $|B|$ because the splitting between the triplet $|S=1,m=-1\rangle$ ground state and the singlet state also increases.

A characteristic field dependence for the AF case is shown in Fig. 7.5b. Upon increasing the field, the dip in the SZBP gradually diminishes until the Kondo peak is fully restored at 4.5 T [27]. Above 4.5 T the Kondo peak splits again. Because the g-factors of the dot spin and the magnetic impurity may be different, it is difficult to compare I with the Zeeman energy at 4.5 T. In two of the devices showing an SZBP at zero magnetic field, the splitting increased with $|B|$ as is expected for an F interaction (see Fig. 7.5c).

Both AF and F interactions are observed in different devices because the sign of I depends on the exact device geometry. The surprising fact that more AF interactions are observed compared to F interactions may result from experimental
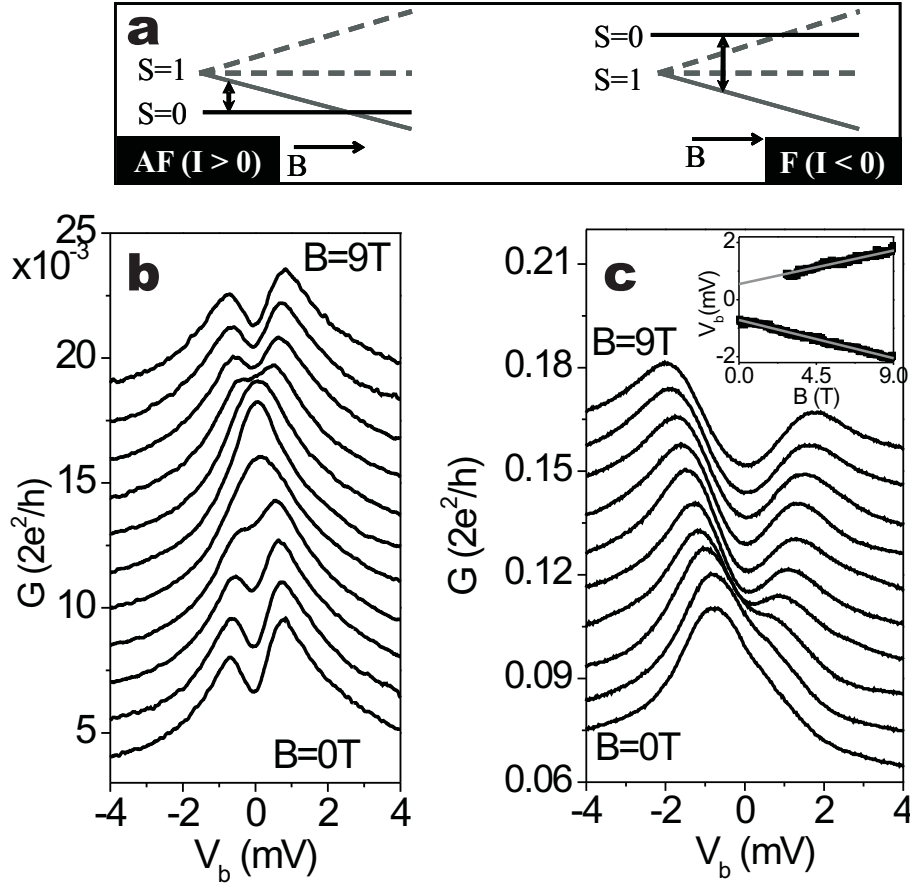
Figure 7.5: Magnetic field dependence of the split zero-bias anomaly. **a**, For anti-ferromagnetic (AF) interaction, the singlet-triplet transition energy (arrow) decreases, then increases with B-field. For ferromagnetic (F) interaction, the triplet-singlet energy always increases with field. **b,c**, Line plots are taken at different values of the external magnetic field, increasing from $B = 0$ T (bottom line) to B=9 T (top line) in steps of 0.9 T. Data taken at $T = 250$ mK b) Restoration of the Kondo effect at finite field, typical for AF interaction between to spins. Line plots offset by $1.5 \times 10^{-3}(2e^2/h)$, for clarity. **c**, For a F interaction the peak separation increases linearly with $|B|$. The peak separation at $B = 0$ T is determined by extrapolating from peak positions to zero field (inset) and yields 1.4 ± 0.3 meV. Line plots offset by $1 \times 10^{-2}(2e^2/h)$.

temperatures below T_{K-t}. In that case a triplet Kondo peak could be confused with an $S = \frac{1}{2}$ Kondo peak. Interactions with several cobalt impurities at varying distances may contribute to the imbalance as well.

7.4.3 Tuning between Kondo- and AF/F-phases with a gate

A characteristic feature of these samples is that the dip around zero bias becomes more pronounced away from the charge degeneracy point, whereas the peak positions are insensitive to the gate (see Figs. 7.3b,c). A gate changes the coupling strength J_1 between the spin of a QD and the conduction electrons in the leads, $J_1 \propto 1/V_g$. The Kondo temperature depends exponentially on J_1, $T_K \propto \exp(-1/\rho|J_1|)$, so T_K rapidly decreases away from the degeneracy point [18]. Compared to T_K, the RKKY interaction energy $I \propto J_1 J_2 \cos \phi$ depends less strongly on J_1, so the ratio I/T_K increases away from the degeneracy point (J_2 is the coupling of the spin of the magnetic impurity to the free electrons in the leads). A quantum phase transition has been predicted between Kondo and RKKY phases as a function of I/T_K, which is replaced by a smooth crossover at higher temperatures or when particle-hole symmetry is broken [30, 29, 21, 22] (Fig. 7.2b). The transition from SZBP to Kondo peak in Fig. 7.3c may indicate a gate induced transition between RKKY and Kondo phases.

7.5 Discussion and conclusion

Other mechanisms that can lead to an SZBP have also been considered, but can be ruled out for several reasons. First, nearly degenerate singlet-triplet states *within* the dot may result in a SZBP [32, 31, 28]. However, this option is disregarded since it does not explain the observed dependence on the presence of magnetic impurities. Second, an SZBP at zero magnetic-field was recently observed in a single C_{60} molecule QD with ferromagnetic leads [10]. The (gate-independent) SZBP in that work was attributed to exchange splitting of the Kondo peak by the ferromagnetic leads. Evidence for this explanation was provided by the dependence of the splitting on the relative orientation of the ferromagnetic electrodes. The absence of hysteresis with magnetic field in any of our measurements, together with the relatively low ($\lesssim 1\ \%$) Co concentration, make this an unlikely mechanism to explain our results.

In conclusion, we have observed a gate dependent SZBP in electromigrated gold break junctions in the presence of magnetic impurities. These observations are consistent with an RKKY interaction between the local spin of a small gold grain and magnetic Co impurities. Magnetic field dependence distinguishes between F and AF interactions. This system is a flexible platform to study the interaction between static magnetic impurities and the spin on a tunable quantum dot in an all-metal system. It bridges the gap between studies of the RKKY

and Kondo interactions in bulk metals, and measurements of the two effects in semiconductor quantum dots.

We thank R. Lopez, J. Martinek, P. Simon, and M. G. Vavilov for useful discussions.

References

[1] D. Goldhaber-Gordon *et al. Kondo effect in a single-electron transistor.*, Nature **391**, 156 (1998).

[2] T. H. Oosterkamp S. M. Cronenwett and L. P. Kouwenhoven, *A tunable kondo effect in quantum dots*, Science **281**, 540 (1998).

[3] J. Nygård, D. H. Gobden, and P. E. Lindehof, *Kondo physics in carbon nanotubes*, Nature **408**, 342 (2000).

[4] W. Liang *et al.* , *Kondo resonance in a single-molecule transistor.*, Nature, **417**, 725 (2002).

[5] J. Park *et al.* , *Coulomb blockade and the kondo effect in single-atom transistors.*, Nature **417**, 722 (2002).

[6] L. H. Yu and D. Natelson, *The kondo effect in C60 single-molecule transistors.* Nanoletters **4**, 79 (2004).

[7] L. H. Yu and D. Natelson, *Strong kondo physics and anomalous gate dependence in single-molecule transistors.*, cond-mat/0505683, 2005.

[8] A. M. Chang H. Jeong and M. R. Melloch, *The kondo effect in an artificial quantum dot molecule*, Science **293**, 2221 (2001).

[9] J. C. Chen, A. M. Chang, and M. R. Melloch. *Transition between quantum states in a parallel-coupled double quantum dot.* Phys. Rev. Lett. **92**, 176801 (2004).

[10] A. N. Pasupathy *et al.* , *The kondo effect in the presence of ferromagnetism*, Science **306**, 86 (2004).

[11] N. J. Craig *et al.* , *Tunable nonlocal spin control in a coupled-quantum dot system.*, Science **304**, 565 (2004).

[12] A. C. Hewson, *The Kondo Problem to Heavy Fermions*, Cambridge Univ. Press, Cambridge (1993).

[13] A. A. Houck *et al.* , *Kondo effect in electromigrated gold break junctions.*, Nano Lett., **5**, 1685 (2005).

[14] Strachan, D. R. et al. *Controlled fabrication of nanogaps in ambient environment for molecular electronics.* Appl. Phys. Lett. **86**, 043109 (2005).

[15] R. Sordan *et al.* , *Coulomb blockade phenomena in electromigration breakjunctions*, Appl. Phys. Lett. **87**, 013106 (2005).

[16] J. I. Gonzalez *et al.* , *Quantum mechanical single-gold-nanocluster electroluminescent light source at room temperature.* Phys. Rev. Lett., **93**, 147402 (2004).

[17] T. A. Costi, A. C. Hewson, and V. Zlatić, J. Phys. Condens. Matter **6**, 2519 (1994).

[18] D. Goldhaber-Gordon *et al.* , Phys. Rev. Lett. **81**, 5225 (1998).

[19] For the devices broken with feedback and measured at $T = 250$ mK, split zero bias peaks were observed in 18/62 devices and unsplit Kondo peaks in 13/62 devices. At $T = 1.6$ K and no feedback, these numbers were 9/120 and 17/120, respectively.

[20] An SZBP was also observed in 2 samples without Co, most likely due to the presence of unintended magnetic impurities in the gold.

[21] M. G. Vavilov and L. I. Glazman, *Transport spectroscopy of kondo quantum dots coupled by RKKY interaction*, Phys. Rev. Lett. **94**, 086805 (2005).

[22] P. Simon *et al.* , *Ruderman-kittel-kasuya-yosida and magnetic-field interactions in coupled kondo quantum dots*, Phys. Rev. Lett. **94**, 086602 (2005).

[23] M. Pustilnik and L. I. Glazman, *The kondo effect in real quatum dots*, Phys. Rev. Lett. **87**, 216601 (2001).

[24] R. López, R. Aguado, and G. Platero, *Nonequilibrium transport through double quantum dots: Kondo effect versus antiferromagnetic coupling*, Phys. Rev. Lett., **89**, 136802 (2002).

[25] R. Aguado and D. C. Langreth. *Kondo effect in coupled quantum dots: A noncrossing approximation study.*, Phys. Rev. B, **67**, 245307 (2003).

[26] M. Pustilnik and L. I. Glazman, *Kondo effect induced by a mangnetic field*, Phys. Rev. B **64**, 045328 (2001).

[27] Transitions between singlet and triplet excited states [21, 22] are not observed. This is probably due to their low intensity and/or smoothing by temperature.

[28] A. Kogan *et al.* , *Singlettriplet transition in a single-electron transistor at zero magnetic field.* Phys. Rev. B, **67**, 113309 (2003).

[29] B. A. Jones and C. M. Varma, *Critical point in the solution of the two magnetic impurity problem.* Phys. Rev. B **40**, 324 (1989).

[30] B. A. Jones and C. M. Varma, *Study of two magnetic impurities in a fermi gas*, Phys. Rev. Lett., **58**, 843 (1987).

[31] S. Sasaki *et al. Kondo effect in an integer-spin quantum dot.* Nature **405**,764 (2000).

[32] W. G. van der Wiel *et al.* , *Two-stage kondo effect in a quantum dot at a high magnetic field*, Phys. Rev. Lett. **88**,126803 (2002).

Chapter 8

Bipolar supercurrent in graphene

Hubert B. Heersche, Pablo Jarillo-Herrero, Jeroen B. Oostinga,
Lieven M. K. Vandersypen, and Alberto F. Morpurgo

Graphene - a recently discovered one-atom-thick layer of graphite [1] - constitutes a new model system in condensed matter physics, because it is the first material in which charge carriers behave as massless chiral relativistic particles. The anomalous quantization of the Hall conductance [2, 3], which is now understood theoretically [4, 5], is one of the experimental signatures of the peculiar transport properties of relativistic electrons in graphene. Other unusual phenomena, like the finite conductivity of order e^2/h at the charge neutrality (or Dirac) point [2], have come as a surprise and remain to be explained [5, 6, 7, 8, 9, 10, 11, 12]. Here, we study the Josephson effect [13] in graphene [14]. Our experiments rely on mesoscopic superconducting junctions consisting of a graphene layer contacted by two closely spaced superconducting electrodes, where the charge density can be controlled by means of a gate electrode. We observe a supercurrent that, depending on the gate voltage, is carried by either electrons in the conduction band or by holes in the valence band. More importantly, we find that not only the normal state conductance of graphene is finite, but also a finite supercurrent can flow at zero charge density. Our observations shed light on the special role of time reversal symmetry in graphene and constitute the first demonstration of phase coherent electronic transport at the Dirac point.

8.1   Introduction

Owing to the Josephson effect [13, 15], a supercurrent can flow through a normal conductor (N) placed in between two closely spaced superconducting electrodes (S). For this to happen, transport in the N material must be phase coherent and time reversal symmetry (TRS) must be present. In graphene, the Josephson effect can be investigated in the 'relativistic' regime [14], where the supercurrent is carried by Dirac electrons. However, it is not a-priori clear that graphene can support supercurrents, since other quantum interference phenomena that require both phase coherence and TRS were found to be absent or strongly suppressed in previous experiments [16]. Below we show experimentally that the Josephson effect in graphene is a robust phenomenon, and argue that its robustness is intimately linked to its unique electronic structure.

8.2   Device fabrication

Single and few layer graphene Josephson junctions are fabricated on oxidized Si substrates by mechanical exfoliation of bulk graphite[1], followed by optical microscope inspection in order to locate the thinnest graphitic flakes, and electron beam lithography to define electrical contacts to selected flakes. Figure 8.1a shows an atomic force microscopy (AFM) image of a typical device. We use as superconducting contacts a Ti/Al bilayer (10/70 nm). Titanium ensures good electrical contact to graphene and Al establishes a sufficiently high critical temperature to enable the observation of supercurrents in a dilution refrigeration set-up [17].

8.3   Normal state characterization

Before discussing their superconducting properties, we first characterize the devices with the superconducting electrodes in the normal state. Figure 8.1c shows the two-terminal resistance, R, versus gate voltage, V_G, for one of our samples. The strong V_G-dependence of R provides a first indication that the device consists of at most a few layers of graphene [1] since, due to screening, V_G affects the carrier density only in the bottom one or two layers. For single layers, the position of the resistance maximum corresponds to the gate voltage at which the Fermi energy is located at the Dirac point, V_D, and we typically find that $|V_D| < 20$ V. We unambiguously determine the single layer character of a device by quantum Hall effect (QHE) measurements. Because the superconducting proximity effect
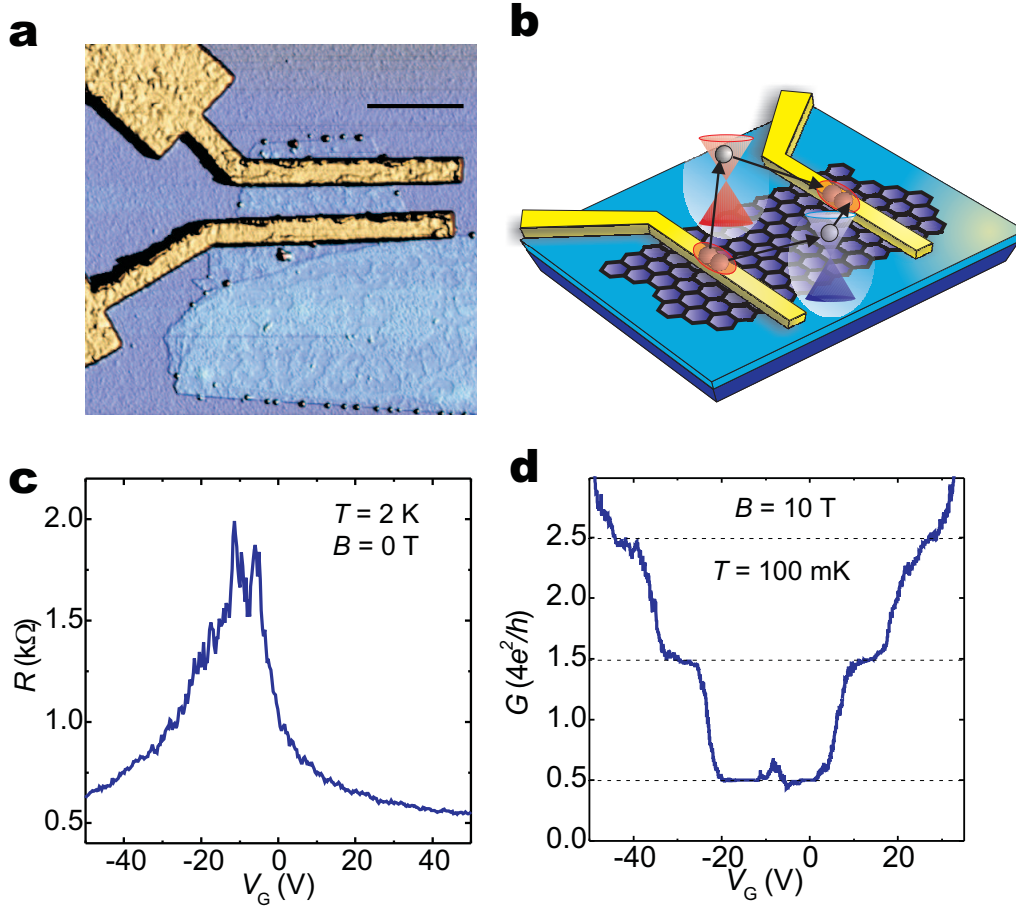
Figure 8.1: Sample characterization. **a**, Atomic force microscope image of a single layer graphene device in between two superconducting electrodes. We have fabricated devices with electrode separations in the range 100-500 nm. **b**, Schematic representation of graphene in between superconducting electrodes. The two electrons in a Cooper pair entering graphene go into different K-valleys. **c**, Two terminal resistance versus gate voltage, V_G, at $T = 30$ mK and a small magnetic field $B = 35$ mT, to drive the electrodes into the normal state. The aperiodic conductance fluctuations are due to random quantum interference of electron waves (see also Fig. 8.4). **d**, Two terminal conductance, G, versus V_G at high magnetic field, $B = 10$ T, and $T = 100$ mK, showing a series of steps at half-integer values of $4e^2/h$, characteristic of the anomalous quantum Hall effect in single layer graphene.

requires two closely spaced electrodes, we can only perform magnetoconductance measurements in a two terminal configuration. In general, the conductance, G, measured in this way is a mixture of longitudinal and Hall signals, but at high fields $G \approx |G_{Hall}|$ (this approximation is exact at the Hall plateaus [18]). Indeed, the measurement of G versus V_G at $B = 10$ T shows clearly identifiable

Hall plateaus at half-integer multiples of $4e^2/h$ (Fig. 8.1d), characteristic of the QHE in single layer graphene [2, 3]. This demonstrates that, even in mesoscopic samples, the quantum Hall effect can be used to identify single layer devices.

8.4   Proximity-induced supercurrents

Cooling down the devices below the critical temperature of the electrodes ($T_c \sim$ 1.3 K) leads to proximity-induced superconductivity in the graphene layer. A direct proof of induced superconductivity is the observation of a Josephson supercurrent [19]. Figure 8.2a shows the current-voltage (I-V) characteristics of a single layer device. The current flows without resistance (no voltage drop at finite current) below the critical current, I_c (what we actually measure is the switching current; the intrinsic I_c may be higher [19, 20]). In our devices, I_c ranged from 10 nA to more than 800 nA (at high V_G). Remarkably, we have measured proximity-induced supercurrents in all the devices that we tested (17 flakes in total, with several devices on some flakes), including four flakes that were unambiguously identified as single layer graphene via QHE (the rest being probably two to four layers thick). This clear observation demonstrates the robustness of the Josephson effect in graphene junctions. (The data shown are representative of the general behaviour observed: All the measurements shown have been taken on the same device, except Fig. 8.2b and 8.4, which correspond to a different single layer device, shown in Fig. 8.1a).

To further investigate the superconducting properties of our devices we measured the dependence of I_c on magnetic field (Fig. 8.2b). The critical current exhibits an oscillatory Fraunhofer-like pattern, with at least 6 visible side lobes, which is indicative of a uniform supercurrent density distribution [21]. The periodicity of the oscillations is theoretically expected to be approximately equal to a flux quantum Φ_0 divided by the junction area. The area that corresponds to the 2.5 ± 0.5 mT period is 0.8 ± 0.2 μm^2, which is in good agreement with the measured device area (0.7 ± 0.2 μm^2) determined from the AFM image. Applying an rf-field to the sample results in the observation of quantized voltage steps, known as Shapiro steps, in the I-V characteristics [19]. The voltage steps, of amplitude $h\omega/2e$ (ω is the microwave frequency), are a manifestation of the ac Josephson effect, and are evident in Fig. 8.2d. The induced superconductivity manifests itself also at finite bias in the form of subgap structure in the differential resistance due to multiple Andreev reflections [22], as shown in Fig. 8.2c. This subgap structure consists of a series of minima at source-drain voltages $V = 2\Delta/en$ ($n = 1, 2..$), which enables us to determine the superconducting gap. We find $\Delta = 125$ μeV

as expected for our Ti/Al bilayers[17]. For $V > 2\Delta/e$, the differential resistance returns to the normal state value.

8.5 Gate dependence of the supercurrent

Having established the existence of the Josephson effect in graphene, we analyse the gate voltage dependence of the critical current. Figure 8.2a shows several *I-V* traces taken at different V_G, where it can already be seen that varying the gate voltage has a strong effect on the maximum supercurrent flowing through the device. This behaviour can be more readily seen in Fig. 8.3a, where the differential resistance is plotted as a function of current bias and gate voltage. By changing V_G we can shift continuously the Fermi energy from the valence band ($V_G < V_D$) to the conduction band ($V_G > V_D$): irrespective of the sign of V_G, we find a finite supercurrent. This demonstrates that the devices operate as bipolar supercurrent transistors: the supercurrent is carried by hole Cooper pairs when the Fermi level is in the valence band and by electron Cooper pairs when it is in the conduction band. Note that in going from valence to conduction band, we sweep the position of the Fermi level through the Dirac point. Strikingly, even then the supercurrent remains finite, despite the fact that for perfect graphene theory predicts a vanishing density of states at $V_G = V_D$ [23]. This behaviour has been observed in all samples and demonstrates that electronic transport in graphene is phase coherent irrespective of the gate voltage, including when the Fermi energy is located at the Dirac point.

8.6 $I_c R_n$ product

In conventional Josephson junctions, the critical current correlates with the normal state conductance, G_n [24]. In graphene this correlation can be observed directly, as shown in Fig. 8.3a, because both I_c and G_n depend on V_G. To analyse this correlation, we plot the product of the measured critical current and the normal state resistance ($R_n = 1/G_n$), or $I_c R_n$ product (see Fig. 8.3b). For large doping (i.e. high $|V_G|$), we find that the $I_c R_n$ product is of the order of Δ/e, whereas around the Dirac point $I_c R_n$ is suppressed. This behaviour may in part originate from the difference between the measured critical current (i.e. the switching current) and the intrinsic critical current of our junctions [19, 20], which could be more pronounced at low V_G, where I_c itself is smaller. Note, however, that our observations agree qualitatively with recent theoretical predictions for ballistic graphene Josephson junctions, in the short junction limit,
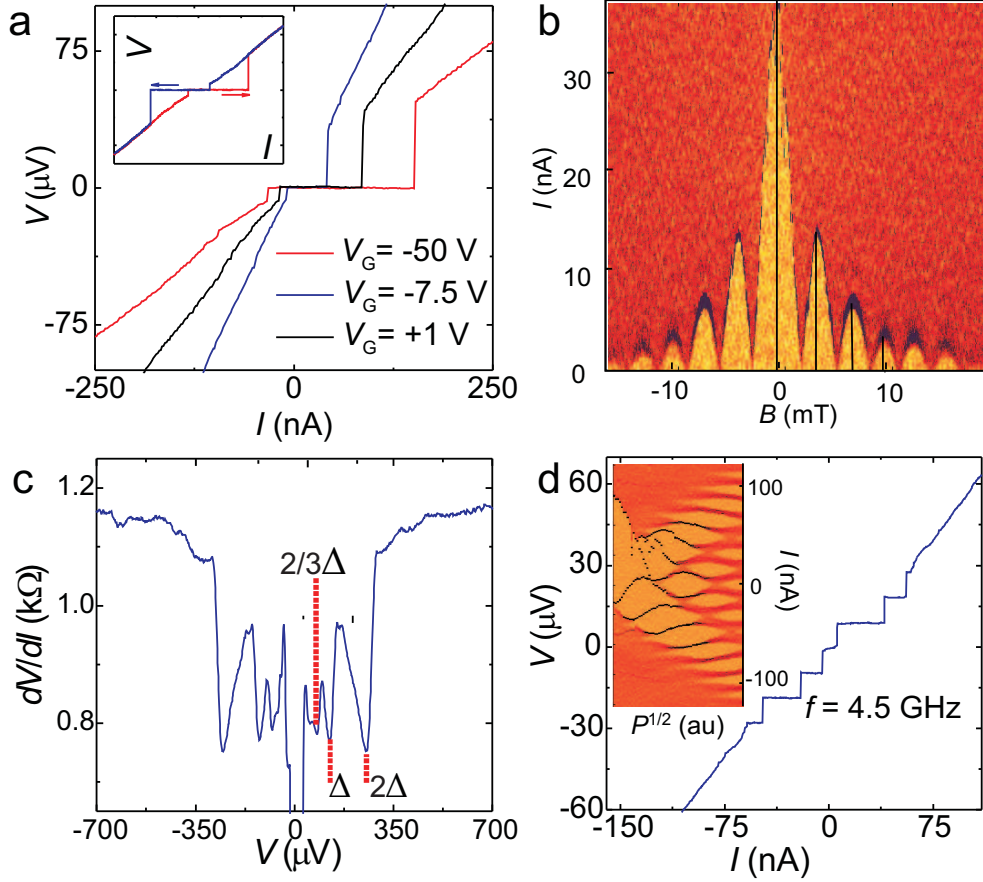
Figure 8.2: Josephson effect in graphene. **a**, Voltage, V, versus current bias, I, characteristics at various V_G, showing a modulation of the critical current. Inset: current bias sweeps from negative to positive (red) and viceversa (blue), showing that the asymmetry in the main panel is due to hysteretic behaviour (the retrapping current is usually smaller than the switching current, due to small damping). **b**, Color-scale representation of $dV/dI(I, B)$ at $T = 30$ mK (yellow-orange is zero, i.e. supercurrent region, and red corresponds to finite dV/dI). The critical current exhibits a series of oscillations described by a Fraunhofer-like pattern. **c**, Differential resistance, dV/dI, versus V, showing multiple Andreev reflection dips below the superconducting energy gap. The dips in dV/dI occur at values of $V = 2\Delta/en$, where n is an integer number. **d**, ac-Josephson effect. The Shapiro steps in the V-I characteristics appear when the sample is irradiated with microwaves. In the example, we applied 4.5 GHz microwaves, resulting in 9.3 μV voltage steps. Inset: Colour-scale plot showing the characteristic microwave amplitude $P^{1/2}$ dependence of the ac Josephson effect (orange/red corresponds to zero/finite dV/dI).

which is appropriate for our devices. This theory also predicts $I_c R_n \sim \Delta/e$ for high doping and a suppression of $I_c R_n$ near V_D, albeit the magnitude and the
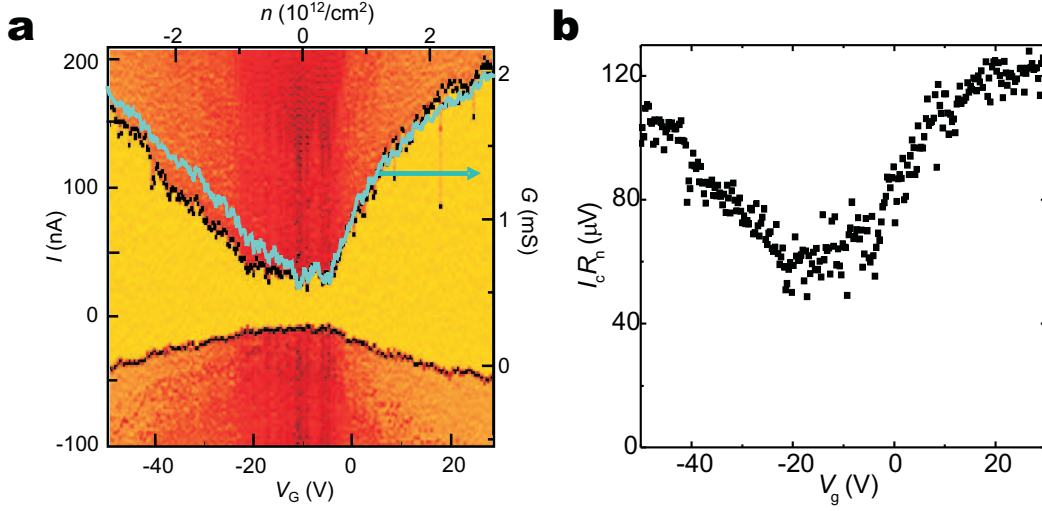
Figure 8.3: Bipolar supercurrent transistor behaviour and finite supercurrent at the Dirac point. **a**, Colour-scale plot of dV/dI (V_G,I). Yellow means zero, i.e., supercurrent region, and finite dV/dI increases via orange to dark red. The current is swept from negative to positive values (see also inset to Fig. 8.2**a**). The top axis shows the electron density, n, as obtained from geometrical considerations [1]. For large negative (positive) V_G the supercurrent is carried by hole (electron) Cooper pairs. The supercurrent at the Dirac point is finite. Note that the critical current is not symmetric with respect to V_D. The origin of this asymmetry is not known, but a similar asymmetry is seen in the normal state conductance (blue curve). **b**, Product of the critical current times the normal state resistance versus V_G. The normal state resistance is measured at zero source-drain bias, at $T = 30$ mK and with a small magnetic field to drive the electrodes in the normal state. The $I_c R_n$ product exhibits a dip around the Dirac point (see main text).

energy scale over which the suppression takes place are smaller (in particular, the range of Fermi energy over which the suppression occurs is roughly an order of magnitude larger in the experiment as compared to theory [14]). More detailed studies are necessary to shed light on the precise origin of the suppression of the $I_c R_n$ product.

8.7   Time reversal symmetry

Theory [14] also points to an interesting aspect of supercurrent in graphene, related to the role of time reversal symmetry, which originates from the unique electronic properties of this material. At low energy, the band structure of graphene consists of two identical, independent valleys centered on the so-called K and K'
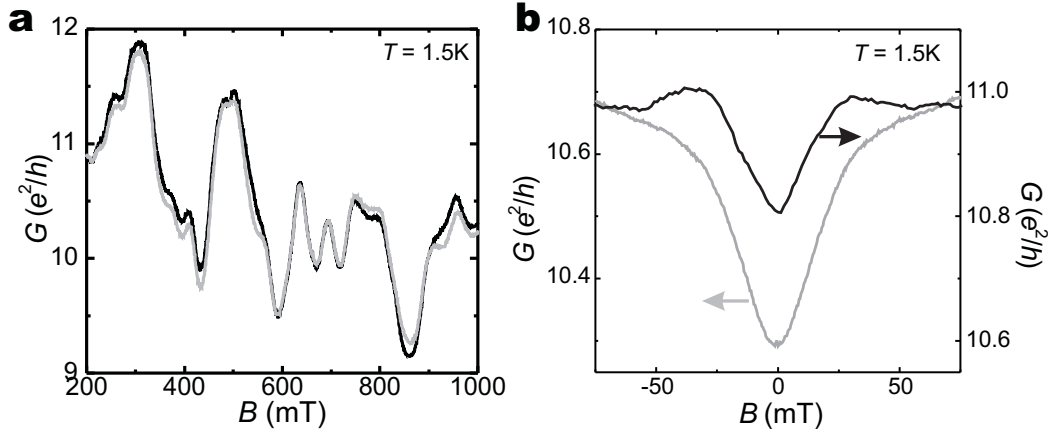
Figure 8.4: Magneto-conductance measurements. **a**, Conductance versus magnetic field at $T \sim$1.5 K for a single layer device at $V_G = V_D$. The red and black traces are two subsequent measurements, showing reproducible conductance fluctuations with a root mean square amplitude of e^2/h. **b**, Low field magnetoconductance measured at $T \sim$1.5 K (electrodes in the normal state) for two different single layer devices (the red trace corresponds to the device measured in **a**), showing that the amplitude of the weak localization effect is sample dependent and suppressed as compared to the expected value $\sim e^2/h$. Each curve results from an ensemble average of 66 individual magneto-resistance measurements taken at different gate voltages near the Dirac point.

points [23], that transform into each-other upon time reversal. Since Cooper pairs are made out of time reversed electron states, the two electrons in Cooper pairs that are injected from the superconducting electrodes into graphene go to opposite K-points (see Fig. 8.1b), and TRS is intrinsically preserved. The situation is very different for normal-state transport, where the dynamics of the electrons is determined by an effective "one-valley" Hamiltonian, which is responsible for example for the anomalous QHE [4, 5]. For this effective Hamiltonian, TRS is easily broken due to imperfections in the graphene sheet [16, 25], and can be restored only up to the extent that there exists a coupling mechanism between the two valleys (such as short-range scattering at impurities or at the graphene edges) [25, 26, 27]. This extrinsic dependence has a profound influence on other quantum interference phenomena in graphene that, like the Josephson super-current, rely on the presence of time reversal symmetry. We believe that this explains why supercurrent in graphene are very robust, whereas both in our own samples (see Fig. 8.4b) and other recent measurements [16, 28], weak-localization was found to exhibit a surprising sample dependent behaviour and was often suppressed. This interpretation is consistent with the observation of aperiodic conductance fluctuations [29] of amplitude e^2/h (see Fig. 8.4a), whose occurrence

requires phase coherence but not time reversal symmetry.

References

[1] Novoselov, K. S. *et al.* , *Electric field effect in atomically thin carbon films.* Science **306**, 666-669 (2004).

[2] Novoselov, K. S. et al. *Two-dimensional gas of massless Dirac fermions in graphene.* Nature **438**, 197-200 (2005).

[3] Zhang, Y. B., Tan, Y. W., Stormer, H. L. & Kim, P. *Experimental observation of the quantum Hall effect and Berry's phase in graphene.* Nature **438**, 201-204 (2005).

[4] Gusynin, V. P. & Sharapov, S. G. *Unconventional integer quantum Hall effect in graphene.* Phys. Rev. Lett. **95**, 256802 (2005).

[5] Peres, N. M. R., Guinea, F. & Castro Neto, A. H. *Electronic properties of disordered two-dimensional carbon.* Phys. Rev. B **73**, 125411 (2006).

[6] Fradkin, E. *Critical-Behavior of Disordered Degenerate Semiconductors.2. Spectrum and Transport-Properties in Mean-Field Theory.* Phys. Rev. B **33**, 3263-3268 (1986).

[7] Ludwig, A. W. W., Fisher, M. P. A., Shankar, R. & Grinstein, G. *Integer Quantum Hall Transition - an Alternative Approach and Exact Results.* Phys. Rev. B **50**, 7526-7552 (1994).

[8] Ziegler, K. *Delocalization of 2D dirac fermions: The role of a broken supersymmetry.* Phys. Rev. Lett. **80**, 3113-3116 (1998).

[9] Katsnelson, M. I. *Zitterbewegung, chirality, and minimal conductivity in graphene.* Eur. Phys. J. B. **51**, 157-160 (2006).

[10] K. Nomura, A. H. M. *Quantum Transport of Massless Dirac Fermions in Graphene.* cond-mat/0606589 (2006).

[11] I.L. Aleiner, K. B. E. Effect of Disorder on Transport in Graphene. cond-mat/0607200 (2006).

[12] Altland, *A. Low energy theory of disordered graphene.* cond-mat/0607247 (2006).

[13] Josephson, B. D. *Possible New Effects in Superconductive Tunnelling.* Phys. Lett. **1**, 251-253 (1962).

[14] M. Titov, C. W. J. B. *The Josephson effect in ballistic graphene.* Phys. Rev. B **74**, 041401(R) (2006).

[15] Degennes, P. G. *Boundary Effects in Superconductors.* Rev. Mod. Phys. **36**, 225-237 (1964).

[16] Morozov, S. V. et al. *Strong suppression of weak localization in graphene.* Phys. Rev. Lett. **97**, 016801 (2006).

[17] Jarillo-Herrero, P., van Dam, J. A. & Kouwenhoven, L. P. *Quantum supercurrent transistors in carbon nanotubes.* Nature **439**, 953-956 (2006).

[18] Datta, S. *Electronic Transport in Mesoscopic Systems* (Cambridge University Press, Cambridge, 1995).

[19] Tinkham, M. *Introduction to Superconductivity* (McGraw-Hill, Singapore, 1996).

[20] Joyez, P., Lafarge, P., Filipe, A., Esteve, D. & Devoret, *M. H. Observation of Parity-Induced Suppression of Josephson Tunneling in the Superconducting Single-Electron Transistor.* Phys. Rev. Lett. **72**, 2458-2461 (1994).

[21] A. Barone, G. P. *Physics and applications of the Josephson effect* (John Wiley & Sons, New York, 1982).

[22] Octavio, M., Tinkham, M., Blonder, G. E. & Klapwijk, T. M. *Subharmonic Energy-Gap Structure in Superconducting Constrictions.* Phys. Rev. B **27**, 6739-6746 (1983).

[23] Dresselhaus, M. S., Dresselhaus, G., Eklund, P. C. *Science of Fullerenes and Carbon Nanotubes* (Academic Press, San Diego, 1996).

[24] Likharev, K. K. *Superconducting Weak Links.* Reviews of Modern Physics **51**, 101-159 (1979).

[25] A.F. Morpurgo, F. G. *Intervalley scattering, long-range disorder, and effective time reversal symmetry breaking in graphene.* cond-mat/0603789 (2006).

[26] Suzuura, H. & Ando, T. *Crossover from symplectic to orthogonal class in a two-dimensional honeycomb lattice.* Phys. Rev. Lett. **89**, 266603 (2002).

[27] E. McCann, K. K., V.I. Fal'ko, H. Suzuura, T. Ando, B.L. Altshuler. *Weak localisation magnetoresistance and valley symmetry in graphene.* cond-mat/0604015 (2006).

[28] Berger, C. et al. *Electronic confinement and coherence in patterned epitaxial graphene.* Science **312**, 1191-1196 (2006).

[29] Lee, P. A. & Stone, A. D. Un*iversal Conductance Fluctuations in Metals.* Phys. Rev. Lett. **55**, 1622-1625 (1985).

Summary

Quantum transport in molecular devices and graphene

Miniaturization of electronic circuits has brought us to the stage where we can electrically contact even single molecules. Their potential as electronic building blocks for nanoscale electronics and the drive to understand their transport properties have stimulated both applied and basic research. One of the advantages of molecular devices is the synthetic tailorability - molecules can be designed to have built-in functionality. Electronic transport measurements offer a unique possibility to study the properties of single, semi-isolated molecules. The transport properties of graphene - a monoatomic layer of graphite - are also fascinating, but for a different reason. Electrons in this recently discovered system behave as massless Dirac particles. This is exceptional for a solid state system and opens the way for a number of exciting experiments.

This Thesis describes a series of experiments aiming at contacting single molecules and graphene in order to study their transport properties at low temperatures. Electron beam lithography (EBL) has insufficient resolution to fabricate electrodes with a spacing of approximately one nanometer, which is the typical size of a molecule. Several techniques have been developed to overcome this obstacle. These include, scanning probe microscopy, electromechanical break-junctions and shadow evaporation. Here, we use electromigration of thin gold wires as a fabrication method for nanogaps. Electromigration - current induced material transport - results in intentional failure of a wire. In Chapter 4 we demonstrate that in the final stage of the electromigration atoms can be removed one by one, resulting in sub-nanometer gaps.

Imaging the gap is difficult using conventional techniques, like scanning electron microscopy, because the resolution is too low to resolve the electrode geometry in detail. This motivated us to develop a technique to image the nanogap formation *in situ* using transmission electron microscopy (TEM), see Chapter 5. Thin (12 nm) gold wires are fabricated on top of a transparent silicon-nitride membrane 'window'. Using a home-built sample holder, we electromigrate the

wires while observing them with TEM. This allows us to monitor the nanogap formation process real-time. Due to gradients in the material flux, voids are created at the cathode side of the wire, whereas hillocks appear at the anode side. Once a constriction becomes so narrow that a single grain boundary spans the width of the constriction, the breaking continues along this grain boundary. A remarkable large deformation of the electrodes occurs in the very final stage ($\lesssim 50$ ms) of the breaking.

At sufficiently low temperatures, a single molecule weakly coupled to metallic electrodes via tunnel barriers behaves as a quantum dot. The number of electrons on the molecule can be adjusted by applying a voltage to a capacitively coupled gate electrode. Transport measurements as a function of this gate voltage reveal information about the energy spectrum of the molecule. In addition to electronic excitations, molecules are flexible and can hence also exhibit vibrational excitations. The molecule that we study experimentally in Chapter 6, a manganese-acetate derivative, belongs to the class of single molecule magnets (SMM). At low temperature, these molecules act as tiny magnets and show magnetic hysteresis, a property which results from their high-spin ground state and large anisotropy barrier. Since electrons not only possess charge but also spin, the spin state of the molecule changes when electrons are added and subtracted. This means that the molecule can be brought into magnetic excited states as a result of a charge current. In reverse, the magnetic excitations affect the differential conductance of the molecule.

Ultra-small gold grains, trapped in the gap after electromigration, are a nuisance for molecular transport experiments as they mimic the current-voltage characteristics expected for single molecules. At the same time, gold grain quantum dots are an interesting system by themselves. Similar to molecules, gold grains can act as artificial magnetic impurities. The net spin of magnetic impurities is screened by the conduction electrons in the leads - the Kondo effect - resulting in an enhancement of the conductance of the gold grain around zero bias voltage. In Chapter 7 we study the interaction between an artificial magnetic impurity (gold grain) and intentionally deposited cobalt atoms in the leads. The indirect, or RKKY, spin-spin interaction results in the suppression of the Kondo-effect on the energy-scale of the interaction strength. In this experiment we study the competition between the Kondo effect and RKKY interaction at the level of a single spin.

In Chapter 8 we discuss the observation of induced supercurrents - currents that flow without dissipation - in graphene. Graphene devices are prepared by mechanical exfoliation of natural graphite followed by deposition on a silicon substrate. Optical microscopy is used to preselect few-layer flakes that are sub-

sequently contacted by closely spaced metallic leads using standard EBL techniques. Below ∼1 K the leads, made from the superconducting metals titanium/aluminium, become superconducting. As a result of the proximity effect, superconducting properties are also induced in the graphene sheet. The supercurrent is bipolar: a gate electrode can tune the Fermi energy from the conduction band - where Cooper pairs consist of electrons - to the valence band - where holes form the Cooper pairs. Notably, the critical current does not vanish at the charge degeneracy or Dirac point, clearly demonstrating phase coherence in this regime.

<div align="right">
Hubert Heersche

December, 2006
</div>

Samenvatting

Quantum transport in moleculaire systemen en grafeen

Miniaturisatie van elektronische circuits heeft er toe geleid dat we zelfs aan enkele moleculen elektrische contacten kunnen maken. Het potentieel van moleculen als bouwstenen voor elektronica op nanoschaal en de drijfveer hun transport eigenschappen beter te begrijpen, hebben zowel toegepast als fundamenteel onderzoek gestimuleerd. Een van de voordelen van moleculaire systemen is de synthetische vrijheid: moleculen kunnen zo ontworpen worden dat ze een ingebouwde functionaliteit hebben. Het meten van elektrisch transport biedt een unieke mogelijkheid om de eigenschappen van individuele, semi-geïsoleerde, moleculen te bestuderen. Ook grafeen - een mono-atomaire laag grafiet - heeft fascinerende transport eigenschappen, maar om een heel andere reden. In dit recent ontdekte systeem gedragen elektronen zich als massaloze Dirac deeltjes. Dit is uitzonderlijk voor een vaste stof systeem en maakt het mogelijk tal van interessante experimenten te doen.

In dit proefschrift worden een aantal experimenten beschreven waarin we door middel van het maken van elektrisch contact met moleculen en grafeen hun transporteigenschappen bij lage temperaturen bestuderen. Elektronen-bundel lithografie (EBL) heeft onvoldoende resolutie om de elektrodes met een tussenafstand van ongeveer een nanometer - de typische afmeting van een molecuul - te fabriceren. De afgelopen jaren zijn er verscheidene technieken ontwikkeld om dit obstakel te overwinnen. Wij gebruiken elektromigratie van dunne gouddraden als fabricage methode voor nanoelektrodes. Elektromigratie - materiaal transport geïnduceerd door een elektrische stroom - resulteert in het intentioneel breken van de draad. In Hoofdstuk 4 laten we zien dat in het laatste stadium van het elektromigratie proces, de atomen een voor een verwijderd kunnen worden. Het resultaat is een afstand van minder dan een nanometer tussen de elektrodes.

Het afbeelden van de nanoelektrodes is moeilijk wanneer gebruik wordt gemaakt van conventionele methodes, zoals elektronen microscopie. Dit komt doordat de resolutie te laag is om de geometrie van de elektrodes duidelijk te kunnen

onderscheiden. Daarom hebben we een techniek ontwikkeld om het breekproces *in situ* af te beelden met behulp van transmissie elektronen microscopie (TEM), zie Hoofdstuk 5. Dunne (12 nm) gouddraadjes zijn daartoe gefabriceerd op een transparant 'raampje' bestaande uit een silicium-nitride-membraan. De draden worden gebroken middels elektromigratie terwijl ze met TEM worden geobserveerd. We maken daarbij gebruik van een zelf ontwikkelde substraat houder. Hierdoor kunnen we het vormingsproces van de nano-elektrodes *real-time* volgen. Door gradiënten in de materiaal flux, vormen zich eerst insnoeringen aan de kathode kant van het draadje, terwijl kleine materiaal ophopingen ontstaan aan de anode kant. Zodra een constrictie zo nauw wordt, dat een enkele korrelgrens over de gehele breedte van de constrictie loopt, verloopt het breekproces verder langs deze korrelgrens. Een opmerkelijke grote deformatie van de elektrodes vindt plaats gedurende het laatste gedeelte ($\lesssim$ 50 ms) van het breken.

Bij voldoende lage temperaturen gedraagt een enkel molecuul, dat zwak gekoppeld is aan metalen elektrodes, zich als een *quantum dot*. Het aantal elektronen op het molecuul kan worden aangepast door een spanning aan te leggen op een capacitief gekoppelde *gate*-elektrode. Transport metingen als een functie van deze *gate*-spanning onthullen informatie over het energie-spectrum van het molecuul. Naast elektronische excitaties kunnen moleculen vanwege hun beweeglijke vrijheid ook vibratie-excitaties vertonen. Het molecuul dat we experimenteel bestuderen in Hoofdstuk 6, een afgeleide van mangaan-acetaat, behoort tot de klasse van de moleculaire magneten. Bij lage temperatuur gedragen deze moleculen zich als kleine magneetjes en vertonen ze magnetische hysterese, een eigenschap die het gevolg is van hun hoge spin grondtoestand en grote anisotropiebarrière. Omdat elektronen niet alleen lading maar ook spin bezitten, verandert de spintoestand van het molecuul wanneer elektronen worden toegevoegd en worden weggehaald. Dit betekent dat het molecuul in magnetische geëxiteerde toestanden kan worden gebracht vanwege een ladingsstroom. Omgekeerd beïnvloeden de magnetische excitaties ook de differentiële geleiding van het molecuul.

Ultra-kleine goudkorrels, die zich tussen de elektrodes bevinden na elektromigratie, zijn vervelend voor moleculaire transport experimenten. Dit komt doordat deze goudkorrels soortgelijke stroom-spannings karakteristieken laten zien als enkele moleculen. Tegelijkertijd vormt een uit een goudkorrel bestaande *quantum dot* ook een interessant experimenteel systeem. Net als moleculen, kunnen goudkorrels zich gedragen als kunstmatige magnetische verontreinigingen. De spin van een magnetische verontreiniging wordt afgeschermd door de geleidingselektronen in de contacten - het Kondo-effect. Dit resulteert in een verhoging van de geleiding van de goudkorrel voor lage spanningen. In Hoofdstuk 7 bestuderen we de interactie tussen een artificiële magnetische verontreiniging (goudkorrel)

en intentioneel gedeponeerde kobalt atomen in de contacten. De indirecte (ofwel RKKY) spin-spin interactie zorgt voor een onderdrukking van het Kondo-effect op de energieschaal van de interactiesterkte. In dit experiment bestuderen we de competitie tussen het Kondo-effect en RKKY interactie op het niveau van een enkele spin.

In Hoofdstuk 8 bespreken we de observatie van een geïnduceerde superstroom - stroom zonder dissipatie - in grafeen. De grafeen devices zijn gemaakt door mechanische exfoliatie van natuurlijk grafiet gevolgd door depositie op een silicium substraat. Optische microscopie is gebruikt om stukjes grafiet van slechts een paar lagen dik voor te selecteren. Vervolgens wordt middels twee dicht bij elkaar gelegen elektrodes elektrisch contact gemaakt. We maken hierbij gebruik van standaard EBL technieken. Beneden een temperatuur van ongeveer 1 K worden de contacten supergeleidend, omdat ze zijn gemaakt de supergeleidende metalen titaan/aluminium. Als gevolg van het proximity effect worden de supergeleidende eigenschappen ook geïnduceerd in het grafeen. De superstroom is bipolair: een *gate*-elektrode kan de Fermi-energie verschuiven van de conductieband - waar Cooper paren bestaan uit elektronen - naar de valentieband - waar gaten de Cooper paren vormen. Het is opmerkelijk dat de superstromen niet verdwijnen op het zogenaamde Dirac of ladingsontaardingspunt, hetgeen een duidelijke aanwijzing is dat dit regiem fasecoherent is.

Hubert Heersche
December, 2006

Curriculum Vitae

Hubertus Bernardus Heersche

22-09-1977   Born in Almelo, The Netherlands.

1990-1996   Secondary school, Twickel College, Hengelo.

1996-2002   M.Sc. Applied Physics (*cum laude*), University of Groningen.
Graduate research in the group of prof. dr. ir. B. J. van Wees.

2000   Master courses at Victoria University of Wellington, New Zealand

2002   Internship at NTT Basic Research Laboratories,
Atsugi, Kanagawa, Japan.

2002-2006   Ph.D. research at Delft University of Technology
under supervision of prof. dr. ir. L. P. Kouwenhoven &
prof. dr. ir. H. S. J. van der Zant.
Subject: Quantum transport in molecular devices and graphene.

List of publications

1. *Bipolar supercurrents in graphene*
   Hubert B. Heersche, Pablo Jarillo-Herrero, Jeroen Oostinga, Lieven M. K. Vandersypen, and Alberto F. Morpurgo.
   Submitted to Nature.

2. *In situ imaging of electromigration-induced nanogap formation by transmission electron microscopy*
   Hubert B. Heersche, Günther Lientschnig, Kevin O'Neill, Herre S. J. van der Zant, Henny W. Zandbergen
   Submitted to Nanoletters.

3. *Kondo effect in the presence of magnetic impurities.*
   H. B. Heersche, Z. de Groot, J. A. Folk, L. P. Kouwenhoven, H. S. J. van der Zant, A. A. Houck, J. Labaziewicz, and I. L. Chuang
   Physical Review Letters **96**, 017205 (2006)

4. *Electron transport through single Mn-12 molecular magnets*
   H. B. Heersche, Z. de Groot, J. A. Folk, H. S. J. van der Zant, C. Romeike, M. R. Wegewijs, L. Zobbi, D. Barreca, E. Tondello, and A. Cornia
   Physical Review Letters **96**, 206801 (2006)

5. *Molecular three-terminal devices: fabrication and measurements.*
   H. S. J. van der Zant, Y. V. Kervennic, M. Poot, K. O'Neill, Z. de Groot, J. M. Thijssen, H. B. Heersche & N. Stuhr-Hansen, T. Bjornholm, D. Vanmaekelbergh, C. A. van Walree, and L. W.Jenneskens
   Faraday Discussions **131**, 347 (2006).

6. *Electrical detection of spin accumulation and spin precession at room temperature in metallic spin valves.*
   F. J. Jedema, M. V. Costache, H. B. Heersche, J. J. A. Baselmans, B. J. van Wees
   Applied Physics Letters **81**, 5162 (2002).

7. *Model for ballistic spin-transport in ferromagnet / two-dimensional electron gas / ferromagnet structures.*
   Th. Schäpers, J. Nitta, H. B. Heersche, H. Takayanagi
   Physica E **13**, 564 (2002).

8. *Investigation of ferromagnetic microstructures by local Hall effect and magnetic force microscopy.*
   J. Nitta, Th. Schäpers, H. B. Heersche, T. Koga, Y. Sato, H. Takayanagi
   Japanese Journal of Applied Physics, **41**, 2497 (2002).

9. *Electrical detection of spin precession in a metallic mesoscopic spin valve.*
   F. J. Jedema, H. B. Heersche, A. T. Filip, J. J. A. Baselmans, B. J. van Wees
   Nature **416**, 713 (2002).

10. *Enhancement of spin injection from ferromagnetic metal into a two-dimensional electron gas using a tunnel barrier.*
    H. B. Heersche, Th. Schäpers, J. Nitta, H. Takayanagi
    Physical Review B **64**, 161307 (2001).

11. *Interference ferromagnet/semiconductor/ferromagnet spin field-effect transistor.*
    Th. Schäpers, J. Nitta, H. B. Heersche, and H. Takayanagi
    Physical Review B **64**, 125314 (2001)